Is a catalyst always beneficial in plasma catalysis? Insights from the many physical and chemical interactions

Is a catalyst always beneficial in plasma catalysis? Insights from the many physical and chemical interactions

Björn Loenders *, Roel Michiels [a] and Annemie Bogaerts [b]

Research group PLASMANT, Department of Chemistry, University of Antwerp, Universiteitsplein 1, B-2610 Wilrijk-Antwerp, Belgium

* Corresponding author, E-mail address: bjorn.loenders@uantwerpen.be

a) E-mail address: roel.michiels@uantwerpen.be

b) E-mail address: annemie.bogaerts@uantwerpen.be

Abstract

Plasma-catalytic dry reforming of CH_4 (DRM) is promising to convert the greenhouse gasses CH_4 and CO_2 into value-added chemicals, thus simultaneously providing an alternative to fossil resources as feedstock for the chemical industry. However, while many experiments have been dedicated to plasma-catalytic DRM, there is no consensus yet in literature on the optimal choice of catalyst for targeted products, because the underlying mechanisms are far from understood. Indeed, plasma catalysis is very complex, as it encompasses various chemical and physical interactions between plasma and catalyst, that depend on many parameters. This complexity hampers the comparison of experimental results from different studies, which, in our opinion, is an important bottleneck in the further development of this promising research field. Hence, in this perspective paper, we describe the important physical and chemical effects that should be accounted for when designing plasma-catalytic experiments in general, highlighting the need for standardized experimental setups, as well as careful documentation of packing properties and reaction conditions, to further advance this research field. On the other hand, the many parameters also create many windows of opportunity for further optimizing plasma-catalytic systems. Finally, various experiments also reveal the lack of improvement in plasma catalysis compared to plasma-only, specifically for DRM, but the underlying mechanisms are unclear. Therefore, we present our newly developed coupled plasma-surface kinetics model for DRM, to provide more insight in the underlying reasons. Our model illustrates that transition metal catalysts can adversely affect plasma-catalytic DRM, if radicals dominate the plasma-catalyst interactions. Thus, we demonstrate that a good understanding of the plasma-catalyst interactions is crucial to avoid conditions at which these interactions negatively affect the results, and we provide some recommendations for improvement. For instance, we believe that plasma-catalytic DRM may benefit more from higher reaction temperatures, at which vibrational excitation can enhance the surface reactions.

Keywords: Plasma catalysis, Dry reforming of methane, Discharges, Reaction kinetics, Modelling

1 Introduction

Climate change and global warming pose an increasing threat to both human welfare and the environment. Moreover, global warming is likely to exceed 1.5 °C relative to pre-industrial levels in the coming decades, which will result in additional severe risks for many human and natural systems, and is expected to cause irreversible changes. Therefore, it is of great importance to strongly lower our greenhouse gas emissions [1]. Yet, the atmospheric concentrations of greenhouse gases are still rising, with CO_2 and CH_4 reaching globally-averaged concentrations of 416 ppm and 1910 ppb, respectively, in November 2021 [2,3]. This corresponds to a rise of 49% and 173% relative to pre-industrial levels (i.e., 280 ppm and 700 ppb), for CO_2 and CH_4, respectively [4]. On the other hand, human society is still strongly dependent on the finite reserves of fossil resources, which are becoming increasingly depleted, while combustion of these resources results in the emission of large amounts of CO_2 into the atmosphere. An intuitive solution to both problems would be to recycle CO_2 into new fuels and value-added chemicals, and thus close the carbon cycle [5]. Dry reforming of CH_4 (DRM) is a promising process in this regard as it converts the two most-abundant greenhouse gases, i.e. CO_2 and CH_4, into value-added products. This conversion can be achieved using conventional thermal catalysis. However, due to the extremely endothermic nature of this reaction, high temperatures (900-1273 K) are required to shift the thermal equilibrium towards syngas (CO/H_2) and attain a desirable conversion [6,7].

The conversion of CO_2 and CH_4 can however also be achieved at low bulk gas temperatures using plasma technology [8]. Plasma is (partially) ionized gas, containing a variety of both charged and neutral reactive species, such as electrons, ions, radicals and excited molecules. By applying an electric field to a gas, electrons and ions will be created, and mainly the light electrons will be accelerated by the electric field. Hence, it is possible to create plasmas in which the electron temperature is much higher (10^4-10^5 K) than the bulk gas temperature, which can be maintained at 300-1000 K. Such plasmas, characterized by a state of strong non-equilibrium, are referred to as non-thermal plasmas (NTP) [8,9]. However, the cocktail of reactive species formed upon collision of the electrons with the gas molecules results in a wide range of products, and as such, NTP is typically not selective in terms of product formation. Plasma catalysis therefore combines plasma with a catalyst to improve the selectivity towards desired end-compounds [9]. Particularly interesting products that can be formed from CO_2 and CH_4 using plasma (catalysis) are oxygenates, such as CH_3OH [10]. Indeed, CH_3OH is a valuable molecule, both for its use as a fuel, as well as building block for the chemical industry, and hence has been proposed as a key compound for an anthropogenic carbon cycle [5,8]. While CH_3OH synthesis from CO_2 and CH_4 in thermal catalysis would first require an energy-intensive conversion of these reactants to syngas (CO and H_2), followed by CH_3OH synthesis at high pressure, DRM via plasma catalysis can in principle produce CH_3OH at atmospheric pressure and (close to) ambient temperature [10].

However, in practice, it is not yet straightforward to selectively produce the desired end-compounds by plasma catalysis, and more research is crucial to make progress in this promising field of research. The reason is that plasma catalysis is very complex. Hence, in this perspective paper, we will first (in section 2) give some literature examples of DRM studies for a wide variety of catalysts, to illustrate that different authors report different results, which makes it difficult to gain deeper insight. This is indeed attributed to the high complexity of plasma catalysis. Therefore, in sections 3 and 4, we will zoom in on important physical and chemical effects, respectively, that are responsible for the complexity of plasma-catalytic reactions in general and should thus be accounted for when designing plasma-catalytic experiments. This way, we aim to stress the need for standardized experimental setups, as well as elaborate documentation of packing properties and reaction conditions to facilitate comparison of experimental results with each other and with modelling studies. To complement our discussion of these physical and chemical interactions that affect plasma-catalytic reactions in general, we present our own modelling results in section 5 to illustrate how some of the chemical aspects can affect plasma-catalytic DRM. We will provide insights from our model on why (and how) the combination of (transition metal) catalysts with plasma can also negatively affect the performance. Indeed, it is shown in literature (especially for DRM; see references in section 2) that plasma catalysis does not always yield improved performance compared to plasma without catalyst. Finally, in the Conclusions we will provide recommendations on how to overcome this problem.

2 The complexity of plasma catalysis

The aim of plasma catalysis is to combine the high reactivity of plasma with the selectivity of catalysts, and thus to combine the best of both worlds. In the ideal case, synergy is achieved between plasma and catalyst, meaning that the effect of plasma catalysis surpasses the sum of the effects of the plasma and catalyst alone. However, synergy does not always occur, and in some cases plasma catalytic DRM even performs worse than a plasma reactor that is empty or only filled with support packing (e.g., [11–15]). Thus, appropriate combinations of reaction parameters and catalyst materials need to be identified. Plasma-catalytic DRM has therefore been investigated experimentally with a wide variety of transition metal catalysts, including catalysts based on Ru [11], Re [12], Ir [12], Pd [12,14], Pt [12,13,15–17], Ag [12–14,17], Au [15], Cu [13,15,18,19], Fe [20], Co [19–21], Mn [19,22], and Ni [17,19,21–27].

For instance, Wang et al. [12] compared a wide range of transition metals (Ag, Pt, Pd, Re and Ir) on zeolite supports and reported the highest liquid yield (59-61%) and lowest coke deposition (5.1-9.3%) for Pt-based catalysts. On the other hand, their results also indicated that the combination of plasma and catalyst did not always yield better results than plasma alone. Indeed, all investigated catalysts gave a lower CH_4 conversion compared to the plasma with only the support packing, and only Re (and Pt, depending on the support) could attain a higher CO_2 conversion. Similar conclusions were drawn by Andersen et al. [13], who compared γ-Al_2O_3-supported Cu, Ag and Pt catalysts and observed a drop in CO_2 conversion when Cu was added to the γ-Al_2O_3 support. However, they reported improved alcohol selectivity for Cu/γ-Al_2O_3. Sentek *et al*. [14], studied the effect of Ag/γ-Al_2O_3 and Pd/γ-Al_2O_3 catalysts, and found that Pd/γ-Al_2O_3 improved C_2 hydrocarbon formation, while reducing the production of C_3 and C_4 hydrocarbons. When comparing to the plasma with only the support packing, the authors again observed that the presence of the catalysts reduced the CH_4 and CO_2 conversions, for a 1:1 CH_4/CO_2 feed mixture. Wang et al. [15] reported high selectivities of liquid oxygenates (50-60% combined liquid selectivity, assuming 10% C-deposition) by cooling the reactor with a ground water electrode. Additionally, the authors studied the use of γ-Al_2O_3 supported Cu, Au or Pt catalysts. While Cu/γ-Al_2O_3 improved the CH_3COOH selectivity, Au and Pt on γ-Al_2O_3 were the only catalysts that produced CH_2O. Nevertheless, the CO_2 conversion was significantly lower for Cu/γ-Al_2O_3 compared to only the γ-Al_2O_3 packing.

The effect of Pt nanoparticles deposited on a metal-organic framework support was examined by Vakili *et al.* [16], who found that the Pt did improve the CH_4 and CO_2 conversion, as well as the production of H_2, while lowering the selectivity to light hydrocarbons. Using *in situ* diffuse reflectance infrared Fourier transform spectroscopy (DRIFTS) the authors observed indications of HCOO* (formate) decomposition to CO, and C_2H_4 dehydrogenation on the catalyst. Mei *et al*. [17] reported that for γ-Al_2O_3 supported Ni, Pt and Ag catalysts, the CO_2 conversion is correlated to the basicity of the catalyst material, while the CH_4 conversion is affected by both catalyst properties and discharge characteristics. These authors also

reported that Ni/γ-Al_2O_3 gives the highest selectivity to liquid oxygenates (14%), while Pt/γ-Al_2O_3 is the only catalyst that forms CH_2O. Wang et al. [18] discovered a correlation between the Cu valence state and the oxygenate distribution for a range of Cu-based catalysts with different supports, with Cu^{2+} favoring alcohols and Cu^{+} enhancing acid selectivity.

Zeng *et al.* [19] studied plasma-catalytic DRM with Ni, Co, Cu and Mn catalysts supported on γ-Al_2O_3. From these four catalysts, the Ni/γ-Al_2O_3 and Mn/γ-Al_2O_3 showed plasma-catalytic synergy towards CH_4 conversion, but not for CO_2 conversion. Li et al. [20] compared Fe and Co catalysts on a SiO_2 aerogel support and found that Co/SiO_2 improved the selectivities of acids, as well as long-chain oxygenates, while Fe/SiO_2 favored the formation of alcohols. Similarly, Dou et al. [21] investigated the formation of acids vs. alcohols, but for Co- and Ni-based catalysts with different promotors, deposited on Ni-foams. These authors also found that metallic Co enhanced CH_3COOH formation, while oxygen vacancies improve alcohol formation.

Diao *et al*. [23] studied the effect of adding β-Mo_2C as a promotor to a Ni/γ-Al_2O_3 catalyst, which enhanced Ni dispersion, catalysts stability, as well as the conversions of CH_4 and CO_2. Khoja *et al.* [24] performed a process optimization of plasma-catalytic DRM with a Ni/La_2O_3-$MgAl_2O_4$ catalyst using statistical analysis methods. The authors attained conversions of 83% and 82% for CH_4 and CO_2, respectively. The excellent performance of this catalyst was attributed to its high Ni dispersion, strong oxidative capability and high basicity. Li *et al*. [25] studied the activity of different Ni-foam (NF) supported Ni-based catalysts for oxygenate production. Their results showed that Ni/NF and NiGa/NF formed CH_3COOH as the main oxygenate product, while NiAl layered double hydroxy (LDH) on NF favored CH_3OH. NiO/NF gave similar selectivities for CH_3OH and CH_3COOH.

Ray *et al.* [22] compared γ-Al_2O_3-supported Ni and Ni-Mn catalysts and found that Ni-Mn/γ-Al_2O_3 gave less coke deposition and a higher CH_4 conversion, while Ni/γ-Al_2O_3 performed better in terms of CO_2 conversion. In another work by the same authors [26] the effect of MgO and CeO_2 promotors on the performance of a Ni/γ-Al_2O_3 catalyst was investigated. The authors reported that the MgO-promoted catalyst showed the best performance. This could be attributed to a higher dispersion of Ni, as well as the higher basicity of the support material, which was suggested to enhance CO_2 conversion. The authors also observed that the MgO and CeO_2 promotors resulted in higher and lower H_2/CO ratios, respectively, compared to the empty DBD. Similarly, Zeng *et al*. [27] studied the use of K-, Ce- and Mg-promoted Ni/γ-Al_2O_3 catalysts and also found that the Mg promotor enhanced the H_2/CO ratio. The highest conversions, however, were achieved with the Ce- and K-promoted catalysts.

From the above, it is clear that although much experimental work has already been dedicated to plasma-catalytic DRM, detailed insight in the underlying mechanisms is still lacking. Indeed, as mentioned earlier, plasma-catalytic systems in general are highly complex and still not well understood. Therefore,

more fundamental research is required to rationally identify catalysts and reaction conditions that will provide high yield and energy efficiency towards a particular product [9,28]. The complexity of plasma catalysis is attributed to the plethora of interactions that can occur between the catalyst and the plasma. These effects, which are either chemical or physical in nature, can be divided in effects of the plasma on the catalyst or effects of the catalyst on the plasma. Plasma can affect the properties of the catalyst by, e.g., changing the morphology of the catalyst, reducing or oxidizing the catalyst material, and by altering its work-function [29,30]. In addition, plasma-produced reactive species like radicals, ions and vibrationally or electronically excited molecules might diffuse to the catalyst surface and partake in the surface chemistry. On the other hand, the catalyst can also alter the plasma, for example, in packed-bed dielectric barrier discharge (DBD) reactors, where introducing a catalyst or packing material into the discharge gap can lead to localized electric field enhancement and alter the discharge behavior of the plasma [29,30].

Since multiple of these interactions can occur simultaneously, it is often difficult to determine which effects contribute to the overall process, let alone correlate these to specific properties of the catalyst material or the plasma. Indeed, the presence of a catalyst or packing in the plasma does not only affect the system chemically, but also leads to physical effects, i.e., changes to the discharge behavior of the plasma. In sections 3 and 4 we will therefore discuss important physical and chemical interactions, to illustrate the difficulties associated with comparing experimental results among each other or with modelling studies. This makes it difficult to obtain more detailed insights, which is, in our opinion, one of the main bottlenecks for further development of the plasma-catalytic field and optimization of plasma-catalytic systems for gas conversion, such as DRM. A schematic overview of these simultaneous physical and chemical interactions is presented in Figure 1.

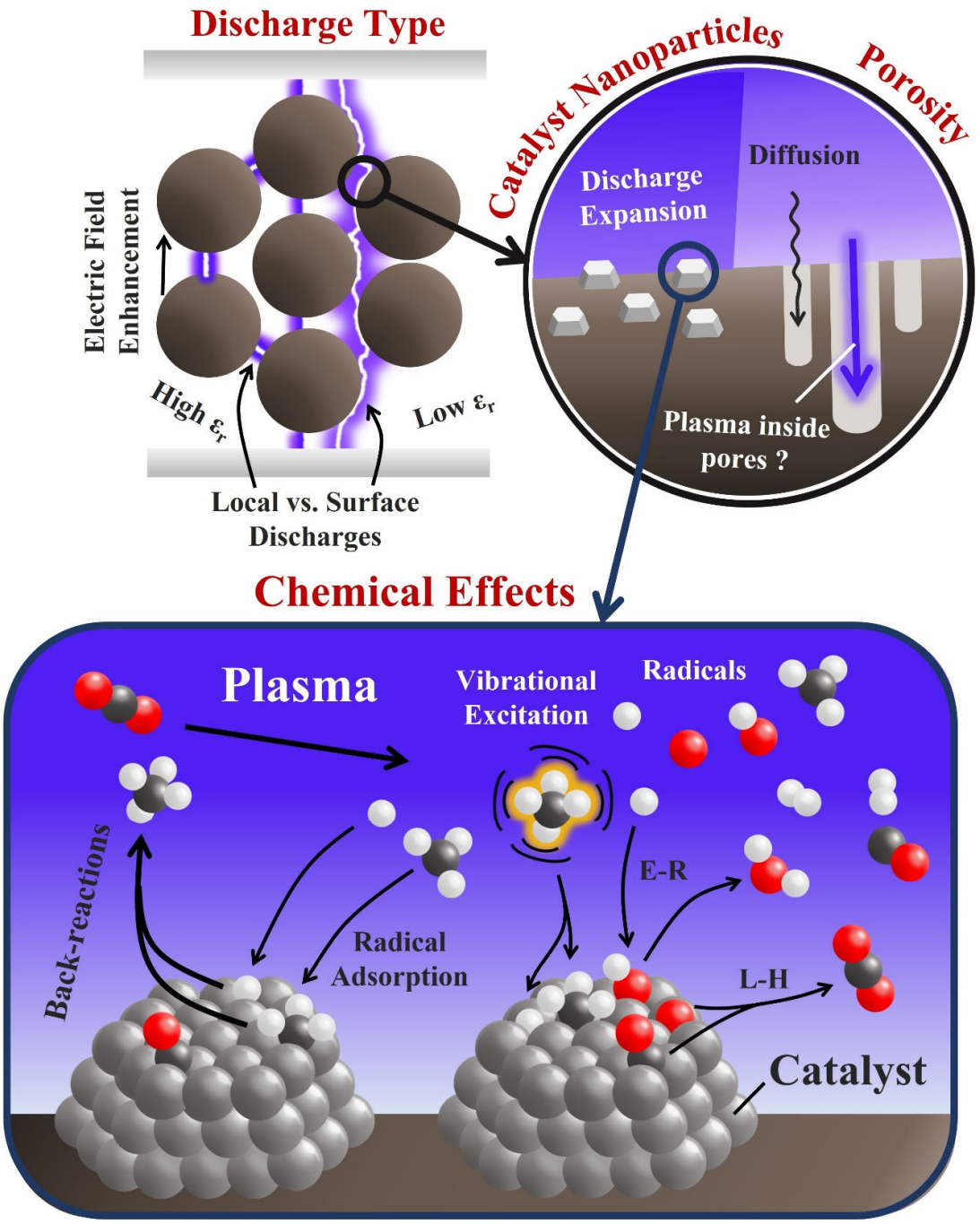

Figure 1. Schematic overview of the various physical and chemical plasma-catalytic interactions that will be discussed in this perspective paper. E-R and L-H are abbreviations for Eley-Rideal and Langmuir-Hinshelwood reactions, respectively.

Moreover, in section 5, we will provide insights from our own, newly developed model, to illustrate the role of certain chemical aspects discussed in section 4. We show that transition metal catalysts can also negatively affect plasma-catalytic DRM, by lowering the conversion of CH_4 and CO_2, if radicals

dominate the plasma-catalyst interactions. Effectively, while the goal of plasma catalysis is to improve conversion and selectivity relative to the plasma and catalyst alone, synergy is not guaranteed, and in several cases, combining the plasma with a catalyst negatively impacts the performance in DRM (e.g., [11–15]). Our modelling results provide more insight in the underlying reasons and indicate the need for a more coordinated approach towards catalyst selection. Finally, in the Conclusions, we provide some recommendations on how to overcome this issue, based on our own insights gained from the literature reports and our own model.

3 Physical effects

While strictly being not a catalytic effect, physical interactions between plasma and catalyst (or catalytic packing) can induce changes in the discharge behavior of the plasma and, in turn, substantially alter the plasma chemistry. The simultaneous occurrence of these interactions with any chemical effects that might happen on a catalyst surface can therefore significantly complicate the interpretation of experimental observations. Needless to say, a detailed insight in the impact of the support and catalyst particles on the plasma physics is required, yet currently this is still lacking [9].

3.1 Surface discharges vs. localized discharges: Using the packing to tune the contact between plasma and catalyst

The introduction of a support material (with, but also without catalyst particles) in the discharge gap can alter the plasma physics. Note that in plasma catalysis, the catalyst is typically loaded on packing beads (of a few mm diameter) inserted in a dielectric barrier discharge (DBD) plasma reactor. Both experimental [31] and modelling [32] studies for air plasmas have shown that the dielectric constant (ε_r) of the packing is an important material property in this regard, as it determines the type of discharges that can occur in between the packing beads. Low dielectric constants give rise to surface discharges on the packing beads, while higher dielectric constants promote the formation of ~~partial~~ discharges localized at the contact points between the beads. These ~~partial~~ local discharges can serve as staging points that facilitate streamer propagation to adjacent beads. However, for materials with very high dielectric constants, such as $BaTiO_3$ ($\varepsilon_r \approx 2600$), streamer propagation does not happen and only ~~partial~~ local discharges occur [31,32].

The effect of the dielectric constant on the discharge type is displayed in Figure 2, which shows images of microdischarges in a packed-bed DBD reactor in air, captured using an intensified charged coupled digital (ICCD) camera, as well as electron number densities from computer simulations. The images on the left show the position of the packing beads, while those in the middle show the ICCD images of microdischarges, and those on the right show the simulated electron number densities. The dielectric constant of the packing material drops from Figure 2 a) to c), with a) showing $BaTiO_3$ ($\varepsilon_r = 2600$), b) ZrO_2 ($\varepsilon_r = 25$) and c) glass beads ($\varepsilon_r = 5$). As can be seen in Figure 2 a) for $BaTiO_3$, which has a high dielectric constant of 2600, only localized microdischarges occur. For materials with intermediate dielectric constants, such as ZrO_2 ($\varepsilon_r = 25$) shown in Figure 2 b), surface discharges start occurring, while microdischarges localized at the contact points between the beads are still present as well. Packing materials with low dielectric constants predominantly form surface discharges, which connect to the surface of adjacent beads and thus spread out over the discharge gap, as can be seen for glass beads in Figure 2 c) [32].

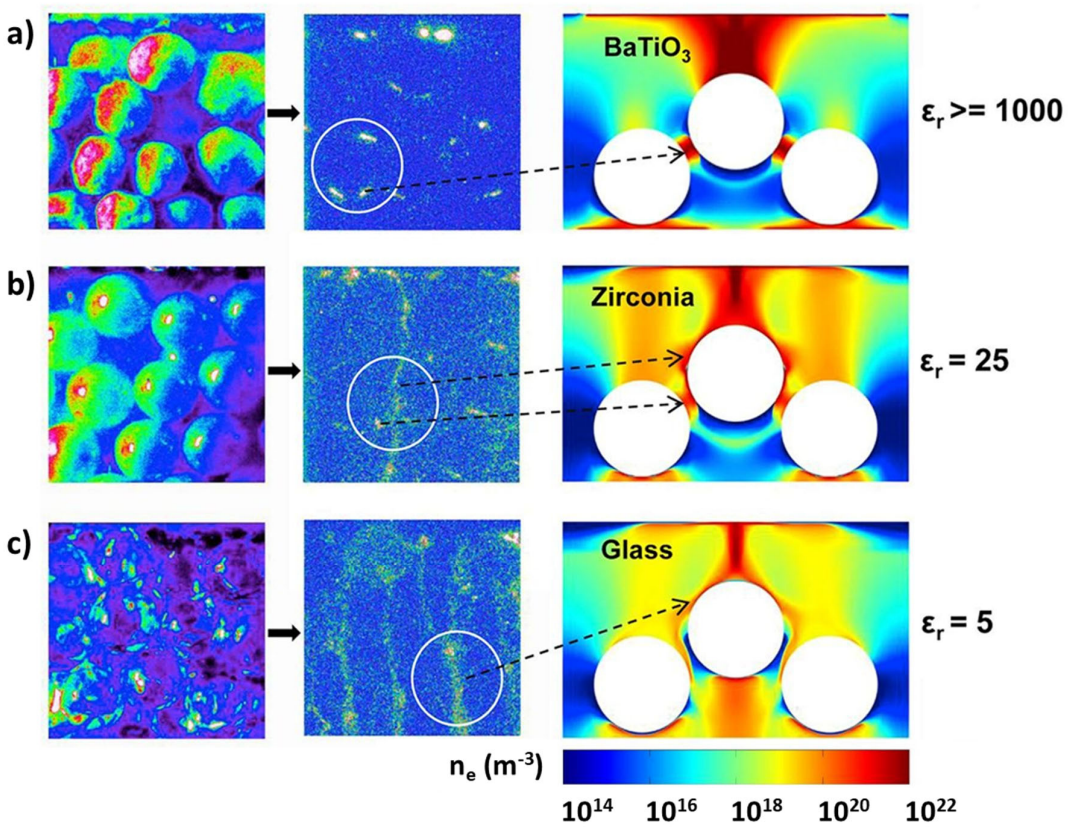

Figure 2. Fast ICCD camera imaging of visible light emission from the microdischarges in a packed bed DBD reactor, and electron number densities (n_e) from computer simulations. The figures on the left show the packing beads without discharges, while those in the middle show the ICCD images of plasma discharges for packing materials with different dielectric constants: a) $BaTiO_3$, ε_r=2600; b) ZrO_2, ε_r=25; c) glass, ε_r=5. The figures on the right show the corresponding electron number densities calculated with computational fluid dynamics simulations for the different values of ε_r. A transition from localized discharges at high ε_r (a) to surface discharges at low ε_r (c) can be observed. Reprinted from [32], Copyright (2018), with permission from Elsevier.

The discharge type is expected to have important implications for the chemical plasma-catalyst interactions, as it determines the spatial distribution of the plasma in the reactor and its distance to the surface. Indeed, before reactive plasma species can partake in the surface chemistry, they need to diffuse from the plasma to the catalyst surface. Consequently, the number of species that reaches the catalyst will depend on the distance between the plasma and the catalyst particles, as well as the lifetime of the species.

Interestingly, computational modelling by Wang *et* al. [32] revealed that the dielectric constant of the packing beads not only influences the discharge type, but consequently also the species formed in air

plasma, with high dielectric constants enhancing the concentration of N radicals and electrons, while slightly suppressing O and O_3. This is caused by the stronger polarization of the beads with higher dielectric constants, which leads to stronger electric field enhancement at the poles, and thus higher electron temperatures. The higher electron temperatures improve the electron impact dissociation of N_2, while lowering the fraction of the electron energy that goes into electron impact dissociation of O_2 [32]. This example illustrates that the dielectric constant of the packing can be used to enhance or suppress the formation of specific plasma species. More generally, we can envision that low dielectric constants (and thus lower electron temperatures) are more beneficial if vibrational excitation is desired, while high dielectric constants can enhance electron impact dissociation. Indeed, energy thresholds for vibrational excitation are much lower than for electron impact dissociation. For example, electron impact dissociation to the first vibrationally excited states of CH_4 or CO_2 requires a threshold energy in the range of 0.162-0.361 eV or 0.083-0.291 eV, respectively, depending on the mode that is excited [33]. Electron impact dissociation reactions of CH_4 or CO_2, on the other hand, have energy thresholds starting at 8.6 eV [34] and 7.5 eV [35], respectively.

Thus, the dielectric constant of the packing has a strong effect on the discharge type, with low dielectric constants favoring surface discharges along the beads, and high dielectric constants enhancing the formation of localized microdischarges between the beads. Consequently, the dielectric constant can be used to tune the discharge mode to optimize contact between plasma and catalyst. Indeed, it affects the distribution of the plasma between the beads, and thus whether plasma species are formed in the vicinity of the catalyst particles. In addition, the electric field enhancement due to polarization of the beads determines which plasma species are formed by certain electron impact processes.

3.2 Effect of metal particles on the discharge behavior

As described in previous section, it has been experimentally observed that the presence of a catalyst or support material in the discharge gap can alter the plasma behavior [31,32,36–38]. While previous section discussed the effect of the dielectric constant of the support (packing), some authors reported a similar behavior when the packing was loaded with catalyst. For example, Tu *et al.* [36] observed a change in the discharge type from filamentary discharges in an empty DBD reactor to a mixture of surface discharges and localized microdischarges when the reactor was packed with Ni/Al_2O_3. Moreover, the presence of a Ni/Al_2O_3 catalyst in the discharge gap did not only change the discharge behavior relative to the empty DBD, but also resulted in a much wider spatial distribution of the discharges compared to the DBD packed with only Al_2O_3 [36]. To determine the chemical effect of the catalyst in plasma catalysis, results should thus ideally be compared to the reactor packed with the same support material but without catalyst particles. However, even this approach is not conclusive, as the presence of catalyst nanoparticles also affects the discharge behavior compared to the bare support material. Indeed, the presence of various types of metal nanoparticles (e.g., Ni, Zr, Ag and Cu) has been

observed to cause expansion of the plasma, in addition to the effect of the support [36–38]. Furthermore, Kim *et al*. [37,38] illustrated that the loading of Ag nanoparticles on a zeolite support also enhanced the number of microdischarges. While packing the support in a DBD on itself already resulted in more, but less intense (i.e., lower current peaks) microdischarges, the effect was more apparent in the presence of Ag nanoparticles. Both the plasma expansion and the number of microdischarges were further enhanced at larger Ag loadings [37,38].

It is also noteworthy that these authors found that not all metals affected the discharge behavior in the same way, as Cu nanoparticles were less effective in plasma expansion and plasma-catalytic benzene oxidation compared to Ag [37]. In a follow-up work by the same research group [31], loading Ag on γ-Al_2O_3 was found to enhance streamer formation relative to pure γ-Al_2O_3, while the presence of Pt was detrimental to streamer propagation. Moreover, Ndayirinde *et al*. [39] found for plasma-catalytic NH_3 synthesis that the addition of different promotors (Ce, La and Mg) to Co-based catalysts significantly changed the discharge characteristics (e.g., plasma power and electrical current profile) of a DBD plasma. In other words, depending on their composition, the catalysts can act as "plasma modifiers", and thereby possibly affect the plasma chemistry. These results illustrate that different types of metals do not necessarily affect the discharge behavior in the same way. As such, a catalyst that is optimal from a chemical perspective, i.e., with regard to the surface reactions, might not be beneficial for the plasma physics. Such negative effects might be countered by choosing the support material accordingly. This would also imply that the optimal support material might change for different catalysts.

To summarize, the presence of metal nanoparticles can further affect the discharge behavior, in addition to the effect of the support. Metal nanoparticles may lead to expansion of the plasma, as well as a larger number of microdischarges, and their effect becomes more apparent for larger metal loadings [37,38]. Moreover, the physical interaction between the plasma and the catalyst nanoparticles varies for different metals [31,37], further hampering a direct comparison of their chemical effect.

3.3 Effect of the packing and reactor dimensions

In addition to the dielectric constant of the packing material, discussed in section 3.1, the diameter of the packing beads and the size of the discharge gap also strongly determine the discharge behavior in the reactor. Computational fluid dynamic simulations for DBD plasma in helium by Van Laer *et al.* [40,41] showed that smaller bead or gap sizes, as well as higher dielectric constants (and thus stronger polarizability), result in an enhancement of the electric field ~~and a drop in the electron density~~. However, the electric field enhancement stagnates at higher dielectric constants and this stagnation happens at lower values of ε_r for smaller beads or discharge gaps. Additionally, the enhancement of the electric field, as well as the smaller voids resulting from smaller bead sizes, cause a larger fraction of electrons to be lost through collision with the walls. Hence, smaller beads and higher dielectric constants can

enhance the electric field op to a certain point, but also result in a drop in the electron density. Since gas conversion requires both a high electric field and high electron density, smaller bead and gap sizes or higher dielectric constants are no longer beneficial after the electric field stagnates. As such, materials with low ε_r can benefit more from smaller bead and gap sizes, while materials with (very) high ε_r may benefit more from larger bead and gap sizes [40,41]. This agrees with results from CO_2 splitting experiments [42], which showed that smaller beads (100-200 µm) were more beneficial in case of SiO_2 (ε_r = 3.9) and Al_2O_3 (ε_r = 9), while the trend was inversed for ZrO_2 (ε_r = 25), for which larger beads (300-400 µm) gave higher conversions. However, narrowing the discharge gap generally resulted in higher CO_2 conversions for gap sizes in the range 250-1250 µm, regardless of the packing material [42]. Given that the dimensions of the packing and the discharge gap affect the electric field, and thus the electron temperature, these parameters may also affect the species formed in the plasma, similar to the dielectric constant, as discussed in section 3.1.

Next to the dielectric constant of the packing, many other factors determine the optimum packing size. Butterworth *et al*. [43] investigated the effect of packing particle size (180-2000 µm) on CO_2 splitting in a packed-bed DBD with Al_2O_3 or $BaTiO_3$ packing. Their results showed that smaller packing particles improved CO_2 conversion, but on the condition that the applied voltage is high enough to generate discharges in the voids between the packing materials. However, the use of smaller particles (and thus smaller voids) also increased the burning voltage and lead to partial discharging, i.e., not all the charge stored on the surface of the dielectric is transferred during a discharge cycle and thus less plasma is formed. The latter of course has a negative effect. As such, the authors illustrated that to (fully) benefit from the use of smaller particles, breakdown should be facilitated by using higher voltages or gas mixtures with a lower breakdown voltage (e.g., by adding noble gasses to the feed). Indeed, their results showed that for Al_2O_3 smaller particles improved CO_2 conversion in CO_2/Ar feed mixtures. However, the beneficial effect of smaller particles declined when increasing the CO_2 fraction, and for pure CO_2 small particle sizes became detrimental as no plasma could be generated for particles smaller than 850 µm. For $BaTiO_3$, on the other hand, plasma could still be generated in pure CO_2 for the smallest particles, likely due to electric field enhancement as result of the high dielectric constant. Yet, $BaTiO_3$ generally did not benefit from smaller particle sizes, except at the highest Ar fractions combined with plasma powers above 10 W [43].

Furthermore, smaller packing particles result in more contact points between the particles, where the electric field is enhanced, and can thus improve the number of localized microdischarges. As such, the packing size might be used to tune the volume of the plasma relative to that of the non-ionized gas in the reactor [44,45]. This explains why even materials with a high dielectric constant, like $BaTiO_3$, can benefit from smaller packing particles to some extent, as has been observed experimentally [46,47].

Indeed, for packings with high dielectric constants the discharges remain localized at the contact points between the beads, as discussed sections 3.1.

To summarize, not only the dielectric constant of the packing, but also the dimensions of the packing beads and of the discharge gap determine the discharge behavior. While the electric field is initially enhanced with rising dielectric constant and smaller bead or gap sizes, this trend is broken as the electric field stagnates. Consequently, the trends regarding bead size and discharge gap can be inversed for different packing materials, thus significantly complicating direct comparison between different experimental studies. Additionally, some packing materials can benefit significantly from smaller particle sizes, on the condition that a sufficiently high voltage is applied. Yet, smaller particles also raise the breakdown voltage, and can lead to partial discharging if the applied voltage is too low. Hence, the optimal packing and gap size depends on many parameters including the dielectric constant of the packing, the gas mixture, and the applied voltage.

3.4 Other material properties of the packing

In the previous sections we discussed the effect of the dielectric constant of the packing, the presence of metal nanoparticles, as well as the dimensions of the beads and the reactor, on the discharge behavior and electric field enhancement. However, many other material parameters of the packing may affect gas conversion in a DBD. For example, in an experimental study on DRM in a packed-bed DBD reactor, Michielsen *et al.* [48] observed that α-Al_2O_3 spheres gave higher conversions than γ-Al_2O_3 spheres of the same size. Since both packing materials have the same dielectric constant, this indeed indicates that other material properties play a significant role as well. An important difference between α- and γ-Al_2O_3 is the higher porosity of the latter, e.g., with pore volumes of 8.47 mm³/g vs. 500 mm³/g in ref. [48] for α- and γ-Al_2O_3, respectively. We could speculate that part of the gas may be protected from the plasma by diffusion into the pores, which raises the question whether plasma formation inside the pores is possible. Particle-in-cell/Monte Carlo collision simulations have shown that plasma streamers can only penetrate into pores with a diameter larger than the Debye length, which is typically in the order of 0.5-1 μm for air discharges in DBD [49]. Using T_e = 2.5 eV and $n_e = 3 \times 10^{19}$ m^{-3} from ref. [50], we can estimate a Debye length, $\lambda_{de} \approx 7430 \times (T_e/n_e)^{1/2} = 2$ μm for CH_4/CO_2 DBD plasmas. As the pore diameter of γ-Al_2O_3 in ref. [48] is determined to be 0.54 μm, this indicates the plasma is indeed not able to penetrate into the pores. This may explain why the γ-Al_2O_3 packing gave lower conversion, despite its higher porosity, as the gas inside the pores could not be converted by the plasma, due to a shielding effect. This result is striking, and different from thermal catalysis, where higher porosity is typically beneficial, enabling more catalyst surface area to participate to the reaction. It again illustrates the additional complexity of plasma catalysis, compared to e.g., thermal catalysis.

It is also noteworthy that most support materials have pore sizes in de microporous (< 2 nm) and mesoporous (2-50 nm) range [51], meaning that the plasma will typically not reach into the pores. This is important to keep in mind for plasma catalysis applications, as any catalyst particles that are present in the pores will not be in direct contact with the plasma, and can thus only be reached by plasma species via diffusion. How far the plasma species will be able to reach into the pores will thus depend on their lifetime and diffusion coefficient. This was discussed in a review by Kim *et al.* [52], who estimated diffusion lengths of 0.74 μm, 52 μm and 65 μm for $O(^1D)$, $O(^3P)$ and OH, respectively, based on lifetimes of 10 ns, 50 μs and 100 μs, respectively. Assuming a typical diffusion coefficient around 0.2 $cm^2\ s^{-1}$, similar to the values reported in ref. [52], we might expect diffusion lengths of 6.3-63 μm for vibrationally excited CH_4 and CO_2, with lifetimes in the range of 1-100 μs [10,53]. Similarly, for CH_x radicals in CH_4 DBD plasma, with lifetimes of < 5 μs (CH), < 30 μs (CH_2) and > 1 ms (CH_3) [10], diffusion lengths of < 0.45 μm, < 1.1 μm and > 200 μm may be reached, respectively. Note that the lifetimes and thus diffusion lengths are determined by the reactions in the plasma and will differ dependent on the gas mixture and reaction conditions, such as temperature, pressure and plasma power. Apart from radicals and excited species, ions and electrons might also diffuse into the pores. However, estimating their diffusion lengths is more complicated, as positive ions can be accelerated into the pores due to the negative charge accumulated at the pore walls, while electrons experience repulsion [51].

Next to physical affects, the chemical properties of the packing can also play a role. For example, some experimental studies have ~~reported~~ suggested that a higher basicity of the packing enhances CO_2 conversion in DRM and CO_2 methanation [17,24,26,54]. Indeed, it is known from thermal catalysis that basic sites on the support material interact with CO_2 due to the Lewis acidic properties of this molecule. Hence, a higher number of basic sites enhances CO_2 adsorption and can improve CO_2 conversion [55–57]. This effect likely also plays a role in plasma catalysis. For example, Mei *et al.* [17] studied plasma-catalytic DRM with Ni, Ag and Pt catalysts supported on γ-Al_2O_3, as well as bare γ-Al_2O_3 and observed that the trend in CO_2 conversion was consistent with the number of basic sites on the catalyst material. Additionally, Mikhail *et al.* [54] investigated plasma-catalytic CO_2 methanation using Ni/$CeZrO_x$ catalyst with various dopants (Cu, La, Mn, Co, Y, Gd and Sr) and observed that the amount of CH_4 produced (and CO_2 converted) generally improved with a higher percentage of medium basic sites compared to strong basic sites. This was attributed to strong basic sites mainly forming strongly-bound, unreactive surface intermediates, while CO_2 adsorbed on medium basic sites results in more reactive surface intermediates [54–56]. However, it is worth nothing that it is difficult to establish a clear correlation between basicity and CO_2 conversion in plasma catalysis, due to the many factors that can play a role. Moreover, the effect of a packing in plasma-catalytic DRM is further complicated by the myriad of products that can be formed. Indeed, in the abovementioned work by Michielsen *et al.* [48] the selectivities and CO/H_2 ratio showed significant variation with packing material (SiO_2, α-Al_2O_3, γ-Al_2O_3, ZrO_2 and $BaTiO_3$) and bead size (1.25-2.24 mm).

To summarize, in addition to the dielectric constant, metal loading, packing bead and reactor gap size, many other packing properties can affect the conversions and product selectivities. These include other physical properties, such as porosity and pore size, which determine the fraction of the gas mixture and catalyst particles that are in direct contact with the plasma. On the other hand, chemical properties, such as basicity, may also play a role.

3.5 Comparing packing materials at different residence times

While various packing properties can affect the conversion, the optimal packing in terms of conversion can also differ depending on the residence time of the gas in the reactor. This was illustrated by Uytdenhouwen *et al*. [58], who demonstrated the existence of a partial chemical equilibrium (PCE) for CO_2 splitting in a DBD reactor. The authors found that the CO_2 conversion stabilized at different values depending on the size of the discharge gap and the choice of packing, but the residence time needed to reach PCE also changed independently of the conversion at PCE. This is illustrated in Figure 3, which shows the CO_2 conversion as function of the residence time in a DBD reactor with a 455 µm (a) and a 4705 µm (b) discharge gap. For the 455 µm discharge gap, the PCE shifted to higher conversion when SiO_2 was packed in the reactor, relative to the empty reactor. However, packing ZrO_2 into the reactor resulted in the same PCE as the empty reactor, but a longer residence time was required to reach the same conversion. In other words, the ZrO_2-packed and empty reactor performed the same at long residence times, while the empty reactor performed better at short residence times. For a larger (4705 µm) gap, the trend changed and ZrO_2 reached the highest conversion at PCE, followed by SiO_2, with the empty reactor giving the lowest conversion (see Figure 3) [58]. As such, even direct comparison of two different packing materials in the same DBD reactor is not necessarily straightforward, as the observed trend in conversion might change for different residence times.

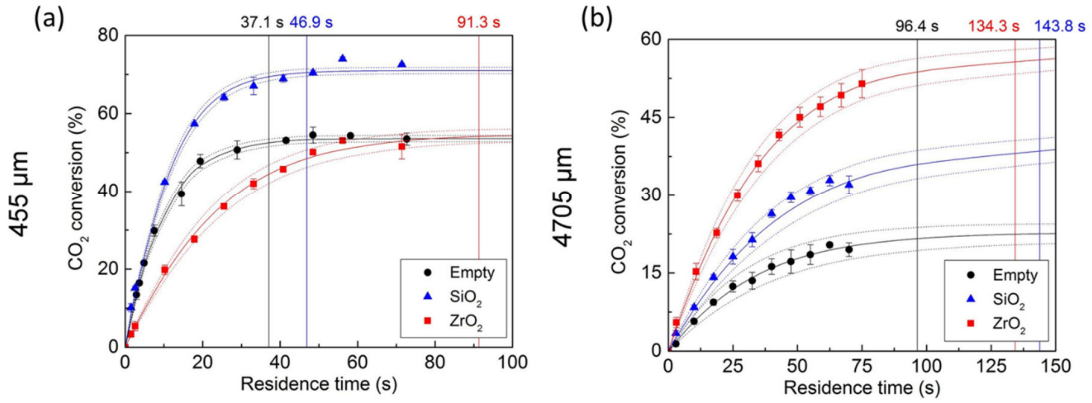

Figure 3. CO_2 conversion as function of the residence time at 30 W and 1 bar, for a gap size of 455 µm (a) and 4705 µm (b). The CO_2 conversion in an empty DBD (black curve) is compared with that of a DBD packed with SiO_2 (blue) or ZrO_2 (red) beads. An apparent first-order reversible reaction fit is

applied for all graphs (solid lines) with its 95% confidence interval (dotted lines). The time points at which the fits reach 98% of the end conversions of CO_2 dissociation are indicated for each case by the vertical lines. Reprinted from [58]*, Copyright (2019), with permission from Elsevier.*

3.6 Many intertwined factors: leading to complexity, but also many degrees of freedom

As illustrated in sections 3.1 to 3.5, many variables affect the physical behavior of the plasma in plasma catalysis. Indeed, the dielectric constant of the support (i.e., packing material) [31,32], the metal loading [37,38], the type of metal particles [31,37], as well as the size of the packing beads [40] and the discharge gap [41] can affect the electric field and discharge type. On one hand, this determines the spatial distribution of the plasma in the reactor and thus whether it is formed in the vicinity of the catalyst particles. On the other hand, the change in electric field alters the electron impact processes and consequently the conversion and the species formed in the plasma [32]. Moreover, the trends observed when varying bead or gap sizes can change for different values of the dielectric constant, or vice versa, due to stagnation of the electric field at high dielectric constants and small bead or gap sizes [40–42]. Next to material properties related to the change in discharge behavior, other parameters also play a role in plasma catalysis. For example, the porosity and pore size determine the fraction of catalyst particles that can interact with reactive species formed in the plasma. Indeed, the plasma cannot penetrate into pores smaller than the Debye length [49], meaning that plasma species need to have a sufficient lifetime to reach the catalyst particles in these pores via diffusion. Furthermore, the observed trends in terms of conversion between packing materials can even change depending on the residence time, as the position of a PCE and the rate at which this is reached can vary independently [58].

Since all parameters above (and likely more) can affect the outcome of plasma-catalytic experiments, a straightforward comparison of experimental results for different packing types is significantly hampered. This highlights the need for standardized experimental setups and elaborate documentation of packing properties, to disentangle the various effects and make progress in this important research field. On the other hand, since many parameters can affect the experimental results, there are also many degrees of freedom for optimization of plasma-catalytic systems, which should be further exploited, but in a controlled way.

4 Chemical effects

Rational design of plasma-catalytic systems also requires a good understanding of the chemical interactions that occur between the plasma and the catalyst. By identifying the conditions (e.g., temperature, plasma power, gas composition, catalyst) for which synergy occurs, and by comparing experimental results with computational kinetics studies, the mechanisms behind the synergistic effect may be elucidated. In addition, chemical kinetics models can also be employed to screen for possible conditions at which synergistic effects may be achieved. However, a direct comparison between modelling and experiments is not straightforward, due to the simultaneous occurrence of both chemical and physical interactions.

In the following subsections, we will discuss various chemical effects that might play a role in plasma catalysis, revealed by both experiments and modelling. Here, we do not exclusively focus on DRM, but also discuss studies for other plasma-catalytic reactions (e.g., NH_3 synthesis, SRM, CO_2 hydrogenation) that are conceptually simpler and often more well studied, as these studies provide insights that are applicable to plasma catalysis in general and thus also relevant for plasma-catalytic DRM. In section 4.1, we will illustrate how reactive plasma species can improve reactant activation on the catalyst surface, which leads to enhanced conversion, but only within specific temperature ranges. We will compare the effect for endothermic and exothermic reactions. Section 4.2 will illustrate how plasma-catalyst synergy can alter the trends in catalyst reactivity relative to thermal catalysis. In section 4.3, we will discuss the difference between vibrationally excited molecules and radicals in inducing plasma-catalyst synergy.

Next, Section 4.4 will elaborate on experimental methods developed to quantify plasma-catalyst interactions and to measure plasma-induced surface heating. In section 4.5, we will illustrate how plasma-catalyst synergy can influence the product selectivities based on examples from plasma-catalytic CO_2 hydrogenation. Section 4.6 will provide insights from our own modelling work, to demonstrate the role of plasma-catalytic CO hydrogenation as a possible pathway for CH_3OH production, as well as competitive reactions that are a bottleneck for plasma-catalytic DRM. In section 4.7, we will propose solutions for the issues associated with oxygenate synthesis illustrated in the previous section.

In section 4.8, we will discuss how a plasma typically contains a wide variety of radicals, which can strongly affect the product distribution, as well as the optimal choice of catalyst. Section 4.9 will explain how these radicals can react with adsorbates via Eley-Rideal (E-R) reactions, which are likely important in plasma catalysis, although much is still unknown about the associated kinetics. Finally, in section 4.10, we will emphasize how a detailed understanding of the physical plasma-catalyst interactions is important to optimize the chemical interactions, which depend on the flux of plasma species to the surface and thus the contact between the plasma and the catalyst.

4.1 Temperature dependence of plasma catalysis

Experimental studies on plasma-catalytic DRM and steam reforming of CH_4 (SRM) [53,59] as well as NH_3 synthesis [60] have observed the occurrence of plasma-catalyst synergy to be temperature dependent, i.e., requiring higher temperatures to become active, similar to thermal catalysis. This indicates that reactive plasma species may participate in the catalyst surface chemistry, enhancing specific surface reaction steps. Because of this, the surface reaction rates are enhanced, but only at temperatures for which the surface reaction steps that are not directly affected by the plasma, become thermally active [60,61]. In sections 4.1.1 and 4.1.2, we discuss this for DRM (and SRM), as well as NH_3 synthesis, as examples of an endothermic and exothermic reaction, respectively. Next, we provide a more general comparison on the effect of plasma-catalyst synergy for endothermic and exothermic reactions, in section 4.1.3.

4.1.1 Plasma-catalyst synergy in DRM and SRM

Specifically for DRM, a temperature dependence of plasma-catalyst synergy was observed by Kim *et al*. [59], whose results are displayed in Figure 4. The authors compared DRM in a DBD without catalyst (empty or packed with Al_2O_3) to thermal and plasma catalysis with a Ni/Al_2O_3 catalyst, at different temperatures. As can be seen in Figure 4 a), plasma alone or with Al_2O_3 packing (red and green curves) gave significant CH_4 conversions at low temperatures (< 600 K), but the conversion diminished at higher temperatures. Thermal catalysis (black curve) naturally showed an opposite trend, and the conversion rose with temperature as the catalyst became thermally active. Plasma catalysis (blue curve) displayed a similar conversion as the plasma without catalyst at low temperatures (< 600 K), but outperformed thermal catalysis at higher temperatures. Thus, synergy is only observed at temperatures where the catalyst also becomes active for thermal catalysis, clearly indicating the involvement of surface reactions. Similar observations were made for the H_2 yield, displayed in Figure 4 b). Because of the temperature dependency and the fact that plasma alone gave negligible conversion at high temperatures, the authors attributed the observed synergy to vibrationally excited CH_4. This would lower the activation barrier for the presumed rate-limiting step, i.e., CH_4 dissociative adsorption, and thus enhance the surface reaction rates [59].

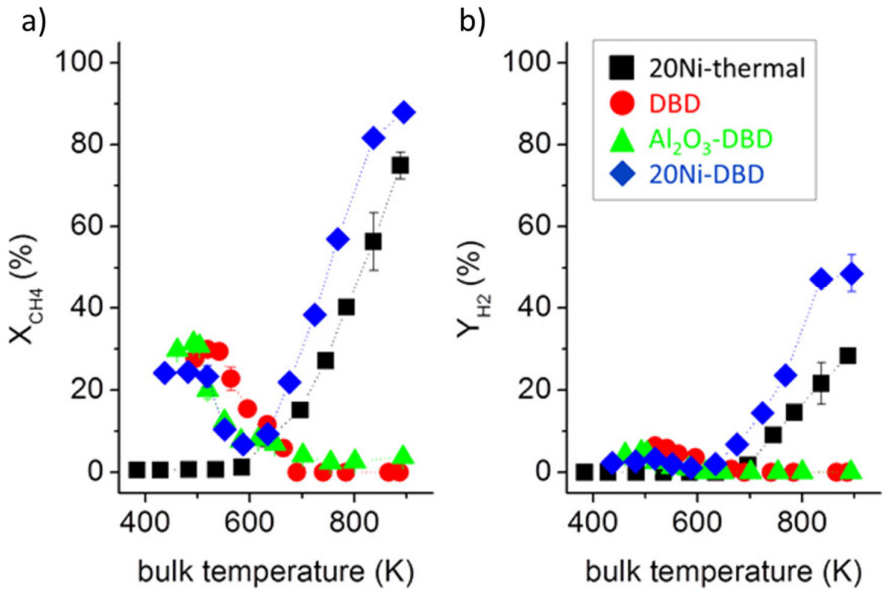

Figure 4. Profiles of a) CH_4 conversions (X_{CH4}) and b) H_2 yields (Y_{H2}) for 20wt% Ni/Al_2O_3 in thermal catalysis (black), an empty DBD (red), DBD packed with Al_2O_3 (green) and DBD packed with 20wt% Ni/Al_2O_3 (blue). Reaction conditions: 100 mg packing; CH_4:He:CO_2 = 1:2:1; total flow rate of 20 mL min^{-1}; 1 atm; 10 W. The results demonstrate the occurrence of plasma-catalyst synergy above 600 K. Reprinted with permission from [59]. *Copyright (2016) American Chemical Society.*

Similar behavior was also observed for SRM by Nozaki *et al*. [53]. In that study, the CH_4 conversion in a DBD packed with a Ni/SiO_2 catalyst exceeded the combined conversions of the empty DBD and thermal catalysis at temperatures between 673 – 873 K. Moreover, CH_4 conversions beyond the thermal equilibrium could be reached, indicating that plasma-enhancement of the surface reactions does not only improve the kinetics, but can also circumvent thermodynamic limitations to some extent [53].

Hence, these studies demonstrate that plasma can facilitate CH_4 activation on the catalyst surface, possibly by destabilizing the C-H bonds through vibrational excitation. The latter is further supported by the results of molecular beam studies, which show that vibrational excitation of the asymmetric C-H stretch mode in CH_4 enhances its dissociative adsorption [62,63]. However, this plasma-catalyst synergy only becomes effective above a certain temperature.

4.1.2 Plasma-catalyst synergy in NH_3 synthesis

To further elucidate the mechanisms behind plasma-catalyst synergy, studies of more straightforward reaction systems, such as plasma-catalytic NH_3 synthesis, can also be useful. Both experimental [60] and modelling [61] studies on plasma-catalytic NH_3 synthesis have demonstrated that plasma-catalyst synergy only occurs past a certain temperature threshold, like in DRM and SRM. However, unlike DRM and SRM, NH_3 synthesis is exothermic and thus equilibrium-limited at high temperatures. While

plasma-catalysts synergy can also push the NH_3 concentrations beyond the equilibrium composition, the exothermicity of the reaction eventually leads to a drop of the NH_3 concentrations at higher temperatures [60,61]. This behavior was clarified via modelling by Mehta *et al.* [61], who illustrated the effect of plasma-enhanced N_2 dissociative adsorption (e.g., due to N_2 vibrational excitation or dissociation in the plasma) on the surface kinetics. The authors illustrated that at low temperatures, plasma-enhanced N_2 activation has no effect, as the reaction becomes rate-limited by the slow hydrogenation and NH_3 desorption steps. Yet, as these reactions become thermally activated at higher temperatures, plasma-enhanced N_2 dissociation leads to improved NH_3 formation rates and concentrations. The faster NH_3 formation rate also causes an imbalance between NH_3 formation and destruction, explaining why the NH_3 concentrations can exceed the thermal equilibrium. However, as the temperature rises, the catalytic pathways for NH_3 destruction also become more active, causing the NH_3 concentration to reach a maximum and subsequently decline [61].

As discussed in section 3.2, the presence of metal nanoparticles on the support material can alter the discharge behavior of the plasma, thus possibly leading to a change in conversion. It is therefore noteworthy that on top of the qualitative agreement between experimental [60] and modelling results [61], there is also direct evidence of plasma-enhanced surface reactions [64,65]. More specifically, Barboun *et al.* [64] demonstrated the formation of surface-bound NH_x* on Ni/γ-Al_2O_3 that was sequentially treated with N_2 and H_2 plasmas to exclude the formation of NH_x radicals in the plasma. The formation of surface-bound NH_x* could indeed be attributed to plasma catalysis, as subsequent N_2 and H_2 exposure under thermal conditions without plasma did not form these species. In a follow-up work [65], SiO_2-supported Fe, Ni, Co and Pt catalysts were treated with a N_2 plasma, followed by temperature programmed reaction with H_2 gas to eliminate the possibility of gas-phase NH_3 synthesis. Using this method, NH_3 production via thermal hydrogenation of surface-bound N* was indeed observed. However, if the catalyst was not treated with N_2 plasma, but instead exposed to N_2 at 200 °C, no NH_3 could be formed. Hence, this proves that the plasma was essential in forming the adsorbed N*.These studies thus provide clear evidence that plasma enhances activation of N_2 on the catalysts surface.

In summary, plasma can facilitate N_2 dissociation on the catalyst surface, leading to enhanced NH_3 concentrations in the gas-phase, which can even exceed the thermodynamic equilibrium. Yet, a certain light-off temperature is still required to activate the subsequent surface reaction steps, while too high temperatures cause the NH_3 concentration to revert to the equilibrium composition.

4.1.3 Plasma-catalyst synergy: endothermic vs. exothermic reactions

As mentioned above, both DRM and SRM are endothermic reactions and thus equilibrium-limited at low temperatures, while NH_3 synthesis is exothermic and becomes limited by the thermodynamic equilibrium at high temperatures. As such, plasma-catalyst synergy follows a different temperature

dependence for these reactions. Mehta *et al.* [66] recently reviewed the potential of plasma catalysis for DRM and NH_3 synthesis, as examples of processes that operate in different limiting regimes.

In Figure 5 we schematically illustrate the effect of plasma-enhancement of the reactant activation step (i.e., dissociative adsorption) on the conversion for endothermic and exothermic reactions, for which this step is rate-limiting. For the purpose of this discussion, we define plasma-enhancement as the destabilization of the reactant through vibrational excitation or dissociation in the plasma, leading to more facile reactant activation on the surface. Note that Figure 5 does not include any conversion that takes place in the gas phase or any alteration of other surface reaction steps. Figure 5 a) shows how endothermic reactions are affected by plasma-enhanced reactant activation. Since endothermic reactions are both kinetically and equilibrium-limited at low temperatures, enhanced conversions occur exclusively at temperatures below which the catalyst becomes active for thermal catalysis. At temperatures above the equilibrium-limited regime, plasma-enhancement has limited potential, although it can still be useful to activate catalysts that are strongly kinetically limited, by reactant activation. Such catalysts require high temperatures to become catalytically active and thus both the thermal and plasma catalysis curves in Figure 5 a) will be shifted to the right. Less active catalysts in terms of conversion might be chosen if they offer advantages with respect to product selectivity. For endothermic reactions, higher temperatures will result in increased conversion, yet plasma-enhancement will also become redundant, as the equilibrium and kinetic limitations applicable to thermal catalysis will disappear. As such, the optimal operating temperature for plasma catalysis will be lower than for thermal catalysis.

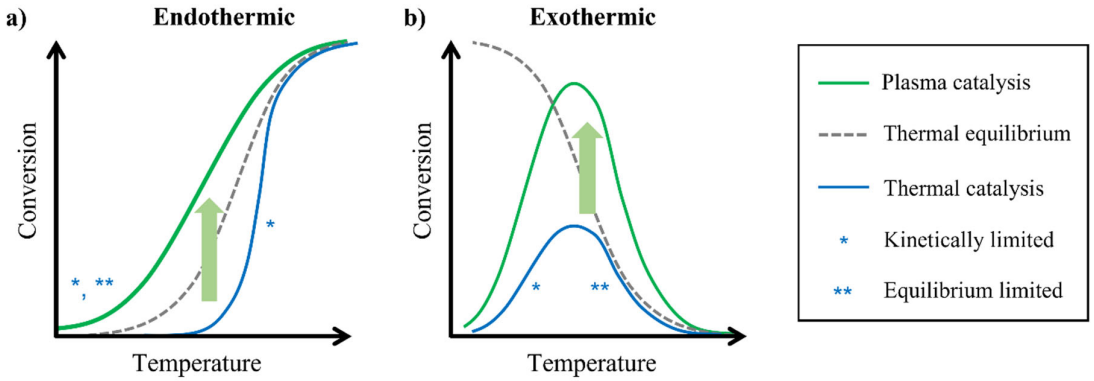

Figure 5: Schematic representation of the effect of plasma-enhanced reactant activation for a) endothermic and b) exothermic reactions that are rate-limited by this reaction step.

The effect of plasma-enhanced reactant activation on exothermic reactions is displayed in Figure 5 b) and is explained in more detail above, where we discussed the work by Mehta *et al.* on plasma-catalytic NH_3 synthesis [61]. Exothermic reactions exhibit an optimal operating temperature, due to the kinetic and equilibrium limitations at low and high temperatures, respectively. Strong plasma-enhancement

improves the conversions in both the kinetically and equilibrium-limited regime. This enables conversions closer to the equilibrium composition at low temperatures, while it allows for conversions beyond the thermal equilibrium at higher temperatures (see Figure 5 b). Nevertheless, an optimal temperature will still exist where the conversion reaches a maximum. Contrary to endothermic reactions, the maximum conversion for plasma-enhanced exothermic reactions corresponds to the temperature at which plasma-enhancement has the strongest impact.

Note that the discussion above features reactions that are endergonic in part of the temperature range. However, some reactions are never limited by the equilibrium, i.e., when the reactants are not the thermodynamically favored products at any temperature. Nevertheless, the equilibrium composition can still change with temperature, meaning that depending on the temperature different products will be favored. An example of this is the partial oxidation of CH_4, which favors a mixture of non-combusted CH_4 and complete oxidation products (H_2O, CO_2) at low temperatures (< 900 K) or syngas (CO/H_2) at high temperatures (> 900K) [67,68]. For such processes, plasma-enhancement can aid in circumventing the kinetic limitations, allowing the reaction to occur at lower temperatures and enabling the formation of products that are thermodynamically favored in the low temperature range. On the other hand, it might also shift the temperature at which transition to a different equilibrium composition occurs, i.e., by destabilizing molecules that would otherwise be thermodynamically favored at that temperature.

In conclusion, plasma can facilitate reactant activation on the catalyst surface, which can enhance the conversion for specific temperature ranges, depending on whether the reaction is endothermic or exothermic. For both types of reactions, a certain light-off temperature must first be exceeded to thermally activate surface reaction steps that are not directly affected by the plasma, before plasma-catalyst synergy is observed. For endothermic reactions (like DRM and SRM), plasma catalysis can subsequently circumvent the kinetic and equilibrium limitations that exist at low temperatures, yet becomes redundant at (very) high temperatures. For exothermic reactions (like NH_3 synthesis) plasma-catalyst synergy can (partially) lift the kinetic limitation at low temperatures and the equilibrium limitations at higher temperatures, although the conversion will eventually revert to the thermodynamic equilibrium if the temperature rises further.

4.2 Effect of plasma-catalyst synergy on trends in catalyst reactivity

In this section, we will briefly explain some important principles that govern trends in catalyst reactivity for thermal catalysis, namely the existence of scaling relations and the volcano curve (section 4.2.1). Subsequently, in section 4.2.2, we will discuss how these trends are affected by plasma-enhancement of the reactant activation step, and in section 4.2.3 we will illustrate how this applies to the specific case of CH_4 conversion. Finally, in section 4.2.4 we will provide insights in how the choice of catalyst affects the possibility of reaching product concentrations beyond the thermal equilibrium. Indeed, a thorough

understanding of these mechanistic changes is required to predict the optimal catalyst for plasma catalysis.

4.2.1 Scaling relations and the volcano curve

An important concept in thermal catalysis is the existence of scaling relations, i.e., correlations between the adsorption energies of surface intermediates that bind to the surface through the same atom(s). These scaling relations exist not only for the adsorbate energies, but also for the energies of the surface transition states. Consequently, they determine the activation barriers and reaction energies of the reactions on the catalyst surface. Due to scaling between the adsorbate and transition state energies of the different reaction steps, it is generally not possible to independently vary the activation barrier (and rate constant) of a single reaction step. These scaling relations often also result in volcano behavior, i.e., plotting the catalyst activity vs. the binding strength of a specific adsorbate results in a curve with a maximum, usually for catalysts with intermediate binding strength. This optimum at intermediate binding strength results from a monotonic rise in the rate of reactant activation and a decline in that of product desorption with growing binding strength [69]. The volcano behavior is schematically represented in Figure 6. While strongly binding catalysts can easily break the bonds in the reactant molecules, the formation of new bonds and product desorption from the surface is difficult. Weakly binding catalysts, on the other hand, allow for easy desorption, but struggle with breaking bonds. Consequently, the highest reactions rates are typically achieved at intermediate binding strengths, for catalysts that have a balanced reactivity towards both reactant activation and product desorption.

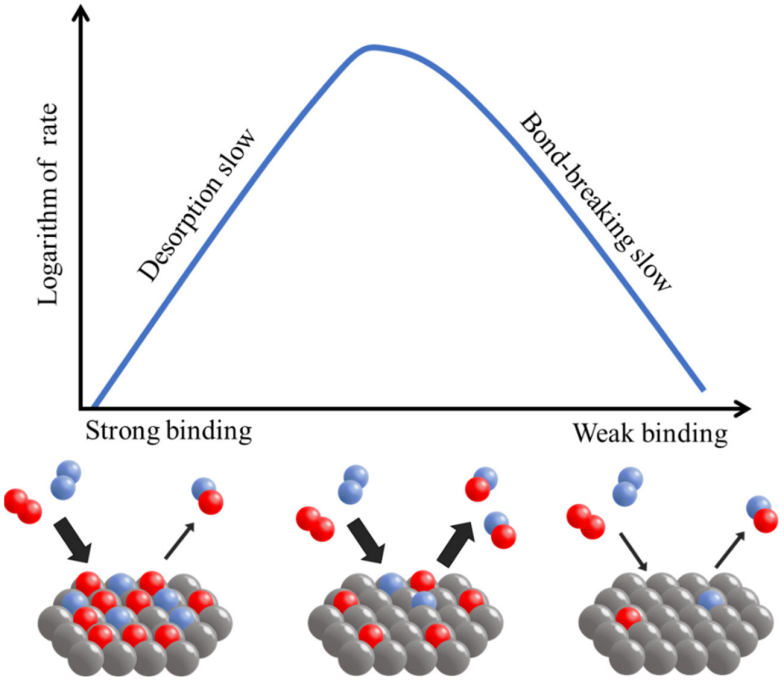

Figure 6. Schematic representation of volcano behavior: on strongly binding catalysts, reactant activation is facile and desorption slow, while on weakly binding catalysts, bond-breaking is difficult and desorption easy. Consequently, the optimal catalyst and highest rate are located at intermediate binding strength.

4.2.2 Change of the volcano curve due to plasma-enhancement

As discussed in section 4.1, various experimental works [53,59,60] have observed a temperature dependence in the occurrence of plasma-catalyst synergy, which indicates that catalyst surface reactions play a role in the chemistry. Indeed, even when vibrational excitation lowers the barrier for reactant dissociation on the surface, a certain temperature will still be required to surpass the remaining part of the barrier. Alternatively, if reactant activation on the surface is strongly enhanced or even omitted due to gas-phase dissociation, a subsequent surface reaction becomes rate-limiting. In this case, the new rate-limiting step needs to become thermally activated for plasma-enhancement to be effective [61].

Since the rate-limiting reaction step changes for different catalysts, a shift of the rate-limiting step due to plasma-enhancement can also alter the optimal catalyst material. This was illustrated in a computational study by Mehta *et al.* [70] using a microkinetic model for NH_3 synthesis in which the barrier for N_2 dissociative adsorption was lowered by vibrational excitation. Their results are shown in Figure 7, which demonstrates that enhanced N_2 dissociation can improve the rates of NH_3 synthesis, but only on catalysts that are rate-limited by N_2 dissociation. This is the case for catalysts that bind N* weakly or intermediately, such as Ru, Rh, Co, Ni, Pt and Pd, while strongly binding catalysts, like Fe,

do not benefit from vibrationally excited N_2. For some of the intermediately binding catalysts (Ru and Rh), the enhancement of the N_2 dissociation step causes subsequent reaction steps to become rate-limiting. Therefore, these catalysts do not benefit further from the plasma-enhancement, and the optimum of the volcano curve shifts towards more weakly binding catalysts. The authors also support their findings with experimental results. However, it is worth mentioning that the difference in performance between the catalyst in the experiments is less extreme than predicted by the model when viewed logarithmically. This indicates that other effects, like Eley-Rideal reactions (see section 4.9) likely also play a role. Yet, the conclusion of this study is still important, as it illustrates how plasma catalysis can be used to circumvent the scaling relations for bond dissociation normally present in thermal catalysis, by weakening (or breaking) bonds in the plasma [70]. Similar results have also been reported by other microkinetic studies for NH_3 synthesis [61,71], N_2 oxidation [72,73], non-oxidative coupling of CH_4 [74], CO_2 hydrogenation [75] and CH_4 partial oxidation [76].

Hence, by improving the initial reactant activation step on the catalyst surface, plasma can enhance the rates on intermediately and weakly binding catalysts, which are rate-limited by this reaction step. Moreover, the enhanced reactant activation can also shift the optimum in the rate volcano to more weakly binding metals if subsequent reaction steps are easier on these catalysts [70].

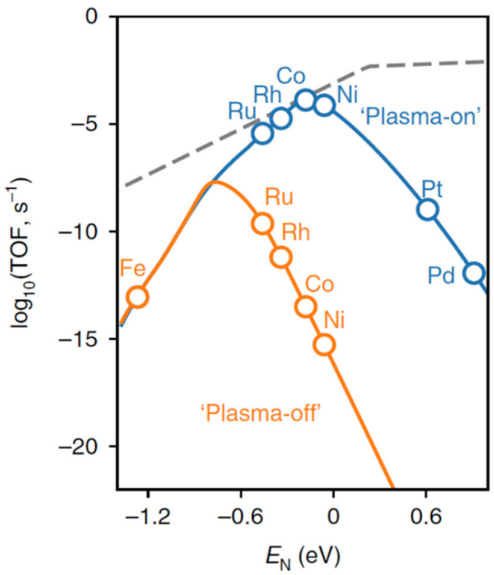

Figure 7. Predicted effect of N_2 vibrational excitation on the turnover frequencies (TOFs) of NH_3 synthesis (plasma-on), compared to those for thermal catalysis (plasma-off). Rates on (211) surfaces with reaction conditions: 1 atm, T_{gas} = 473 K, T_{vib} = 3000 K, conversion = 1%. The dashed lines are the maximum possible rates for the hydrogenation reactions according to Sabatier analysis. Lower (negative) values of E_N correspond to catalysts that bind N strongly, high (positive) values of E_N correspond to catalysts that bind N* weakly. Reprinted from P. Mehta, P. Barboun, F.A. Herrera, J.*

Kim, P. Rumbach, D.B. Go, J.C. Hicks, W.F. Schneider, Overcoming ammonia synthesis scaling relations with plasma-enabled catalysis. Nat. Catal. 1 (2018) 269–275. https://doi.org/10.1038/s41929-018-0045-1. With permission from Springer Nature.

4.2.3 Effect of plasma-catalyst synergy on the volcano curve for CH_4 conversion

Nevertheless, it is important to keep in mind that plasma-enhancement does not necessarily shift the top of the volcano curve for all reactions. For NH_3 synthesis, the enhanced N_2 activation causes a subsequent reaction step to become rate-limiting. Because the new rate-limiting step, i.e., NH_x* hydrogenation, occurs more easily on more weakly binding catalysts, the maximum in the volcano curve will shift in that direction. This is also indicated by the dotted grey line in Figure 7, which represents the maximum possible rates for the hydrogenation reactions. However, for reactions where the new rate-limiting step does not happen more easily on the more weakly binding catalysts, a change of the optimal catalyst will not occur. This might, for example, be expected for DRM or SRM to produce syngas (CO/H_2).

Figure 8 illustrates the reaction and activation energies for C-H bond scission in CH_x (x = 4-2) on both Cu(211) and Ni(211) surfaces. The effect of plasma-enhanced CH_4 activation via vibrational excitation (grey arrows) and dissociation (black arrows) in the plasma is schematically represented. Although vibrationally excited CH_4 can undergo dissociative adsorption with a lower activation barrier compared to ground-state CH_4, the barrier is typically not lowered by the total energy difference between these two states. Instead, the barrier will be lowered by the energy difference multiplied with an efficiency factor between 0 and 1, as indicated by the dotted lines in Figure 8. Next to vibrational excitation, a molecule can also be dissociated in the plasma (black arrows), e.g., via electron impact dissociation. However, this requires a much higher energy compared to vibrational excitation and is thus less energy efficient. Yet, some dissociation in the plasma is unavoidable due to the lower threshold energies for electron impact dissociation, compared to those for electron impact ionization [34], which is required to form and sustain the plasma. As can be seen in Figure 8, thermal dissociative adsorption of CH_4 is much easier on Ni(211) compared to Cu(211). Indeed, Ni-based catalysts are widely used for DRM and SRM in thermal catalysis, due to their high catalytic activity for these reactions (and low price compared to Rh, Ru, Pt and Pd) [6,77]. If the initial dissociation step is enhanced or omitted, because of the presence of radicals (dissociation in the plasma; black arrows in Figure 8), subsequent C-H bond scission steps remain. Just like the dissociation of CH_4, the CH_3* and CH_2* dissociation steps exhibit higher barriers on Cu(211), due to the weaker binding (i.e., more noble) character of this metal. As such, it is expected that these or other bond-breaking steps will become rate-limiting on weaker binding catalysts when CH_4 dissociation is enhanced, disabling a (further) shift of the volcano maximum to lower binding strengths. This is important to consider for DRM (and also SRM).

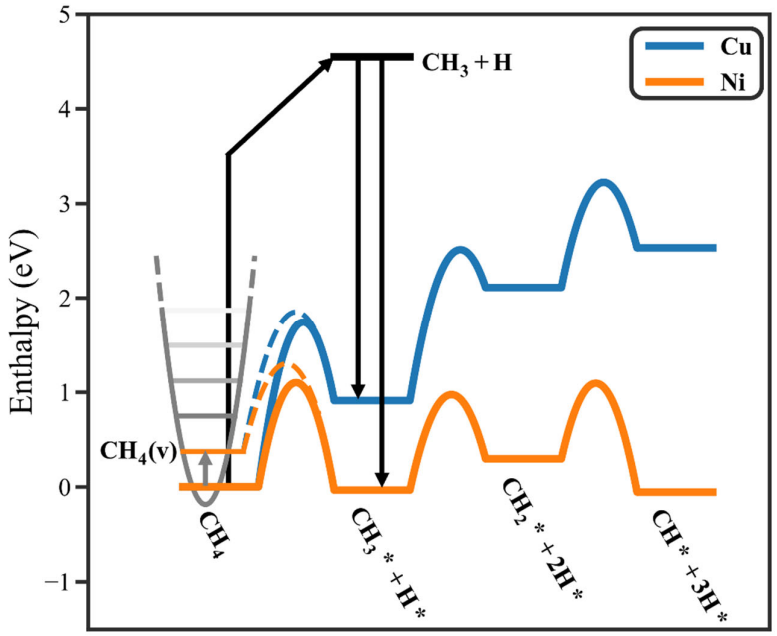

Figure 8. Reaction and activation enthalpies of C-H bond scission in CH_x (x = 4-2) on Cu(211) and Ni(211) surfaces. The effects of vibrational excitation and dissociation in the plasma are schematically represented with grey and black arrows, respectively. Based on data taken from the CatApp database [78] *and the NIST chemistry webbook* [79].

The reasoning above is supported by the work of Engelmann *et al*. [74], who constructed a microkinetic model to study the effect of vibrational excitation on CH_4 non-oxidative coupling. Their results are shown in Figure 9, which compares the TOFs (a, b) and surface coverages (c, d) for thermal and plasma catalysis, respectively. As can be seen from Figure 9 a) and b), the maximum of the CH_4 consumption volcano remains around approximately the same CH_3* binding strength if CH_4 activation is enhanced by vibrational excitation. Consequently, the intermediately binding metals, located near the volcano summit (such as Pt, Rh and Pd), still clearly outperform the weakly binding metals (e.g., Cu, Au and Ag). Finally, similar to NH_3 synthesis, the most strongly binding metals do not benefit from vibrational excitation at all, as these are rate-limited by difficult product desorption and surface poisoning [74].

However, it is important to stress that the situation changes when plasma-produced radicals are also accounted for. Indeed, as we will discuss in section 4.8, the rate volcano will change if the catalyst is in contact with complex mixtures that contain a wide variety of radicals. Radicals are not only formed in the plasma through electron impact dissociation of the reactants, but subsequent gas-phase reactions also form a wide variety of other radicals. In contrast to vibrational excitation or gas-phase dissociation of the reactants, these secondary radicals can enhance other (difficult) surface reaction steps, next to the initial reactant activation step. In that case, also for CH_4 conversion, the rates will rise considerably on

the weakly binding metals, and consequently, the maximum in the volcano curve will shift to the most weakly binding catalysts [74].

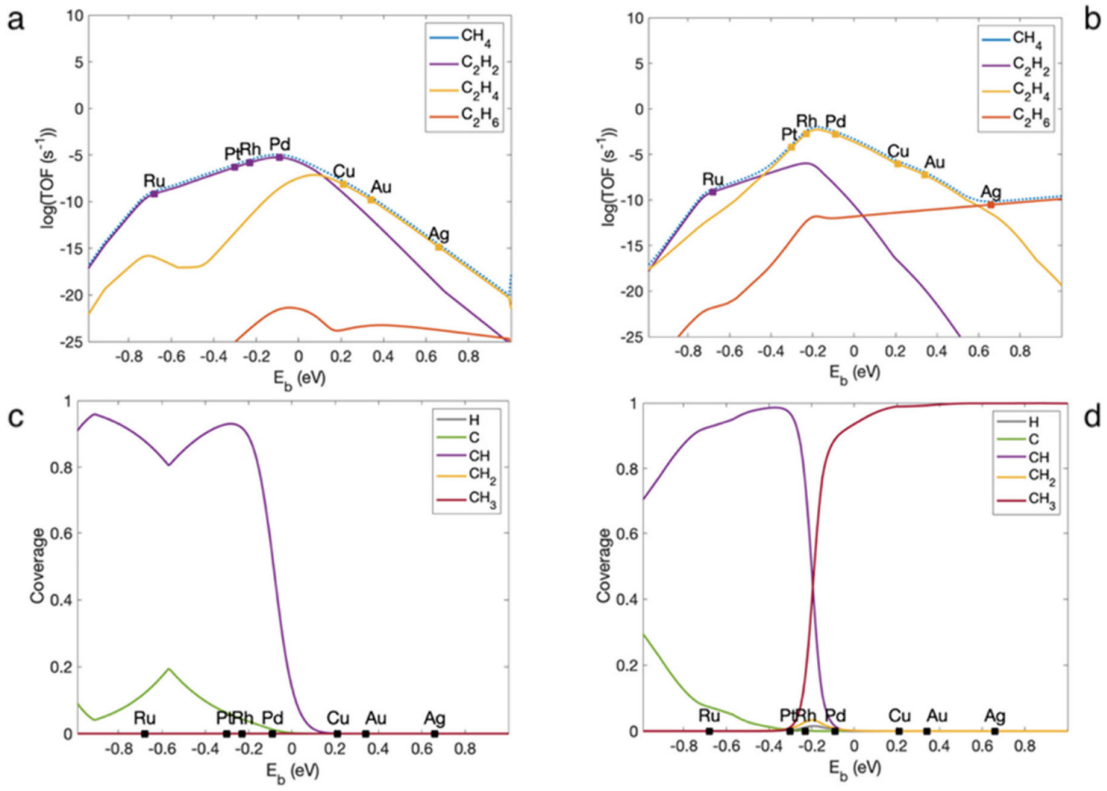

Figure 9. Steady-state TOFs (a, b) and coverages (c, d) for CH_4 non-oxidative coupling in thermal catalysis (a, c) and with vibrationally excited CH_4 at T_{vib} = 1500 K (b, d). The values are plotted against the binding energy (E_b) of CH_3. Low (negative) values of E_b correspond to strongly binding catalysts, high (positive) values of E_b correspond to weakly binding catalysts. Reprinted with permission from* [74]. *Copyright (2020) American Chemical Society.*

Most remarkably, Figure 9 a) and b) also illustrate that while the top of the CH_4 consumption volcano does not shift much, vibrational excitation can strongly affect the volcano curves of the individual products. Indeed, the main product on the intermediately binding catalysts (e.g., Pt, Rh and Pd) has changed from C_2H_2 in Figure 9 a) to C_2H_4 in Figure 9 b). Similarly, the main product on the most weakly binding metal (Ag) has shifted from C_2H_4 to C_2H_6. These changes in product selectivity are a consequence of the higher CH_2* and especially CH_3* coverages when CH_4 is vibrationally excited, compared to thermal catalysis (cf. Figure 9 d) vs. Figure 9 c)). This, in turn, results from the improved CH_4 dissociative adsorption on intermediately and weakly binding catalysts, in combination with their inability to further dehydrogenate these species. Hence, this study illustrates how plasma catalysis can be used to not only improve the overall reaction rate, but also to tune the product selectivity [74].

In conclusion, as illustrated here for CH_4 conversion, enhanced reactant activation by plasma does not shift the maximum in the volcano curve to more weakly binding catalysts, if the subsequent reaction steps do not happen more easily on these catalysts. In that case, plasma catalysis will mainly improve the rates for the intermediately binding catalysts near the optimum for thermal catalysis, unless additional surface reaction steps can be avoided. This might be possible due to the presence of various radicals produced by the rich plasma chemistry, as will be discussed further in section 4.8. Nevertheless, while facilitating the reactant activation step does not shift the optimal catalyst in terms of CH_4 consumption, it can still be used to tune the product selectivities on the different catalysts [74].

4.2.4 How the choice of catalyst affects beyond-equilibrium behavior: effect of reverse reactions

In section 4.1, we discussed that plasma-enhanced reactant activation can lead to product concentrations that exceed the thermal equilibrium, as a result of the improved forward reaction rates. However, as discussed in section 4.2.2, the product formation rates are affected differently by plasma-enhancement depending on the catalyst. Therefore, the same applies to the possibility of achieving product concentrations beyond the thermal equilibrium, as was demonstrated computationally for NH_3 synthesis by Mehta *et al* [61]. Since strongly binding catalysts do not benefit from enhanced reactant dissociation, neither can these achieve product concentrations that exceed the equilibrium composition. Weakly and intermediately binding catalysts, on the other hand, are affected by plasma-enhanced reactant activation and can thus reach product concentrations beyond the equilibrium limit. However, for exothermic reactions, like NH_3 synthesis, intermediately binding catalysts (that are optimal for thermal catalysis) revert the product concentrations to the equilibrium composition at lower temperatures. This is due to the higher catalytic activity of the intermediately binding catalysts in thermal catalysis, meaning that these catalyze both the forward and reverse reactions at a higher rate [61].

This highlights another aspect that should be paid attention to when selecting a catalyst material, namely that thermally active catalysts are also better at destroying the products. Of course, this is mainly relevant when operating in the equilibrium-limited regime, where the products are thermodynamically unfavored. However, some products are never present in significant amounts at thermal equilibrium, regardless of the temperature. This is, for example, the case for CH_3OH and other oxygenates at ambient pressure [10]. Consequently, the catalyst will stimulate the destruction of these molecules once the associated surface pathways become thermally active. As this is obviously undesired, (very) high temperatures should be avoided when aiming for these products.

Hence, when selecting an optimal catalyst for plasma catalysis, attention should be paid to the operating temperature, as catalysts that are more optimal for thermal catalysis will also catalyze the reverse reaction more efficiently. Consequently, these catalysts will revert the gas mixture to the equilibrium

composition at lower temperatures compared to more weakly binding catalysts that are less active in thermal catalysis.

4.3 The role of plasma species in plasma catalysis: vibrational excitation vs. radicals

As is shown in Figure 8, plasma can enhance reactant activation by weakening molecular bonds, thus lowering the barrier for dissociative adsorption. Alternatively, molecular bonds can be broken in the plasma, e.g., by electron impact dissociation, followed by adsorption of the formed radicals. As such, different mechanisms are possible in plasma catalysis, depending on which species are involved in the gas and surface reactions. In this framework, Rouwenhorst *et al.* [80] proposed four different mechanisms for plasma-catalytic NH_3 synthesis: (1) plasma-phase NH_3 synthesis, (2) surface-enhanced plasma-driven NH_3 synthesis, (3) plasma-enhanced semi-catalytic NH_3 synthesis, and (4) plasma-enhanced catalytic NH_3 synthesis. These mechanisms are schematically represented in Figure 10 a), b), c) and d), respectively. The first mechanism involves the breaking of chemical bonds in the plasma, with the subsequent reactions occurring entirely in the gas phase (Figure 10 a)). In the second mechanism, the bonds in both N_2 and H_2 are broken in the plasma, whereafter the formed radicals adsorb and react on the catalyst surface (Figure 10 b)). In the third mechanism, the N_2 bond is broken in the plasma, while H_2 dissociation and the subsequent reactions occur on the surface (Figure 10 c)). Lastly, in the fourth mechanism, all reactions occur on the catalyst surface, but N_2 is vibrationally excited prior to dissociating on the surface (Figure 10 d)) [80].

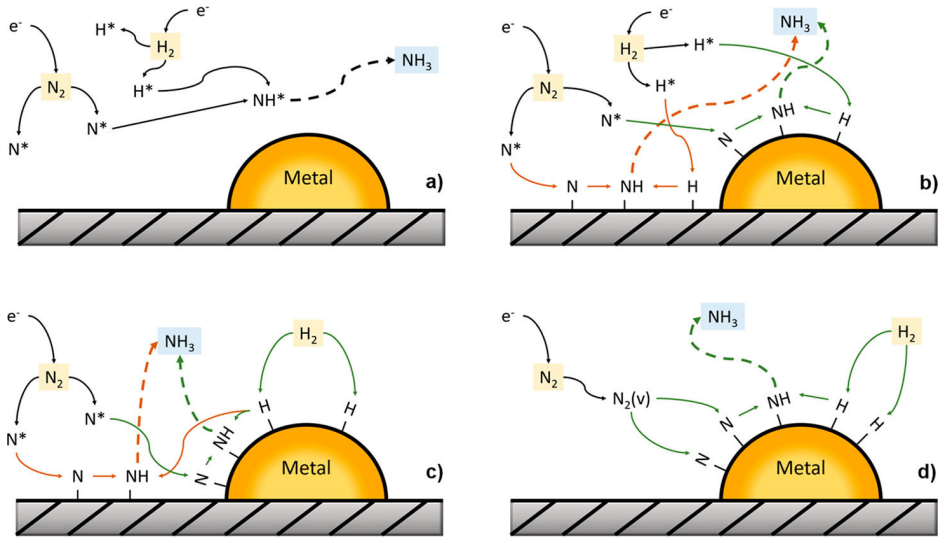

Figure 10. Schematic representation of different reaction mechanisms for plasma-catalytic NH_3 synthesis, namely: plasma-phase NH_3 synthesis (a), surface-enhanced plasma-driven NH_3 synthesis (b), plasma-enhanced semicatalytic NH_3 synthesis (c), and plasma-enhanced catalytic NH_3 synthesis (d). Reactions relevant for the mechanism are depicted with full arrows, while the subsequent reaction to NH_3 is depicted with a dashed arrow. Reproduced from ref. [80]. *CC BY NC ND 4.0*

In the same work, Rouwenhorst *et al*. compared Cs-, K- and Mg-promoted, as well as unpromoted Ru/γ-Al_2O_3 catalysts for plasma-catalytic NH_3 synthesis. The authors observed plasma-enhancement of the NH_3 synthesis rates and, interestingly, found that the catalysts showed the same trend in reactivity as for thermal catalysis. As alkali and alkaline-earth promotors are used in thermal catalysis to improve the dissociative adsorption of N_2, this observation pointed to N_2 dissociation occurring on the catalyst. Therefore, the authors attributed the plasma-enhancement to vibrational excitation, in accordance with the mechanism for plasma-enhanced catalytic NH_3 synthesis [80].

However, in a follow-up work [60] the same authors found that plasma-catalytic NH_3 synthesis instead occurred via a radical-based mechanism in at least part of the temperature range investigated. This is illustrated in Figure 11, which displays the NH_3 concentration over a temperature range of 50-500 °C for an empty DBD and a DBD packed with MgO, Ru/MgO and Ru-K/MgO. As can be seen in Figure 11, the curves of the Ru/MgO and Ru-K/MgO catalysts start to deviate from those of the empty and MgO-packed DBD around 125-175 °C, and synergy occurs at higher temperatures. Yet, in the temperature range between 200-300 °C, the unpromoted and K-promoted Ru/MgO catalysts show the same performance, thus indicating that N_2 dissociation does not happen on the catalyst. Hence, this points towards a radical-based mechanism. At temperatures above 300 °C, the activities of the catalysts start to deviate, indicating that enhancement by vibrational excitation also becomes important [60]. We can thus conclude that plasma-enhancement can happen both via radicals and vibrational excitation. Moreover, the dominant mechanism may vary depending on the temperature.

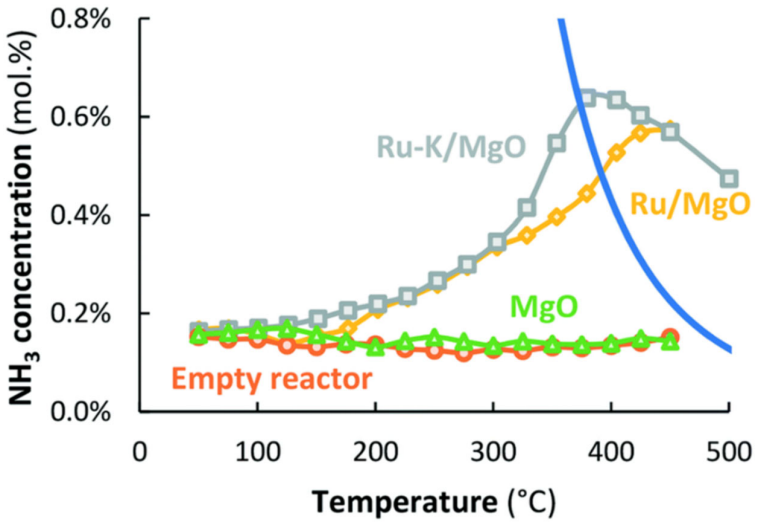

Figure 11. Activity for plasma-catalytic NH_3 synthesis at different temperatures for the empty reactor (orange circles) and the reactor packed with MgO (green triangles), Ru/MgO (yellow diamonds), and Ru–K/MgO (grey squares). Reaction conditions: total flow rate of 20 mL min^{-1}, 1:1 H_2/N_2 feed mixture, 130 mg catalyst loading and a plasma power of 3.8 W (SIE = 11.4 kJ L^{-1}). Reproduced from ref. [60] *with permission from the Royal Society of Chemistry. CC BY 3.0*

A temperature dependence of the mechanism for plasma-enhancement (i.e., radicals vs. vibrational excitation) is consistent with the idea that vibrational excitation only partly lowers the barrier for reactant dissociation. This is also depicted in in Figure 8 for CH_4, i.e., vibrational excitation only lowers the barrier for dissociative adsorption, so a certain temperature is still required to surpass the remaining part of the activation barrier. For plasma-enhancement by radicals, the dissociation occurs in the plasma and the radicals can adsorb onto the surface without having to surpass an enthalpy barrier. For the radical-based mechanism, the rate will thus depend on the radical density and on how facile the subsequent surface reactions can occur at the specified temperature. As such, we can interpret the results in Figure 11 as follows. Plasma-enhancement becomes effective around 125-175 °C, when the NH_x* hydrogenation and NH_3 desorption steps become thermally active. Up to 300 °C, plasma-enhancement is driven by radicals, which can adsorb and form surface-bound N* and H*, regardless of temperature. At temperatures above 300 °C, the dissociation of vibrationally excited N_2 becomes possible, further enhancing NH_3 formation.

This reasoning is also supported by kinetic modelling results from Ma *et al*. [72] for plasma-catalytic N_2 oxidation on Pt(211) and Au(211) surfaces. Their model showed that both Pt and Au benefit from the presence of radicals, while vibrational excitation only has an appreciable effect on Pt. Indeed, Pt, as an intermediately binding catalyst, has lower barriers for N_2 (and O_2) dissociation compared to the more weakly binding Au. The combination of the already lower barriers on Pt with vibrational excitation could result in significant rates on this catalyst, while the rate on Au remained low in the absence of radicals. Therefore, vibrational excitation and radicals gave comparable rates on Pt at high temperature (1000 K), while at low temperature (625 K) the radical-based mechanism resulted in the highest rates. On Au, on the other hand, the radical-based mechanism remained dominant both at low and high temperatures. In addition, the model showed that due to the stronger binding character of Pt, relative to Au, Pt also required higher temperatures for the desorption step to become thermally active. Consequently, Au outperformed Pt at low temperature (300 K) in the presence of radicals, while Pt performed better than Au at high temperature (900 K) in the presence of vibrationally excited molecules [72].

To summarize, plasma-enhancement by vibrational excitation is expected to be mainly relevant for intermediately binding catalysts at high temperature, while radicals are more important for intermediately binding catalysts at intermediate temperatures or for weakly binding catalysts in the entire temperature range. The observation that vibrational excitation has a negligible effect compared to plasma radicals at typical DBD temperatures (400 – 500 K) is also supported by other microkinetic modelling studies [74–76]. Of course, this will also depend on the vibrational temperature and the radical densities in the plasma.

4.4 Quantifying plasma-catalyst interactions

Due to the different possible mechanisms in plasma catalysis, as well as the complex plasma chemistry that occurs in tandem with the modified surface processes, a direct comparison of different catalysts is cumbersome. Kinetic studies that present methods for quantifying plasma-catalyst interactions can therefore aid in the comparison of catalyst materials and provide fundamental insight in the mechanisms of plasma catalysis. For example, Sheng *et al*. [81] determined activation barriers for DRM in thermal catalysis, as well as plasma catalysis operated at two different frequencies (12 and 100 kHz). These authors observed a strong decrease in the activation barrier for plasma catalysis at 100 kHz (44.7 kJ/mol) compared to thermal catalysis (91.2 kJ/mol) and plasma catalysis at 12 kHz (83.2 kJ/mol), which was attributed to accumulation of vibrationally excited species and their interaction with the catalyst [81]. Hence, apparent activation barriers might be used as a measure for the synergistic effect between plasma and catalyst. In this regard, modified Arrhenius equations have been developed that enable calculation of apparent activation barriers for plasma-catalytic reactions on specific catalysts [80,82,83]. In some studies [82,83] a modified Arrhenius behavior was reported in which the logarithm of the corrected reaction rate coefficient follows a linear correlation with the inverse of the specific energy input (SEI). A correction for the contribution of gas-phase reactions was applied by subtracting reactant consumption rates measured in a support-packed DBD from those of the plasma-catalytic case. Using this method, a strong reduction in apparent activation barriers was observed for plasma-catalytic DRM [82] and CO_2 hydrogenation [83], relative to thermal catalysis (i.e., from 73.5 kJ mol^{-1} to 6.1-18.6 kJ mol^{-1} and from 68-113 kJ mol^{-1} to 21-43 kJ mol^{-1} for DRM and CO_2 hydrogenation, respectively). In a different study [80], a modified Arrhenius equation was developed based on activity (i.e., amount of product formed per unit of time and amount of catalyst) divided by SEI. The logarithm of this quantity was observed to scale linearly with the inverse of temperature, and apparent activation barriers between 20-40 kJ mol^{-1} were determined for plasma-catalytic NH_3 synthesis on different catalysts (compared to 60-115 kJ mol^{-1} for thermal catalysis) [80]. The presence of the SEI in both abovementioned equations illustrates the dependency of plasma-catalyst synergy on plasma species (like vibrationally excited molecules and radicals), as low SEI's produce less plasma species and thus enhance the surface reactions less efficiently.

However, a higher SEI can also result in stronger plasma-induced heating [84], which could be responsible for the improved catalytic rates. While some plasma catalysis studies have reported that the effect of plasma-induced heating was not substantial enough to cause the observed synergy, this conclusion was often based on indirect measurements or estimations [59,80,85]. Nevertheless, recently, some experimental methods have been developed for direct, *in* situ measurement of the catalyst surface temperature. Moreover, these techniques do not require the insertion of, e.g., a thermocouple into the discharge region, and thus do not affect the plasma [11,86,87].

Gibson *et al.* [86] constructed an experimental setup for *in situ* X-ray absorption of plasma-catalytic CH_4 partial oxidation with Pd/Al_2O_3 and found that the temperature of the catalyst could be determined from the mean squared thermal disorder parameter, which corresponds to a change in the amplitude of oscillations of the extended X-ray adsorption fine structure of the catalyst. Parastaev *et al.* [87] developed a method for *in situ* measurement of the catalyst surface temperature based on thermally induced changes in absorption intensity of the 420 nm band of rutile TiO_2. Most recently, Van Turnhout *et al*. [11] developed a method to measure surface temperatures based on a downward shift of the band at 1965.9 cm^{-1} of $BaTiO_3$, which was added as an internal standard to the support. While in ref. [87] plasma-induced heating was reported to be negligible, refs. [86] and [11] reported surface temperatures up to 207 °C and 150 °C, respectively. Yet, these temperatures were still insufficient to thermally activate the catalysts. As such, these studies support the idea that plasma-enhancement of catalytic reactions is due to reactive plasma species, and not due to surface heating. Moreover, plasma-induced heating would not explain the beyond-equilibrium conversions observed for exothermic reactions, such as NH_3 synthesis, that are equilibrium-limited at higher temperatures [60].

Hence, both experimental kinetic studies, as well as direct measurements of the surface temperature in plasma catalysis experiments indicate that plasma-catalyst synergy occurs due to interactions of reactive plasma species with the catalysts surface. Moreover, kinetic studies provide methods to directly compare the performance of different catalysts, i.e., by determining apparent activation barriers from modified Arrhenius equations, while direct measurements of the catalyst temperature are necessary to correct for plasma-induced surface heating.

4.5 Tailoring the selectivities towards oxygenates: insights from CO_2 hydrogenation

A fundamental understanding of the mechanisms by which plasma catalysis alters the product selectivities for different catalysts is particularly important when aiming for products that are not thermodynamically favored, like CH_3OH and other oxygenates. Indeed CH_3OH is thermodynamically disfavored relative to CH_4/CO_2 at low temperatures, and relative to CO/H_2 at high temperatures [10]. As such, plasma catalysis should ideally facilitate steps in the catalytic pathway for CH_3OH formation without facilitating CO/H_2 production, and while also avoiding back-reaction to CH_4 and CO_2. This will be discussed in more detail in section 5 below. However, studies on plasma-catalytic CO_2 hydrogenation can also provide insights that may be applicable to DRM, while the reaction itself is somewhat simpler to study. Therefore, in the following subsections, we will first discuss observations from plasma-catalytic CO_2 hydrogenation on Cu and Ni, and link these to insights in catalyst selectivity from thermal-catalytic CO hydrogenation (section 4.5.1). Next, we will present the hydrogenation of plasma-produced CO as an important pathway for plasma-catalytic CO_2 hydrogenation (section 4.5.2), and finally we will briefly discuss other potential pathways for plasma-catalytic CO_2 hydrogenation (section 4.5.3).

4.5.1 The role of the catalyst in tuning the selectivity

In section 4.1 we discussed that the mechanism by which plasma catalysis improves the conversion depends on temperature. Similarly, any synergistic effects on the selectivities and yields may be influenced by the reaction temperature. This was, for example, observed in experiments on plasma-catalytic CO_2 hydrogenation by Eliason *et al.* [88]. Their results are shown in Figure 12, which illustrates a temperature dependence of the CH_3OH yields for thermal and in-plasma catalysis with a $CuO/ZnO/Al_2O_3$ catalyst, as well as the CH_3OH yield for an empty DBD. As can be seen in Figure 12, the maximum in the curve of the CH_3OH yield was shifted towards lower temperatures if the catalyst was combined with a DBD plasma. Consequently, plasma catalysis gave higher CH_3OH yields below approximately 170 °C, while thermal catalysis performed better at higher temperatures. DBD plasma without catalyst, on the other hand, gave a negligible CH_3OH yield over the entire temperature range (80-250 °C), showing that the catalyst was essential for CH_3OH formation. The drop in the plasma-catalytic CH_3OH yield towards higher temperatures could be attributed to competitive formation of CH_3OH and CH_4. Similar to the CH_3OH yield in Figure 12, the CH_3OH selectivity showed a maximum between 80-100 °C and subsequently declined at higher temperatures, which was accompanied by a rise in CH_4 selectivity. Hence, this indicates that DBD plasma can enhance both the formation of CH_3OH and CH_4 when combined with $CuO/ZnO/Al_2O_3$, albeit in different temperature ranges [88].

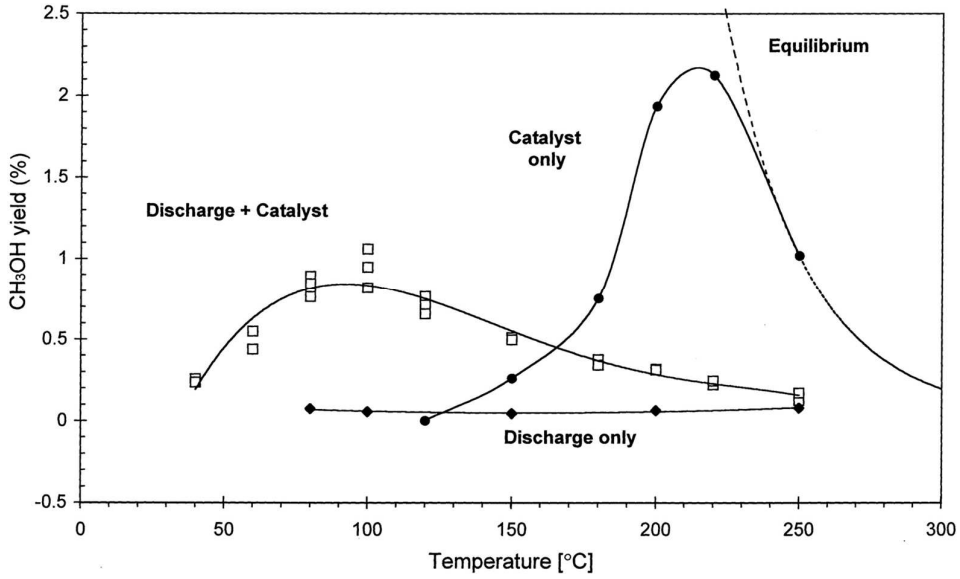

Figure 12. CH_3OH yield at different wall temperatures for plasma catalysis (Discharge + Catalyst), thermal catalysis (Catalyst only) and plasma without catalyst (Discharge only) at 8 bar and for a 3:1 H_2/CO_2 feed mixture. The dashed line indicates the equilibrium yield of CH_3OH if methanation is not allowed. Reprinted with permission from [88]. *Copyright (1998) American Chemical Society.*

The role of the catalyst in tuning product selectivity for plasma-catalytic CO_2 hydrogenation was also illustrated by Ahmad *et al.* [89]. Their results are displayed in Figure 13, which shows the CO_2 conversion and the selectivities of CH_4 and CO at different temperatures and reactor configurations. The DBD without catalyst (a) mainly produced CO, while the presence of a Ni/Al_2O_3 catalyst in a post-plasma (b), thermal (c) and in-plasma catalysis (d) setup at 150 °C gave high CH_4 selectivities for CO_2 hydrogenation (Figure 13). This clearly demonstrates that the Ni/Al_2O_3 catalyst was essential in achieving high CH_4 selectivity. Moreover, only the in-plasma catalysis setup (d) showed significantly enhanced CO_2 conversion, illustrating a synergistic effect between the plasma and catalyst. However, if the temperature was raised to 400 °C, the synergy disappeared and a similar conversion was attained for both thermal (e) and in-plasma (f) catalysis [89]

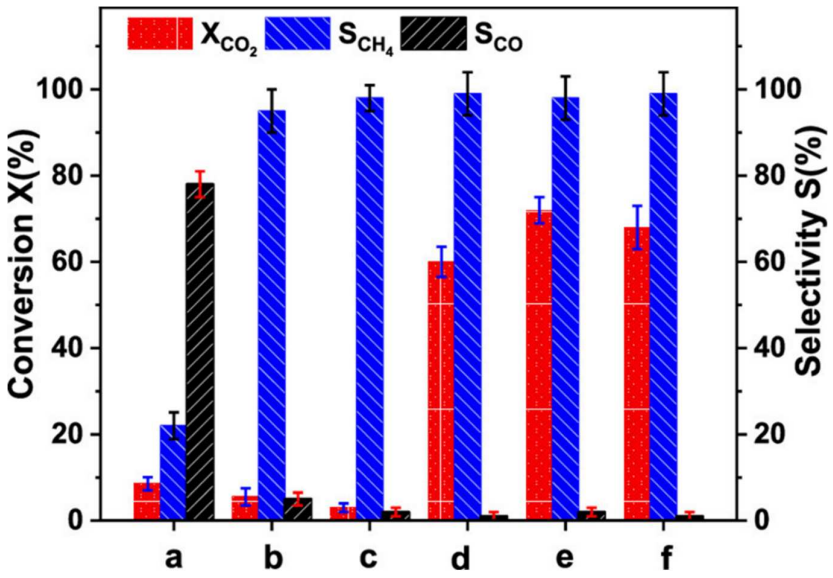

Figure 13. Conversion and product selectivity for CO_2 hydrogenation with different configurations of plasma-only, post-plasma, in-plasma and thermal catalysis, with 10% Ni/Al_2O_3, at different reaction temperatures: (a) plasma without catalyst at 150 °C, (b) post-plasma catalysis at 150 °C, (c) thermal catalysis at 150 °C, (d) in-plasma catalysis at 150 °C, (e) thermal catalysis at 400 °C, and (f) in-plasma catalysis at 400 °C. Reprinted with permission from [89]. *Copyright (2020) American Chemical Society.*

In the abovementioned works, the role of the catalyst in steering the selectivities towards CH_3OH or CH_4 seems to correspond well with observations from thermal-catalytic CO hydrogenation. Indeed, it is known that for thermal-catalytic CO hydrogenation weakly binding catalysts, like Cu, favor CH_3OH production, while more strongly binding catalysts, like Ni, Rh, Ru and Ir, are selective towards CH_4 [90–92]. This is because the weakly binding catalysts are unable to break the C-O bond and therefore cannot form CH_4, thus forming CH_3OH instead. The more strongly binding catalysts, on the other hand, can more easily break bonds and thus form CH_4 and H_2O [90–92].

In conclusion, the choice of catalyst can be used to steer the product selectivities of plasma-catalytic CO_2 hydrogenation, with a Cu-based catalyst enabling CH_3OH formation, while Ni preferentially forms CH_4. These observations correspond well with insights from thermal-catalytic CO hydrogenation, for which weakly binding catalysts (e.g., Cu) selectively produce CH_3OH, as these are unable to break the strong C-O bond, while strongly binding catalysts (e.g., Ni) can break the C-O bond and form CH_4. However, other factors, like temperature, also play a role in tuning the selectivities, as illustrated by ref [88].

4.5.2 Hydrogenation of plasma-produced CO as a mechanism for plasma-catalytic CO_2 hydrogenation

In both works on plasma-catalytic CO_2 hydrogenation discussed in section 4.5.1, CO is observed as the main C-based product for plasma-only conditions [88,89]. As such, it is likely that part of the CH_3OH and CH_4 produced by plasma catalysis can be attributed to CO_2 dissociation in the plasma, followed by CO hydrogenation reactions on the catalyst surface. This conclusion is also supported by experimental [83,87,93] and modelling studies [75].

For example, Parastaev *et al*. [93] used isotopic labelling in combination with temperature programmed reaction and found that pre-adsorbed $^{13}CO_2$ did not form $^{13}CH_4$ at temperatures below 100 °C, while formation of $^{12}CH_4$ from $^{12}CO_2$ in the gas phase did happen at lower temperatures. However, CH_4 formation only occurred when a $Co/CeZrO_4$ or $Cu/CeZrO_4$ catalyst was present in the DBD and not for the empty or $CeZrO_4$-packed reactor. Hence, this study shows that at temperatures below 100 °C, gas-phase CO_2 was converted into CO, which adsorbed and formed CH_4 on the catalyst. In a follow-up study [87], the same authors provided further support for this hypothesis, based on the presence of surface carbonyl (CO*) groups observed with *in situ* diffuse reflectance infrared Fourier transform spectroscopy (DRIFTS). In addition, Xu *et al*. [83] also found that CO was a key intermediate in plasma-catalytic CO_2 hydrogenation over Ru/MgAl-LDH catalysts, based on combined *in situ* DRIFTS and mass spectrometry (MS) analysis. These authors proposed a mechanism in which CO_2 dissociates partly in the gas phase and partly on the surface, followed by reaction of the formed CO on the surface to produce CH_4 via CHO*, COH* and CH_xO* intermediates. Furthermore, in a microkinetic modelling study by Michiels *et al*. [75], hydrogenation of plasma-produced CO on Cu(111) was found to be one of the pathways that lead to enhanced CH_3OH production for plasma catalysis, relative to thermal catalysis. Hence, these studies illustrate that CO, which can be formed from dissociation of CO_2 in the plasma, is an important intermediate in plasma-catalytic CO_2 hydrogenation to CH_3OH and CH_4.

The high selectivity towards CH_4 observed for strongly binding catalysts, like Ni [89], Co [87,93] and Ru [83], and the formation of CH_3OH on weakly binding catalysts, like Cu [88], is also consistent with the trends in selectivity for CO hydrogenation. However, in ref. [88] CH_4 became favored over CH_3OH

at higher temperatures, while in ref. [93] $Cu/CeZrO_4$ formed CH_4 and CO as the main products. Yet, CH_4 formation on $Cu/CeZrO_4$ happened with lower selectivity and required higher temperatures (> 350 °C) compared to the more strongly binding $Co/CeZrO_4$ catalyst, consistent with the trends in catalyst reactivity for CO_2 methanation [93]. Additionally, the plasma-catalytic CO hydrogenation to CH_4 on $Co/CeZrO_4$ observed in refs. [87,93] is also not possible at ambient temperature in thermal catalysis. Moreover, thermal-catalytic CO hydrogenation to CH_3OH also requires high temperatures and pressures to kinetically activate the reaction and drive the equilibrium composition towards CH_3OH, respectively [10,90]. Hence, this illustrates that plasma does not only facilitate CO_2 hydrogenation by dissociating CO_2 in the gas phase, but also enhances subsequent hydrogenation of the formed CO by adsorbed H* radicals on the catalyst surface. As such, plasma enables the formation of CH_4 on both weakly and strongly binding catalysts, as well as the formation of CH_3OH on weakly binding catalysts under conditions for which the catalysts are inactive for thermal-catalytic CO/CO_2 hydrogenation.

In the case of CH_4 formation, the plasma-enhancement may be attributed to vibrational excitation or electron impact dissociation of CO, which facilitates breaking of the C-O bond. Notably, in ref. [87] it is suggested that adsorbed CO* dissociates on the catalyst due to electrons impacting the surface. Additionally, the plasma might also enable any formed CH_3OH to undergo consecutive reactions, e.g., due to reaction with radicals or by electron impact processes, which may limit the CH_3OH yield and lead to CH_4 formation. We suggest that CH_3OH formation could be enhanced by the adsorption of plasma-produced H* radicals, as we will illustrate in section 4.6. Indeed, a challenge in thermal-catalytic CO hydrogenation exists in varying the energies of transition states for the CO* and CH_3O* hydrogenation steps independently from the binding energy of CO*, as this is prohibited by scaling relations [90]. However, it may instead be possible to improve these hydrogenation steps by increasing the H* coverage via adsorption of H radicals or by vibrationally exciting H_2.

To summarize, plasma can dissociate CO, which can subsequently be hydrogenated on the catalyst to either CH_3OH or CH_4. Moreover, this catalytic CO hydrogenation pathway is also facilitated by plasma-catalyst synergy. This allows us to understand how the choice of catalyst affects the selectivities in plasma-catalytic CO_2 hydrogenation. While weakly binding catalysts form CH_3OH in thermal catalysis, plasma catalysis can enhance both the surface hydrogenation steps, and to some extent the dissociation of the C-O bond, thus enabling both CH_3OH and CH_4 production on these catalysts at ambient conditions. The more strongly binding catalysts, on the other hand, remain selective to CH_4, while plasma-catalyst synergy only enhances the production rates.

4.5.3 Other pathways for plasma-catalytic CO_2 hydrogenation

Finally, other pathways for plasma-catalytic CO_2 hydrogenation have also been reported. For example, in ref. [83] the calcination temperature of the catalyst was found to affect the mechanism of plasma-

catalytic CO_2 hydrogenation. Next to the CO hydrogenation pathway, an additional surface pathway was reported for the catalyst calcined at high temperature (600 °C). In this pathway, CO_2 reacts with surface OH groups to form carbonate and bicarbonate species that subsequently react to HCOO* (formate), which forms CH_4 after multiple hydrogenation steps [83]. The modelling results presented in ref. [75] also showed additional pathways through which plasma-catalytic CH_3OH production could occur, next to CO hydrogenation. The HCOO* pathway, starting from CO_2 and adsorbed H*, was found to be the most important route for CH_3OH formation. This pathway was enhanced due to higher H* coverages, resulting from the presence of H radicals formed by the plasma. In addition, the model also predicted some surface HCOO* formation to occur through reaction between adsorbed O* radicals and CHO*. Note that CHO* is the first intermediate in the CO* hydrogenation route. Additionally, vibrational excitation of CO_2 was found to reinforce the impact of plasma-generated radicals, by lowering the activation barrier of the reaction between gas-phase CO_2 and surface H* to HCOO* [75]. The lower activation barriers for HCOO* production from vibrationally excited CO_2 were implemented based on the observations by Quan *et al* [94]. These authors found that vibrational excitation of the CO_2 bending mode facilitates the Eley-Rideal (E-R) type reaction between CO_2 and adsorbed H* to produce surface HCOO* on Cu(111) and Cu(100) surfaces. Their findings were based on both molecular beam experiments and density functional theory (DFT) calculations. Interestingly, these results illustrate that vibrational excitation can also enhance associative reactions to activate gas molecules on the surface and not only dissociative adsorption [94]. Furthermore, Kim *et al*. [95] demonstrated both experimentally and computationally that CO_2 hydrogenation on a Pd_2Ga/SiO_2 catalyst happens via reaction between vibrationally excited CO_2 and adsorbed H* to form HCOO*, which subsequently decomposes to CO*. In addition to the gas-phase dissociation of CO_2, followed by subsequent hydrogenation of adsorbed CO*, and conversion of CO_2 on the surface via the HCOO* route, the surface-catalyzed reverse water-gas shift (RWGS) reaction via a carboxyl intermediate (COOH*) has also been proposed as a possible pathway in plasma-catalytic CO_2 hydrogenation [96].

Hence, next to hydrogenation of plasma-produced CO (discussed in section 4.5.2) there exist several other pathways through which plasma-catalytic CO_2 hydrogenation can occur, such as the RWGS reaction and variations on the CHOO* route. These pathways may benefit from enhanced H* coverages due to adsorption of plasma-produced radicals. In addition, vibrationally excited CO_2 can also improve the E-R reaction between gas-phase CO_2 and adsorbed H*.

4.6 The role of CO hydrogenation in plasma-catalytic DRM: insights from modelling

In section 4.5 we suggested that plasma can facilitate CH_3OH formation by dissociating CO_2 in the gas phase, followed by plasma-catalytic CO hydrogenation on the surface of weakly-binding metals. Since CO and H_2 are typically the main products of DRM, also in DBD plasmas [12–17,48,50], this pathway could potentially play a role in CH_3OH production via plasma-catalytic DRM. Therefore, we here

provide insights from our own modelling results to illustrate potential pathways and trends between catalysts for CH_3OH production via plasma-catalytic DRM. We performed simulations using the descriptor-based microkinetic model CatMAP [97]. The CatMAP code calculates steady-state fractional coverages and reaction rates on a catalyst surface exposed to a fixed gas mixture. As such, we would like to emphasize that this model exclusively provides information on the catalyst surface chemistry, but does not consider any gas-phase reactions or changes to the gas composition that may occur due to surface reactions. However, we recently have developed a coupled plasma-surface model that does consider these effects, and the results will be presented in section 5 below. Nevertheless, the present catalyst surface model is also of interest, as it enables visualization of trends in reactivity between different catalysts, based on scaling relations that describe the activation barriers of the reactions on different transition metals. These scaling relations are derived from DFT energies that were taken from the work of Schumann *et al*. [91] on CO hydrogenation. To include additional reactions for DRM, we extended this set with our own DFT results, using settings that match those of Schumann *et al*. as much as possible for consistency reasons. More information on the methodology of the DFT calculation can be found in the supporting information (SI), section S1. In the surface kinetics simulations with CatMAP, we employed a two-site model in which H* adsorbs on a separate reservoir site, in accordance with ref [91]. This is based on the assumption that H* shows negligible interaction with other adsorbates, due to its small size. As such, H* can still co-adsorb if the surface is covered by other adsorbates. Inclusion of lateral adsorbate-adsorbate interactions is outside the scope of this study, and thus not considered here. However, such interaction might destabilize adsorbates that have high fractional coverages, thus improving their reactivity and desorption. Nevertheless, while this might potentially expand the maximum in the volcano plot towards more strongly binding catalysts, the overall trends are expected to remain the same. A detailed description of the methodology for the CatMAP simulations can be found in section S2 of the SI.

We focus on the reaction pathways and kinetics that occur due to the presence of plasma-produced syngas (CO/H_2) and small partial pressures of radicals (CH_3, H and O) in the CH_4/CO_2 gas mixture. Specifically, CH_3, H and O radicals were considered as they can be directly formed from the reactants, i.e., CH_4 and CO_2, by electron impact dissociation. Unless noted otherwise, we used a 1:1 CO_2/CH_4 gas mixture, which also contains 1.4×10^{17} cm^{-3} (0.01 bar) CO and H_2, as well as 1.4×10^{11} cm^{-3} (10^{-8} bar) CH_3, H and O radicals. For CO and H_2, we chose a number density of 1.4×10^{17} cm^{-3} as a representative value at low conversion, because the possibility of attaining high conversions will be more strongly dependent on the reaction conditions and catalyst. In addition, we chose a value of 1.4×10^{11} cm^{-3} as a typical radical density in a DBD plasma, based on ref. [98] in which radical densities between 10^{10}-10^{14} cm^{-3} were reported for CH_3, H and O. The simulations were performed for a total pressure of 1 bar and a temperature of 500 K, as these conditions are representative for a DBD plasma, commonly used for plasma catalysis.

4.6.1 Effect of plasma species on the catalytic formation of CH_3OH

To illustrate how the plasma-catalytic formation of CH_3OH is affected by different plasma species, i.e. radicals, as well as H_2 and CO formed in the plasma, we calculated the CH_3OH formation rates for different gas mixtures. By removing certain species from the gas mixture, we can observe their effect on the CH_3OH production pathways. We would like to emphasize that for pure CH_4/CO_2 gas mixtures, no reaction occurs at 500 K as the process is strongly equilibrium-limited by the high thermodynamic stability of CH_4 and CO_2 at this temperature [10]. This case is therefore not considered. Our results are displayed in Figure 14, which shows the CH_3OH production rates as function of the O* and CH* binding energies for four different gas mixtures. The binding energies of O* and CH* are correlated to the energies of all others surface species (including transition states) via scaling relations, and thus serve as descriptors that determine the activation barriers and rate coefficients. These binding energies are defined as the formation energies of the adsorbed species relative to the empty slab and CO, H_2O and H_2 in the gas phase. As such, lower (i.e., negative, more exothermic) binding energies correspond to more stable, and thus more strongly bound adsorbates, while higher (or positive) binding energies correspond to more weakly bound adsorbates.

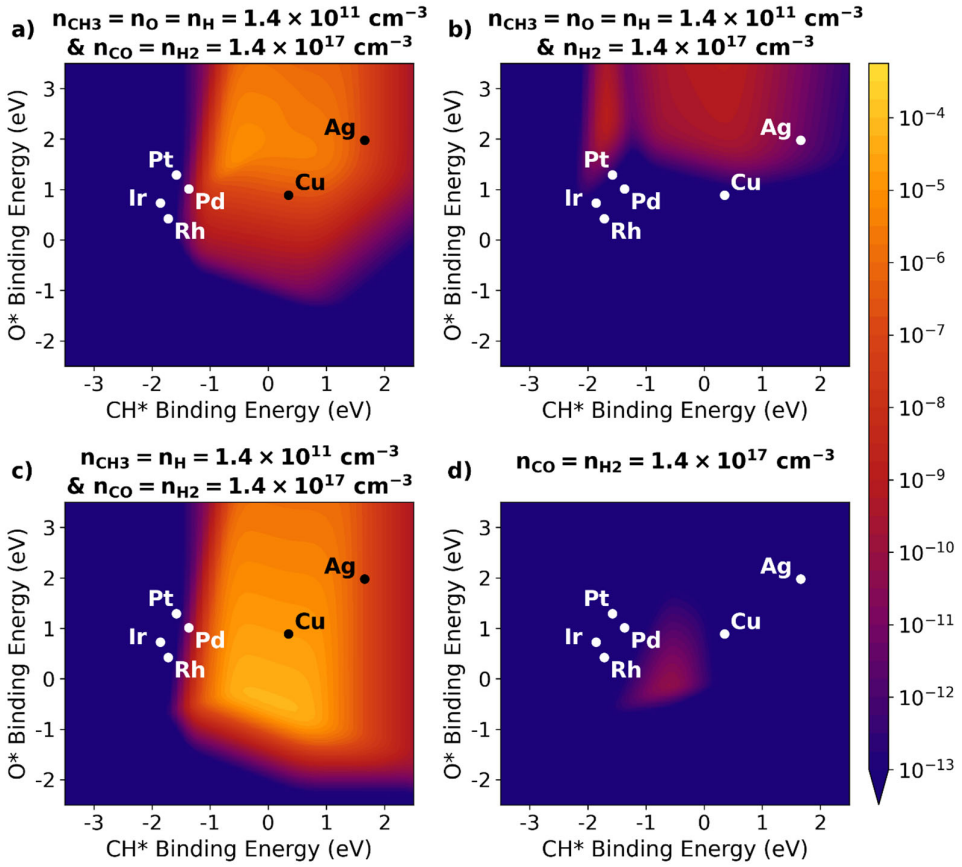

Figure 14. Activity plots of the CH_3OH production rates in s^{-1} on transition metal (111) surfaces exposed to a 1:1 CH_4/CO_2 gas mixture, that also contains (a) 1.4×10^{11} cm^{-3} (10^{-8} bar) of CH_3, H and O radicals and 1.4×10^{17} cm^{-3} (10^{-2} bar) of H_2 and CO, (b) 1.4×10^{11} cm^{-3} (10^{-8} bar) of CH_3, H and O radicals and 1.4×10^{17} cm^{-3} (10^{-2} bar) of H_2, but no CO, (c) 1.4×10^{11} cm^{-3} (10^{-8} bar) of CH_3 and H radicals and 1.4×10^{17} cm^{-3} (10^{-2} bar) of H_2 and CO, but no O, or (d) 1.4×10^{17} cm^{-3} (10^{-2} bar) of H_2 and CO, but no radicals. The total pressure is 1 bar and the temperature 500 K for all cases. The binding energies of O and CH* are the formation energies of the adsorbed species relative to the empty slab and CO, H_2O and H_2 in the gas phase. Low (negative) values of these binding energies represent strongly binding catalysts, while high (positive) values correspond to weakly binding catalysts.*

Figure 14 a) displays the CH_3OH production rates for a gas mixture that contains plasma-produced CH_3, H and O radicals, as well as syngas (CO and H_2), next to the feed gas (CH_4 and CO_2). For this gas mixture, CH_3OH is formed through hydrogenation of CO by H radicals, which are both directly adsorbed from the plasma. The CO* hydrogenation pathway goes through CHO*, CH_2O* and CH_3O* via subsequent hydrogenation steps to eventually form CH_3OH. The best performing catalysts for this gas mixture are Cu and Ag, which can be attributed to the facile bond formation steps on these weakly binding catalysts. In addition, the rates remain negligible at strong CH* and O* binding, due to surface poisoning by CO* (which binds through carbon and thus scales with CH*) or O*, respectively.

When CO is removed from the gas mixture, the CH_3OH formation rate is much lower (see Figure 14 b)). Indeed, CH_3OH formation cannot proceed through CO hydrogenation anymore, but instead happens from adsorbed CH_3*, H* and O* radicals. In the broad region at weak CH* binding, this occurs via the CH_3O* intermediate through: O* + H* → OH*, CH_3* + OH* → CH_3O* + H* and CH_3O* + H* → CH_3OH. In the second, narrower region at stronger CH* binding, adsorbed CH_3* is first partly dehydrogenated to CH*, followed by coupling with OH* to form CHOH*. This species is then subsequently hydrogenated to form CH_3OH. The best catalysts for CH_3OH production via these pathways are Ag and Pt, respectively. However, comparison between Figure 14 a) and b) clearly shows that formation of CH_3OH directly from adsorbed CH_3*, O* and H* radicals is much more difficult than CO* hydrogenation by adsorbed H* radicals on the catalyst surface.

When O radicals are removed from the gas mixture (without removing CO), the CH_3OH formation rate drastically increases, and Cu becomes the best catalyst, followed by Ag (see Figure 14 c)). Indeed, O* poisoning becomes (quasi) negligible in this case, as direct adsorption of O radicals is no longer possible. As such, a high density of O radicals in the plasma is not beneficial for the surface reactions as this limits the rates on the catalyst due to poisoning. Note that also removing CH_3 radicals from the gas mixture of Figure 14 c) results in essentially the same CH_3OH production rates, as CH_3* does not participate in the CO* hydrogenation pathway.

Finally, as illustrated in Figure 14 d), removing all radicals from the gas mixture results in a strong reduction of the CH_3OH production rates overall. In this case, CH_3OH is formed from the small fraction of syngas that is present, through thermal catalytic CO hydrogenation. Comparing Figure 14 c) and d) illustrates how the presence of H radicals strongly increases the rate of CH_3OH production on the metals that bind CH* weakly. This is because these catalysts have more difficulty with breaking the H-H bond in H_2. However, if H radicals are present in the gas phase, this H-H bond has already been broken by the plasma. In this way, H_2 dissociation on the catalyst surface can be circumvented. Consequently, this improves the H* coverages on the weakly binding catalysts, which in turn enhances the CO* hydrogenation steps.

In conclusion, these results again demonstrate how plasma can overcome the scaling relations for bond dissociation that are normally present in thermal catalysis, by breaking or weakening bonds in the reactant molecules, as was also discussed in section 4.2.2. However, as we will illustrate in the next section, CH_3OH formation from plasma-produced radicals and syngas (CO/H_2) is negligible compared to the production rates of other molecules (CH_4, CO_2, H_2O and H_2), at least for gas mixtures that are representative for CH_4/CO_2 plasmas.

4.6.2 Surface reactions that compete with CO hydrogenation in plasma-catalytic DRM

In section 4.6.1, we illustrated that plasma-produced CO and H radicals can enhance the formation of CH_3OH on the surface of weakly binding metals, like Cu and Ag. However, we find that CH_4, CO_2, H_2O and H_2 have significantly higher production rates, at least for a gas mixture representative of CH_4/CO_2 plasma, that contains CH_3, H and O radicals, as well as syngas (CO and H_2), next to the feed gas (CH_4 and CO_2). Figure 15 illustrates the production rates of CH_4, CO_2, H_2O and H_2 for such a gas mixture, i.e., the same gas mixture used for Figure 14 a). As can be observed by comparing Figure 14 a) and Figure 15, the CH_3OH production rates are indeed negligible compared to the high production rates of CH_4, CO_2, H_2O and H_2. A high production rate for CH_4 or CO_2 in this context means that the catalysts can efficiently recombine H and CH_3 radicals, formed in the plasma, back to CH_4, or CO and O back to CO_2. This is of course an unwanted effect and indicates that the catalyst will lower the effective plasma conversion and thus acts as an inhibitor for the overall reaction. Note that CO is oxidized to CO_2, and thus destroyed, on all catalysts for the conditions in Figure 15. Since the CO destruction rate matches the CO_2 production rate, it is not included in Figure 15.

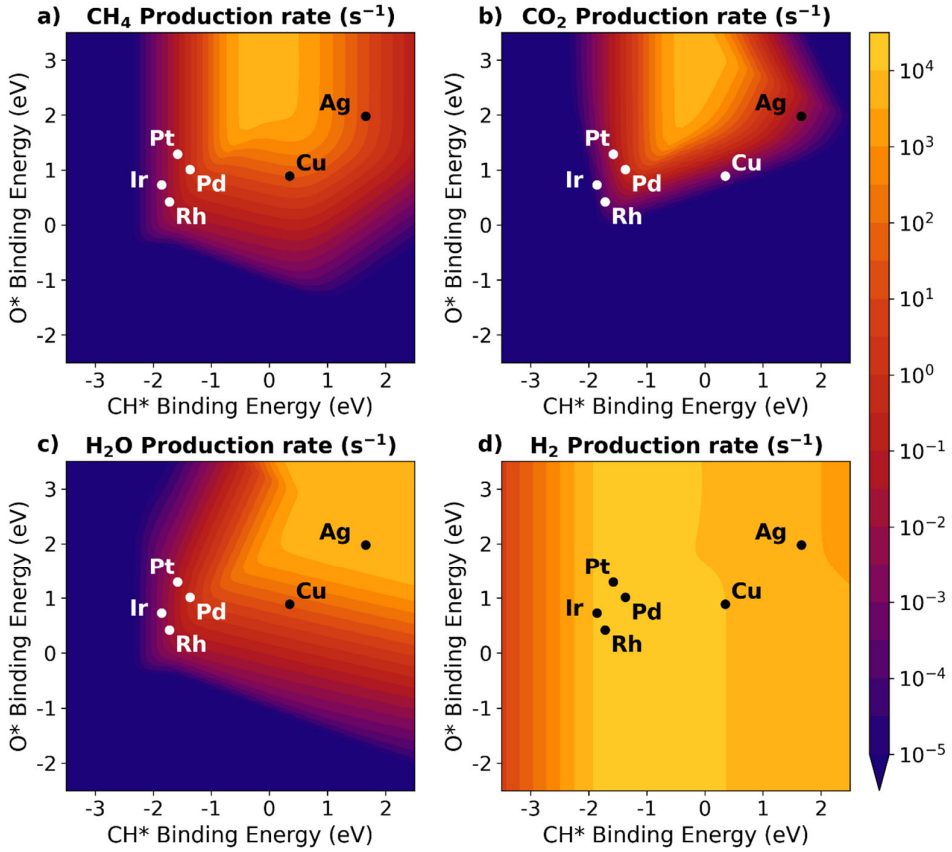

Figure 15. Activity plots of the production rates in s^{-1} for (a) CH_4, (b) CO_2, (c) H_2O and (d) H_2 on (111) transition metal surfaces exposed to a gas mixture containing 7.1×10^{18} cm^{-3} (0.49 bar) CO_2 and CH_4,

1.4×10^{17} cm^{-3} (0.01 bar) H_2 and CO, and 1.4×10^{11} cm^{-3} (10^{-8} bar) CH_3, H and O radicals at a temperature of 500 K. We do not plot the CO production rate, as CO is oxidized into CO_2, and thus destroyed at the catalyst surface; the CO destruction rate matches the CO_2 production rate. The binding energies of O and CH* are the formation energies of the adsorbed species relative to the empty slab and CO, H_2O and H_2 in the gas phase. Low (negative) values of these binding energies represent strongly binding catalysts, while high (positive) values correspond to weakly binding catalysts.*

Figure 15 a) displays the rate for CH_4 production due to recombination of CH_3 and H radicals on the catalyst. This occurs most easily on catalysts that bind CH* relatively weakly or intermediately and O* weakly. i.e., specifically Cu, followed by Ag and to a lesser extent Pd. At strong CH* or O* binding the rates are limited due to surface poisoning, as is also the case for CH_3OH production (discussed in section 4.6.1.). This is also observed in the production rates of CO_2 and H_2O (Figure 15 b) and c), respectively). The maximum of the CH_4 production rate at intermediate CH* binding strength results from lower barriers for recombination on more weakly binding metals, while some CH* binding is required to a have sufficiently high CH_3* coverage. Indeed, CH_3* binds the surface relatively weakly for a radical (e.g., $\Delta H_{CH3(g)\rightarrow CH3*}$ = -0.99 eV on Ag(111) in this chemistry set [79,91]).

The rate for CO_2 production via oxidation of plasma-produced CO by adsorbed O* radicals is shown in Figure 15 b). The rate exhibits a similar trend as that for CH_4 formation, but it declines more rapidly upon going to weaker CH* or stronger O* binding. This similar trend is because sufficiently strong CH* binding is required to have a high enough coverage of CO* (which binds to the surface via the carbon atom), while bond formation is easier on the more weakly binding metals. The highest CO_2 formation rate is observed for Pd, which is in line with thermal catalytic CO oxidation, for which Pd is widely known to be a good catalyst, as it is used for this purpose in automobile exhaust catalysts [99,100].

H_2O is formed by recombination of H* and O* radicals on the surface, with OH* as intermediate adsorbate. As presented in Figure 15 c), the H_2O formation rate is the highest on Ag and (to a lesser extent) on Cu. Since both the O and H radicals bind to the surface strongly, sufficient coverages can be attained on even the most weakly binding metals. Consequently, the highest rates are observed for the most weakly binding catalysts. It is important to realize that H_2O formation competes with CO_2 formation for O*, while it competes with CH_4 and H_2 formation for H*. Similarly, CH_3OH also competes with the formation of CH_4, H_2O and H_2 for H*, and with the formation of CO_2 for CO*. Yet, CH_3OH formation is disadvantaged compared to these other reactions on all catalysts. Consequently, the adsorption of CH_3 and O on the surface is undesirable as these species can scavenge surface H* and CO* to form thermodynamically (very) stable CH_4, H_2O and CO_2 molecules. Moreover, these recombination reactions occur much more easily than CO* hydrogenation to CH_3OH.

Lastly, H_2 is formed upon recombination of two H* radicals, and this reaction occurs with the highest rate on most catalysts (except Ag), as illustrated in Figure 15 d). The slight decrease of the H_2 production rate in the region around Ag, is due to competition for H* with H_2O production. Note that the uniformly high H_2 production rates are partly attributed to the assumption that H can still co-adsorb onto sites that are already occupied by another species. As a result, H radicals in the model can still adsorb and recombine to H_2, even if the surface is poisoned by another, larger species. For more information see section S2 of the SI. Note that the recombination of H radicals to H_2 on the surface will always compete for H* with CO* hydrogenation to CH_3OH. This will inevitably result in a loss of energy efficiency as a large fraction of the energy used to form H radicals in the plasma will not be directed into the formation of CH_3OH.

To summarize, while plasma-produced CO and H can enhance the formation of CH_3OH on the catalyst surface, the CH_3OH formation rate is negligible compared to the production rates of CH_4, CO_2, H_2O and H_2. Indeed, these molecules can easily be formed through recombination reactions of adsorbed radicals and CO on the catalyst. Moreover, these processes direct CO* and H*, needed for CH_3OH production, into other molecules, meaning that these plasma species will not be used efficiently. To avoid the competing formation of CH_4, H_2O and CO_2, adsorption of CH_3 and O radicals should be limited. This may be achieved by reducing their formation in the plasma. However, these radicals may be important for the gas-phase production of CH_3OH [98]. Nevertheless, if chemical effects play a dominant role in plasma catalysis, it would be more beneficial to maximize the reaction rates on the catalyst surface at the cost of those in the bulk plasma. Of course, this would only be applicable to conditions where the chemical effects positively affect the formation of the desired products.

Finally, we would briefly like to mention that although we did not consider the RWGS and HCOO* (formate) pathways in the simulation, our general conclusion would remain largely the same. Indeed, these pathways could possibly result in more facile CO* and CH_3OH formation. However, both the RWGS and HCOO* pathways depend on the presence of H* radicals on the surface. Consequently, the presence of CH_3* and O* on the surface are still undesired, as these react easily with H* to form CH_4 and H_2O, respectively. Moreover, O radicals would still oxidize surface-bound CO*, back to CO_2 and inhibit the overall DRM reaction.

4.7 A proposed solution for CH_3OH production in DRM

As illustrated in sections 4.5 and 4.6.1, plasma-produced H radicals and CO are likely to play an important role in plasma-catalytic CH_3OH formation for CO_2 hydrogenation and DRM. Based on the trends in catalyst selectivity for CO/CO_2 hydrogenation, weakly binding catalysts (like Cu) are expected to be more suitable for CH_3OH production. As discussed in section 4.5, this can be attributed to the lower activity of these weakly binding catalysts for C-O bond scission, which would result in CH_4

instead of CH_3OH [90–92]. Indeed, Cu-based catalysts have been observed to form CH_3OH in plasma-catalytic CO_2 hydrogenation experiments [88,96]. Moreover, the hydrogenation of CO* to CH_3OH also benefits most from plasma-produced H radicals on the weakly binding Cu and Ag surfaces, as illustrated in our modelling results (section 4.6.1). However, this does require that high densities of CO and H radicals can be obtained in the gas phase. On the other hand, the additional presence of CH_3 and O radicals negatively affects surface pathways for plasma-catalytic CH_3OH formation, as these radicals easily recombine with H* and CO* to produce CH_4, H_2O and CO_2, as illustrated by our modelling results in section 4.6.2. Yet, since CH_3 and O can be formed directly from the dissociation of CH_4 and CO_2, these radicals are important plasma species in DRM.

Relatively strongly binding catalysts (e.g., Ni, Ru, Co) can hydrogenate CO_2/CO to CH_4 (as discussed in section 4.5) and should thus be avoided at the relatively low temperatures where CH_4 is thermodynamically favored. Indeed, plasma enables CH_4 formation on these catalysts even at low temperature, as was experimentally observed for plasma-catalytic CO_2 hydrogenation with catalysts based on Ni [89], Ru [83] and Co [87,93]. On the other hand, strongly binding metals (e.g., Ni) are still expected to be good catalysts for DRM to syngas at high temperatures, as these can also more easily break the C-H bonds in CH_4 (as illustrated in Figure 8). Indeed, plasma-catalyst synergy for DRM to syngas (CO/H_2) has experimentally been observed on Ni catalysts at high temperatures [59]. Moreover, the combination of a relatively strongly binding catalyst, like Ni, with high temperatures would also enable plasma catalysis via vibrational excitation, rather than radicals (see section 4.3), which is more energy efficient. Addition of specific promotors may further improve the reaction, as was illustrated by Sheng *et al*. [101], who reported that adding a La-promotor to a Ni/Al_2O_3 catalyst enhanced the production of syngas in plasma-catalytic DRM. The La-promotor was found to enable the formation of surface carbonates from vibrationally excited CO_2, which facilitated the oxidation of CH_x* on the Ni catalyst.

Hence, we could propose a plausible solution based on a two-stage plasma reactor setup, in which a first reactor operates at high temperature, combined with a strongly binding catalyst (e.g., Ni) to enrich the gas mixture with syngas, and reduce the amount of CH_4 and CO_2. A second reactor can then be placed in series that operates at low temperature, with a more weakly binding catalyst (e.g., Cu) to form CH_3OH.

4.8 Complex mixtures of radicals

As already discussed in section 4.3, plasma can enhance catalytic reactions by lowering the barrier for reactant activation on the surface (e.g., due to vibrational excitation) or by dissociating the molecules in the plasma to form radicals. However, radicals produced via electron impact dissociation will also participate in further gas-phase reactions, resulting in a wide distribution of radicals and stable

intermediates that is characteristic of a plasma. In principle, all these species can adsorb and participate in the catalyst surface chemistry. This might allow to bypass several difficult surface reactions or enable new surface pathways that are not active in thermal catalysis. The optimal catalyst then becomes dependent on the plasma composition.

Using microkinetic modelling, Engelmann *et al.* [74] demonstrated that for catalysts exposed to radical densities representative of a CH_4 DBD plasma, the highest production rates can be achieved on the most weakly binding metals (such as, Ag, Au and Cu). This is illustrated in Figure 16, which shows the TOFs for different products on transition metal catalysts exposed to radical densities that are characteristic of a CH_4 DBD plasma. By comparing Figure 16 to Figure 9 (a, b) from the same study, showing the TOFs for a) thermal catalysis and b) plasma catalysis with only vibrationally excited CH_4, we can observe the impact of the radicals. As can be seen in Figure 16, the volcano maximum shifts entirely to the catalysts with the weakest binding strengths (like Ag), as the TOFs (especially for C_2H_4 production) strongly improve on these catalysts. This is because the rates on the surface are no longer limited by bond-scission. Indeed, the radicals and intermediates in the gas-phase (e.g., H_2, CH_x (x = 0-4) and C_2H_x (x = 1-6)) can simply adsorb onto the surface and undergo C-C coupling or hydrogenation to form stable products. As such, a lower binding strength results in higher rates, as it allows for facile recombination of the adsorbed radicals, as well as easy desorption of the products [74]. However, we would like to emphasize that the most weakly binding catalysts will only give the highest rates for radicals on the surface, and not necessarily a good selectivity for the desired products. The selectivities on these weakly binding catalysts will be strongly determined by the composition of the plasma, as well as the activation barriers for the different recombination processes relative to each other. For some reactions, further bond-scission in the radicals might be needed to attain the desired products. For example, CO formation from CH_4 in DRM and SRM requires that all four C-H bonds in CH_4 are broken. For such cases, a more strongly binding catalyst might be more desirable. Yet, this would also require higher operating temperatures to thermally activate the remaining bond scission steps on the surface, as well as product desorption from the catalyst.

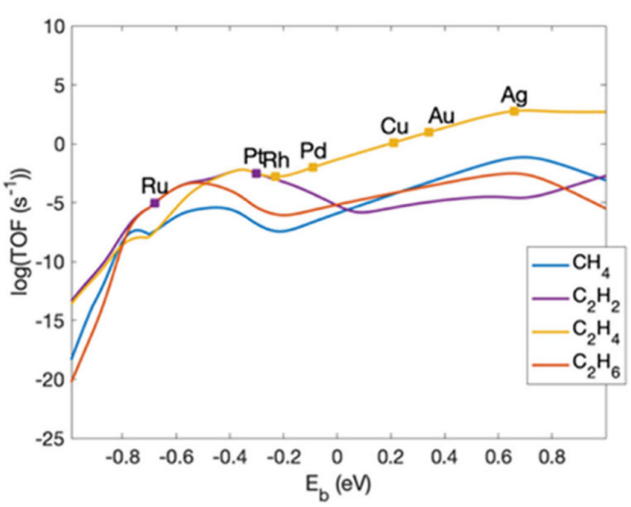

Figure 16. Steady-state TOFs of CH_4 non-oxidative coupling with reactive plasma species, characteristic for a CH_4 DBD plasma at 500 K. The values are plotted against the binding energy (E_b) of CH_3. Low (negative) values of E_b correspond to strongly binding catalysts, high (positive) values of E_b correspond to weakly binding catalysts. When comparing this figure to Figure 9(a, b), where the same results were shown, but for thermal catalysis and the effect of vibrational excitation, respectively, it is clear that reactive plasma species enhance the TOF, especially of C_2H_4 formation, on the weakly binding catalysts. Reprinted with permission from* [74]. *Copyright (2020) American Chemical Society.*

Nevertheless, as mentioned above, the plasma composition will strongly affect the dominant reaction pathways on the surface. Moreover, these surface reactions can in turn produce new molecules and therefore alter the gas composition as well. Thus, to obtain more insight in the combined plasma-catalyst chemistry, models must be developed that couple the reactions on the catalyst surface to those in the plasma, as is discussed in more detail in section 5. Such a coupled model was developed by Maitre *et al.* [102] for plasma-catalytic CH_4 non-oxidative coupling over a Ni(111) surface. Interestingly, these authors found that plasma catalysis could briefly achieve improved turnover frequencies compared to plasma alone and thermal catalysis. Yet, this synergy was only temporal, and at steady-state plasma without catalyst outperformed plasma catalysis at all temperatures investigated (300-600 K). The model showed that H radicals produced in the plasma absorbed and saturated the surface, enabling quick hydrogenation of surface-bound CH_3* back to CH_4 [102].

Similarly, adsorption and recombination of CH_3 and H radicals back to CH_4 was also observed in the aforementioned study by Engelmann *et al.* [74]. Like the other radical recombination reactions on the catalyst surface, back-reaction to CH_4 occurs more easily on the most weakly-binding metals. This can also be understood from Figure 8, which shows that the barrier for recombination of CH_3* and H* to CH_4 is lower on Cu(211) than on Ni(211). The observations from abovementioned studies on non-oxidative coupling of CH_4 align well with the insights provided by our modelling results for DRM

presented in section 4.6.2. Indeed, our modelling results also show that CH_4 is produced at high rates, especially on weakly binding catalysts (Cu and Ag), due to adsorption and recombination of CH_3 and H radicals. The implications of these results are important, as this means that a large fraction of plasma-produced CH_3 and H radicals that diffuse to the surface may not contribute to product formation, but instead recombine again into the reactants. In section 5, we provide further support for this conclusion based on results from our own, newly developed coupled plasma-surface model for DRM.

Lastly, by means of a microkinetic surface model, it is possible to individually vary the radical partial pressures. Although these will not yield self-consistent simulations, as they are not based on a coupled plasma-surface model, this approach can provide useful insight in the role of specific plasma species on the reaction pathways. Loenders *et al*. [76] applied this method to study the partial oxidation of CH_4 on Pt(111). Their results showed that highly dehydrogenated carbonaceous species (C, CH and C_2H_2) bind strongly to the surface, causing catalyst poisoning and coking. On the other hand, high partial pressures of O radicals can counteract coking, yet also cause overoxidation to CO_2. As such, these authors recommended that a balanced CH_4/O_2 ratio and plasma power should be identified, to tailor the amount of hydrogen-poor carbonaceous species vs. O radicals [76]. These observations are also relevant for DRM, where coking is typically an important issue. Moreover, attaining a good balance between carbon formation and overoxidation is especially difficult at the low temperatures relevant for DBD, for which solid carbon and CO_2 are highly thermodynamically stable [66]. In addition, Loenders *et al*. also demonstrated the importance of H radicals for the formation of oxygenates (HCOOH and CH_3OH) on the catalyst surface [76]. Moreover, they identified the CH_3O and CH_3OO radicals present in CH_4/O_2 DBD plasmas as crucial species for plasma-catalytic CH_3OH and CH_2O production on the Pt(111) surface. This illustrates that the formation of oxygenates through surface pathways in plasma catalysis might require the formation of more complex radicals via gas-phase reactions in the plasma prior to adsorption. Finally, this study illustrated that higher radical partial pressures near the surface are not necessarily more beneficial as these could poison the catalyst [76].

In summary, plasmas are complex mixtures of different reactive species and thus typically contain a wide variety of radicals. Consequently, adsorption and subsequent reaction of these radicals on the catalyst allows to circumvent additional surface reactions next to the initial reactant activation step. As such, the surface reactions strongly depend on the densities of the radicals in the plasma. This is especially true for the most weakly binding catalysts (e.g., Cu, Ag, Au) which can recombine the radicals very efficiently. However, this does not mean that these weakly binding catalysts are necessarily the most optimal catalysts, as they can also induce back-reactions due to fast recombination of radicals to the reactants. As such, a thorough understanding of the effect of different radicals on the surface pathways is crucial, so that the gas mixture and plasma conditions can be chosen to maximize the formation of desired products and avoid unwanted back-reactions and coking.

4.9 Eley-Rideal (E-R) reactions involving radicals

In addition to adsorption of radicals from the plasma and subsequent surface reaction via a Langmuir-Hinshelwood (L-H) type mechanism, the highly reactive radicals may directly react with pre-adsorbed surface species via E-R type reactions. Engelmann *et al*. [71] used a microkinetic model for NH_3 synthesis to illustrate the potential effect of E-R reactions involving radicals. Their model showed that if plasma radicals can directly react with surface adsorbates with no enthalpic activation barrier, the volcano behavior of the catalyst activities disappears entirely. While weakly binding catalysts (e.g., Cu, Au and Ag) can quickly adsorb radicals and let them recombine via L-H reactions, coupling between surface adsorbates this way is difficult on strongly binding catalysts (such as Fe and Ru). This leads to high surface coverages on the more strongly binding metals, poisoning the surface. However, facile E-R reactions with radicals would allow for high reaction rates, even on catalysts that are strongly covered by adsorbates. This was found to result in similar reaction rates on weakly and strongly binding metals exposed to radicals [71]. This prediction was supported by the experimental work of Gorbanev *et al*. [103], who observed that different Al_2O_3-supported transition metal catalysts gave a similar performance in plasma-catalytic NH_3 synthesis, and also demonstrated by other experiments [39,70,104,105], showing the same behavior. Similarly, modelling work by Hong *et al.* [106] and van 't Veer *et al.* [107] also indicated that E-R reactions may play an important role in plasma-catalytic NH_3 synthesis.

We expect that E-R reactions may also have a significant impact on the plasma-catalytic conversion of CH_4 and CO_2. Indeed, E-R reactions between H (or D) atoms and various C- or O-containing adsorbates (e.g., CO*, CHO*, HCOO*, O*, OD*, CD_3* and cyclo-hexane) have been observed experimentally by impinging H or D radicals on pre-covered transition metal surfaces, although at temperatures and pressures well below ambient conditions [108–110]. However, there is still much uncertainty around the kinetics and products of most E-R reactions involving polyatomic radicals or adsorbates, especially at conditions relevant for plasma catalysis. Some studies have proposed that CH_3OH formation in plasma catalysis may be partly attributed to E-R reactions, like $CH_3(g) + O^* \rightarrow CH_3O^*$, and $CH_3O^* + H(g) \rightarrow CH_3OH(g)$ [76,111,112]. Still, it is important to consider that other products could result from the same reactant species and may even be more important. For example, radicals impinging on large poly-atomic adsorbates might be more tended to react with the top part of the adsorbate, if the surface-bound atom is difficult to reach due to steric effects. Indeed, it has been experimentally shown that impinging D atoms can abstract H atoms from cyclohexane adsorbed on Cu(111) [108].

To conclude, E-R reactions between gas-phase radicals and adsorbates are likely important in plasma catalysis, and they can explain the similar reactivity for vastly different catalysts, as observed experimentally [39,70,103–105]. Yet, currently not much is known about these reactions. Therefore, more fundamental research on the kinetics and product distribution of E-R reactions involving radicals is required in order to more reliably implement these into microkinetic models.

4.10 Radicals reaching the catalyst surface

Whether or not radicals and other plasma species can actually partake in the catalyst surface chemistry of course depends on the flux of these species to the surface. On one hand, this depends on the distance between the plasma and the catalyst, which for a packed-bed DBD will depend on the discharge type, i.e., localized microdischarges between the packing beads or surface discharges spread over the surface of the beads. In addition, the local electric field and electron density will determine the occurrence of electron impact processes, and consequently also the densities of different plasma species. As discussed in section 3.6, the discharge behavior can be strongly influenced by, among others, the properties (e.g., dielectric constant [31,32,40–42,48,58], pore diameter [49], bead size [40,42]) of the packing material, the size of the discharge gap [41,42,58], the presence of metal nanoparticles [31,36–38] and the amount of metal loading [37,38]. On the other hand, the lifetime of the plasma species will determine whether they can survive long enough to travel from the bulk plasma to the surface, or inside the pores of the support where catalyst nanoparticles may be deposited, as discussed in section 3.4.

This aspect was considered by Jiang *et al*. [85], who studied CH_4 partial oxidation to oxygenates using an experimental setup with a Fe/γ-Al_2O_3 catalyst placed downstream of a plasma jet at either 5 or 30 mm distance. This allowed to distinguish the effect of short-lived species, like radicals, and long-lived plasma-produced species, respectively. Only at the shortest distance, enhanced CH_3OH and CO_2 production was observed. The authors postulated that even for a plasma that is in direct contact with the catalyst, plasma-species should have a sufficiently long lifetime to traverse the plasma sheath and diffuse from the bulk of the plasma to the catalyst surface. Based on measurements with molecular beam mass spectroscopy and estimates of the lifetimes of different radical species, the authors subsequently proposed that CH_3OO was responsible for the synergistic effect of plasma catalysis on CH_3OH production [85].

Moreover, the situation is even more complex for a DBD plasma due to the periodic occurrence of short-lived microdischarges. As such, the operating conditions of the DBD should be tuned to optimize to production and number densities of specific species in the gas-phase. This was illustrated by Sheng *et al.* [81], who found that applying a high-frequency (100 kHz) DBD plasma leads to a strong plasma-catalyst interaction for high-temperature (400-700 °C) plasma-catalytic DRM over a La-modified Ni/Al_2O_3 catalyst. On the other hand, only a weak plasma-catalyst interaction was observed when a low frequency (12 kHz) was used. The effect was attributed to accumulation of vibrationally excited CH_4 due to the more frequent pulses for the 100 kHz DBD. Hence, this study demonstrates the importance of tuning the operating conditions of the power source to improve the formation of specific plasma species [81].

However, in general more research is needed to identify which plasma species can effectively reach the surface for different reactions and conditions. Indeed, further development of plasma catalysis not only requires a good understanding of the chemical plasma-catalyst interactions, i.e., how the plasma species can alter the surface kinetics and pathways. Thorough knowledge of the physical effects, as discussed in section 3, is also needed, as these will govern the contact between the plasma and the catalyst and thus determine which chemical interactions may occur.

5 Insight from coupled plasma-surface simulations: effect of catalyst on DRM

As illustrated in section 2, plasma-catalytic DRM does not always yield improved performance compared to plasma-only. Therefore, in this section, we provide insights in the effect of transition metal catalysts on plasma-catalytic DRM, using our newly developed coupled plasma-surface microkinetic model. We will illustrate how the presence of a catalyst can also negatively affect the conversion and selectivities of plasma-catalytic DRM, by selectively recombining CH_3 and H radicals to CH_4, and O radicals and CO back to CO_2. Indeed, it is also experimentally revealed that the presence of transition metal catalysts not always enhances the conversion, but can also have a negative impact (e.g., [11–15]). However, direct comparison with experiments is often not possible due to the complex interplay of various physical and chemical interactions, as discussed in sections 3 and 4, respectively. Nonetheless, modelling allows to study these interactions separately, and can thus aid in disentangle these effects. In this way, we can point out potential drawbacks that exist in plasma catalysis, but that are often not considered or are unknown.

In the following sections, we will first briefly cover other kinetic models that combine the plasma and catalyst surface reactions, and the approximations made therein, to provide further context to our model. Subsequently, we will discuss the results and insights provided by our model. More specifically, we will illustrate how the presence of a transition metal catalyst in the plasma affects the destruction of CH_4 and CO_2, as well as the production of CO, H_2, H_2O and CH_3OH. Note that the conclusions presented in this section are applicable to DRM at typical DBD conditions but can differ for other plasma-catalytic reactions which might still benefit from the presence of a catalyst.

5.1 Coupled plasma-surface kinetics models in literature

When a plasma is in contact with a catalyst, not only will reactive plasma species adsorb and partake in the surface chemistry, but the catalyst will also form new molecules that desorb into the gas-phase and thus affect the plasma. Coupled plasma-surface models that describe both the reaction kinetics in the plasma and on the catalyst simultaneously are thus crucial in improving our understanding of the chemical interactions that play a role in plasma-catalysis.

Yet only very few studies have attempted to combine the reaction kinetics of discharge plasmas and catalyst surfaces in a single microkinetic model. Hong *et al*. [106] developed a kinetic model that contained both plasma and surface reactions for NH_3 synthesis. While the focus of the model was on the complex and elaborate plasma chemistry, it also contained several surface reactions, including both L-H and E-R reactions. Yet, the rate coefficients for surface reactions were largely based on the kinetics for diffusion of gas species to the surface and surface diffusion of adsorbates. This approach, however,

required the estimation of various parameters (e.g., sticking coefficients and activation barriers) [106]. Based on the same surface chemistry, van 't Veer *et al*. [107,113] developed a coupled plasma-catalyst model for NH_3 synthesis, to study the effect of filamentary microdischarges and their afterglows that are typical for a DBD plasma. For this purpose, the gas was periodically (i.e., as function of time) exposed to pulses in power density. By correlating this time-dependency to the residence time in the reactor, the gas was treated as a volume-element that traverses a (tubular) reactor [107,113]. Du *et al*. [112] combined a plasma kinetics model for CO_2 hydrogenation with surface pathways for CH_3OH formation on Cu(111), and CH_4 formation on Ni(111). These authors also studied the effect of microdischarges, in this case by applying a pulsed reduced electric field (E/N). The surface kinetics were described using the same theory as in the works by Hong *et al*. and van 't Veer *et al.* The authors compared two possible pathways for CH_3OH formation on the Cu(111) surface, while only a limited number of surface intermediates were considered for CH_4 production on Ni(111) [112].

Ma *et al*. [72,73] developed a continuously stirred tank reactor (CSTR) model for plasma-catalytic N_2 oxidation and studied the role of vibrational excitation and radicals on both the plasma and the catalyst. The surface reactions were described using rate coefficients calculated with transition state theory and activation energies calculated with DFT. The electron impact dissociation of N_2 and O_2 was not included in the model, but the dissociation degrees of N_2 and O_2 were treated as variables instead [72,73]. The model showed good agreement with experimental results in which a Pt catalyst was placed in the afterglow of a radio-frequency powered N_2/O_2 plasma [73]. The same reaction setup for plasma-catalytic N_2 oxidation was also studied by Eshtehardi *et al*. [114], who constructed a one-dimensional model with axial dispersion, which could attain even better agreement with the experimental results. In addition, these authors studied the effect of the gas composition entering the catalyst-bed, as well as various operating parameters, to illustrate opportunities for improving the process performance [114].

Pourali *et al*. [115] constructed a CSTR model to study plasma-catalytic non-oxidative coupling of CH_4 over a Cu(211) catalyst. A constant plasma power was deposited into the reactor volume, rather than a pulsed power profile. Similarly, Maitre *et al*. [102] developed a coupled plasma-surface model for CH_4 non-oxidative coupling, but in combination with a Ni(111) surface. These authors also used a CSTR approach in combination with constant power density input. Their model included an elaborate set of surface process, including both E-R and L-H reactions, and incorporated the effect of both vibrationally excited species and plasma radicals [102].

To conclude, while some studies are available, coupled plasma-surface models for plasma catalysis applications are generally still in a pioneering phase, and further development of such models is both promising and highly needed.

5.2 Main equations governing the coupled plasma-surface model

In this section we provide a summary of the main equations governing the coupled plasma-surface model, a detailed discussion of the methodology of the model can be found in sections S3 of the SI. The model uses a CSTR approach, meaning that perfect mixing is assumed and thus that the species densities and coverages are considered uniform throughout the reactor volume. The change in number densities of gas-phase species with time are calculated using the following balance equation:

$$\frac{\partial n_s}{\partial t} = R_{reaction,s} + \frac{n_{s,in} v_{in}}{V_{CSTR}} + \frac{n_{s,out} v_{out}}{V_{CSTR}} \quad (1)$$

In which n_s is the number density of species s and t is the operating time. The first term on the right-hand side, $R_{reaction,s}$, represents the change in number density due to reactions. The second and third terms correspond to the change in number density due to reactants entering and products leaving the reactor, respectively. Here $n_{s,in}$ and $n_{s,out}$ are the species densities in the feed and in the outlet, respectively. Note that for a CSTR model, $n_{s,out}$ matches the species density in the reactor n_s. V_{CSTR} is the volume of the reactor occupied by gas, while v_{in} and v_{out} are the volumetric flow rate entering and leaving the reactor, respectively.

The change in number density of gas-phase species due to reactions is calculated as:

$$R_{reaction,s} = \sum_{i,gas} \left[(c_{s,i}^R - c_{s,i}^L) r_i\right] + n_{sites} f_{cat} \sum_{i,cat} \left[(c_{s,i}^R - c_{s,i}^L) r_i\right] + n_{sites}(1 - f_{cat}) \sum_{i,wall} \left[(c_{s,i}^R - c_{s,i}^L) r_i\right] \quad (2)$$

The first term on the right-hand side corresponds to the reactions occurring in the gas-phase, the second due to reactions on the catalyst surface and the third term due to reactions happening on a "non-catalytic" surface, such as the reactor walls or a support packing. In eq. (2), $c^R_{s,i}$ and $c^L_{s,i}$ are the stoichiometry coefficients of species s in reaction i on the right-hand (production) and left-hand (destruction) side of the reaction equation, respectively. The reaction rates r_i are expressed in $cm^{-3}\ s^{-1}$ for gas-phase reactions or s^{-1} for surface reactions. The terms corresponding to surface reactions are therefore multiplied by the total volumetric density of surface sites n_{sites}, which is expressed in cm^{-3}, and by a factor denoting the fraction of these sites that is catalytic f_{cat} or non-catalytic $(1 - f_{cat})$.

The volumetric flow rate of the gas leaving the reactor v_{out} used in eq. (1), is calculated in such a way that the total pressure in the reactor remains constant. This is done according to the following equation:

$$v_{out} = v_{in} + \frac{V_{CSTR} \sum_{s,gas} R_{reaction,s}}{\sum_{s,gas} n_s} = v_{in} + \frac{V_{CSTR} k_b T}{p_{tot}} \sum_{s,gas} R_{reaction,s} \quad (3)$$

In which p_{tot} is the total pressure in the reactor, k_b is the Boltzmann constant and T is the temperature. Hence, the volumetric flow leaving the reactor equals the volumetric flow entering the reactor plus the change in volume resulting from the reactions. The values of the parameters used in eqs. (1), (2) and (3) are discussed in the SI, section S3.1.

Similar to eq. (1) for the densities of gas-phase species, the change in surface coverages with time for catalytic and non-catalytic surface sites are described using balance equations:

$$\frac{\partial \theta_{s,cat}}{\partial t} = \sum_{i,cat} \left[(c_{s,i}^R - c_{s,i}^L) r_i \right] \quad (4)$$

$$\frac{\partial \theta_{s,wall}}{\partial t} = \sum_{i,wall} \left[(c_{s,i}^R - c_{s,i}^L) r_i \right] \quad (5)$$

However, in these equations there is only one term, which corresponds to the change in coverage due to reactions, as no sites can enter or leave the reactor.

The reactions rates r_i are expressed as:

$$r_i = k_i \prod_s \prod (a_s)^{c_{s,i}^L} \quad (6)$$

In which k_i is the reaction rate coefficient of reaction i and a_s is the activity of species s, which are expressed as either number densities, partial pressures, or fractional coverages, depending on the species and the reaction. For more information see section S3.2 of the SI.

The reaction rate coefficients for gas-phase reactions, electron impact dissociation reactions, catalytic surface reactions and reactions occurring on the non-catalytic wall are discussed in sections S3.3, S3.4, S3.5 and S3.6 of the SI, respectively. Additionally, the reactions included in the model are listed in the SI, i.e., in Table S5 for gas-phase reactions, Table S7 for electron impact reactions, Table S8 for catalytic surface reactions (including adsorption and desorption) and Table S9 for non-catalytic surface reactions (also including adsorption and desorption).

5.3 Assumptions made in our coupled plasma-surface model

In our own model, we also apply the CSTR approach, similar to refs. [72,73,102,115], meaning that the densities of the gas species and the surface coverages are considered to be uniformly distributed over the reactor volume. However, rather than applying a constant power density as was done in refs.

[102,115], we calculate the rate coefficients for electron impact dissociation at the breakdown electric field and multiply these by the fraction of the reactor volume that is occupied by microdischarges~~, as described in section S3 of the SI~~. This way, we attain a volume-averaged rate coefficient for radical production that is representative for a DBD plasma. These rate coefficients are calculated using an electric field of 229 Td and an electron density of 10^{14} cm^{-3} in the plasma. A plasma power of 65 W is chosen which is assumed to be completely deposited into the microdischarges. A detailed description of the calculation of the electron impact rate coefficients can be found in section S3.4 of the SI. If the applied plasma power would be evenly distributed over volume and over time (as was done in refs. [102,115]), the maximum power density would be much lower compared to when the plasma power is concentrated in the microdischarges. Consequently, much less electrons would reach the energy threshold for electron impact dissociation, and the associated rates would be clearly underestimated. On the other hand, we also chose to not treat the microdischarges explicitly, i.e., as variations in power density as function of time. Indeed, such approach would mean that the entire reactor volume experiences the power density that would normally occur in the spatially limited microdischarges, which would lead to an unrealistically high radical production. Note that this is the direct consequence of the spatial uniformity of the reactions rates, gas species densities and surface coverages that is inherent to zero-dimensional models. A possible alternative would be the approach presented in refs. [107,113], in which a volume-element is simulated that travels along a reactor (i.e. similar to a plug-flow reactor approach), rather than the entire reactor volume. However, in that approach the model becomes dependent on the time that the gas needs to reach a certain position in the reactor, meaning that surface coverages would only evolve as function of this definition of time. Yet, in reality the catalyst typically remains stationary in the reactor and the surface coverages on a specific position in the reactor evolve as function of (operating) time. Thus, the latter approach is unphysical with respect to the evolution of the surface coverages. Hence, we choose to use a CSTR approach, combined with spatially averaged rate coefficients for electron impact dissociation, representative for a DBD plasma, as we believe this is the most realistic approach for a zero-dimensional model.

We can further motivate this approach as follows. In a CSTR model, perfect mixing is assumed, meaning that there are no gradients in e.g., species densities and coverages, throughout the entire reactor. This is obviously an extreme case, as perfect mixing is typically not achieved, and it also implies that the catalyst surface is in perfect contact with the plasma. The latter is of course an approximation, as in reality the plasma species will need to diffuse from the bulk plasma to the catalyst surface. As these species diffuse to the surface, they will react, leading to a drop in their densities, while new radicals and stable molecules are formed. While the gas-phase reactions present in our model will partly compensate for this effect, i.e., as unstable species will have higher loss rates and thus lower densities, the effect of the catalyst surface will still be overestimated to some extent. However, this is inherent to the spatial uniformity that is assumed in all zero-dimensional models (i.e., even plug-flow models assume spatial

uniformity in the radial direction). As such, this is also the case for almost all models [72,73,102,106,107,112,113,115] discussed in section 5.1, with exception of ref. [114], which describes a model for post-plasma catalysis. To circumvent this issue, higher dimensional models are required. Yet, these models are significantly more computationally demanding, resulting in limitations on the size of the chemistry set that can be used.

Furthermore, as we discussed in section 4.3, experimental results show that radicals play an important role in enhancing the surface pathways, and are even the dominant species for plasma-catalyst synergy at the lower temperatures (i.e., around 500 K) that are relevant for DBD plasmas [60]. This demonstrates that a significant number of radicals can indeed reach the surface and will be affected by the catalyst, further justifying our CSTR approach, in which the catalyst surface is in perfect contact with the plasma. However, this might not necessarily be observed in all experiments, as it will also depend on various physical effects. Indeed, changes in the discharge type can alter the contact between the plasma and the catalyst and thus affect the number of radicals that reach the surface. Furthermore, in some conditions, vibrationally excited molecules might play a role in plasma-catalyst synergy, as discussed in section 4, but they are not included in this model here, as we consider them indeed to be of minor importance at typical DBD conditions (see above). Anyway, the experimental results in ref. [60] provide evidence that radical adsorption on the catalyst surface can indeed happen at significant rates, and are not simply a consequence of approximations made in the model. This indicates that our model is indeed relevant for experimental plasma catalysis applications.

Finally, with respect to the surface reactions, we use rate coefficients based on transition state theory combined with activation barriers calculated by DFT, as these are more accurate than rate coefficients calculated from estimated sticking coefficients or reaction barriers. We therefore use the same set of surface reactions as for the CatMAP simulations, discussed in section 4.6. In addition to the reactions on the surface of the transition metal catalysts, we also consider surface reactions on an inert surface, representative for the reactor wall and the packing beads. As a reliable set of DFT data is unavailable for these surface reactions, they are treated more approximately, using rate coefficients based on the kinetics of gas species colliding with the surface and diffusion of adsorbates on the surface [116–118]. More information on the calculation of the rate constants can be found in section S3 of the SI.

5.4 Coupled surface and plasma kinetics simulations: Results for DRM

Here we present the results of our coupled plasma-surface kinetics model, to explain why the presence of a transition metal catalyst in plasma-catalytic DRM can also negatively affect the chemistry. The model uses a CSTR approach, as explain in previous section, with a 1:1 CH_4/CO_2 feed mixture entering the reactor. During the simulations, the temperature and pressure are kept constant at 500 K and 1 bar, respectively, as these are typical conditions for a DBD plasma. While DRM is not possible in thermal

catalysis at these conditions, as the reaction is kinetically and equilibrium-limited, the formation of reactive plasma species (e.g., radicals) enables this reaction in plasma catalysis. Indeed, these highly reactive plasma species react further in the gas-phase, but can also adsorb and react on the catalyst surface thus bypassing the difficult reactant activation steps present in thermal catalysis. For a detailed description of the model, we refer to section S3 in the SI.

The surface species energies in the coupled model are described using the same scaling relations as those used in the simulations with CatMAP (see section S2 of the SI). This allows us to model transition metal catalysts for which only limited reaction data is available, or even hypothetical catalysts. However, for the purpose of this study, we limit ourselves to Ag(111), Cu(111) and Rh(111) surfaces. We perform simulations for four different cases: i.e., plasma without catalyst, as well as combined with one of the abovementioned catalysts. The corresponding values of CH* and O* binding energies, used in the scaling relations, are (E_{CH*} = 1.66 eV, E_{O*} = 1.98 eV) for Ag, (E_{CH*} = 0.35 eV, E_{O*} = 0.89 eV) for Cu, and (E_{CH*} = -1.72 eV, E_{O*} = 0.42 eV) for Rh, as acquired from ref. [91] and our own DFT results (see Table S1 in the SI). As such, we compare a set of metals for which both CH* and O* become more strongly bound when going from Ag to Cu to Rh.

In the SI (section S4, Figure S1), we present the time-evolution of the H, CH_3, O and OH radical densities in the plasma. Initially, the radical densities increase with time, both with and without catalysts, due to electron impact dissociation in the plasma. As radical adsorption becomes significant, the radical densities for the different transition metals and the plasma-only case start to deviate, as the net adsorption rates vary with the catalyst material. This eventually causes the radical densities to stabilize at different values for different transition metals. A more detailed analysis is given in the SI, section S4. This demonstrates how the catalysts affect the plasma (radical) composition. In the following subsections, we will describe how the catalysts affect the destruction of the reactants (CO_2 and CH_4) and the formation of various stable molecules (CO, H_2, H_2O and CH_3OH), as obtained by our coupled plasma-surface kinetics model, at steady state. We will compare the net production or destruction rates for the plasma without catalyst, as well as combined with the three different metals. To highlight the effect of the catalyst, distinction will be made between the total net rate, the net rate on the catalyst surface and the net rate in the plasma. Note that while C_2H_6 is included in the gas-phase as a species representative for higher hydrocarbons, C_2H_6 formation on the catalyst surface is not included in our model as these reactions are not included in the reaction set by Schumann *et al*. [91]. However, taking the corresponding values from other studies would lead to an inconsistent reaction set. Therefore, an analysis of the effect of the catalyst on C_2H_6 production is outside the scope of this work. However, it is worth mentioning that C_2H_6 is still the second most important carbon-containing product in the gas-phase (the main carbon-containing product is CO).

5.4.1 CO_2 destruction at steady state

Figure 17 shows the net rate of CO_2 destruction for the different cases at steady state. Note that hatched bars indicate net production on the catalyst surface, instead of destruction. As can be seen in Figure 17, CO_2 is indeed net produced on all catalyst surfaces due to net recombination of CO* and O* on the catalyst. This is in line with our results of section 4.6.2, where we also discussed the production of CO_2 on the catalyst surface (see Figure 15). While CO_2 production on Rh happens at a rate that is many orders of magnitude lower than the other rates in Figure 17, CO_2 production is non-negligible on Cu, and even significant on Ag surfaces. The low rate on Rh results from CO* poisoning of this catalyst at 500 K.

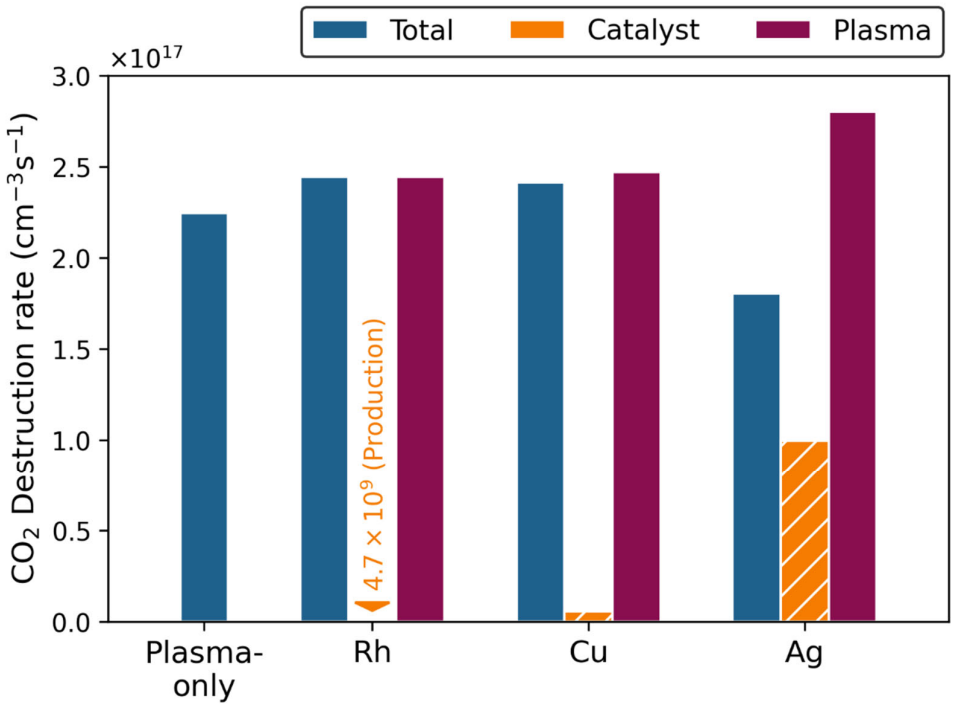

Figure 17. Net rates of CO_2 destruction at steady state ($t = 10^6$ s) for plasma without catalyst, or combined with a Rh, Cu or Ag catalyst. Distinction is made between the total rate, the rate on the catalyst surface and the rate in the plasma. Hatched bars indicate net production instead of destruction. The net (production) rate on the Rh surface is indicated by its numerical value, as it is many orders of magnitude lower compared to the other rates in the figure. Calculated for a 1:1 CH_4/CO_2 feed mixture using a total pressure of 1 bar and a temperature of 500 K.

The rate of recombination to CO_2 is indeed most notable for the Ag surface, as it is large enough to cause a clear drop in the total net destruction rate of CO_2. As such, less CO_2 is destroyed in total for the case with Ag compared to plasma without catalyst, or combined with Rh or Cu. As mentioned in previous paragraph, this is due to the quick recombination of adsorbed CO* and O*, and it is also partly

responsible for the lower O (and OH) densities in the plasma, which can be observed in Figure S1 c) and d). While Ag is indeed among the better catalysts for CO_2 formation in Figure 15 b), it is not the catalyst with the highest rate in this figure. However, in the coupled plasma-surface simulations, the CO and O densities in the gas phase are higher (9.7×10^{17} cm^{-3} and 2.6×10^{11} cm^{-3}, respectively, for plasma with Ag) compared to those used in the simulations with the CatMAP code (see section 4.6.2). This can increase the CO_2 formation rates on weaker binding catalysts, relative to the more strongly binding catalysts, as the latter are more susceptible to poisoning.

The total (and plasma) CO_2 destruction rates are slightly higher for the cases with Cu and Rh relative to the plasma without catalyst. This is due to a higher rate of $CO_2 + CH_2 \rightarrow CO + CH_2O$ in the plasma, which is caused by a higher CH_2 density in the plasma. As can be seen in Figure S1 a), the H density in the plasma is strongly reduced when a transition metal is present, which results in less CH_2 recombining with H, and thus in higher CH_2 densities. This is also the case for Ag, and for this catalyst the net CO_2 destruction rate in the plasma is even higher, due to a reduction in the rate of CO_2 formation via $CO + OH \rightarrow CO_2 + H$. The latter is caused by the lower OH densities in the plasma when Ag is present, as illustrated in Figure S1 d).

Nevertheless, the high net CO_2 destruction rate in the plasma in case of the Ag catalyst is largely compensated by the net CO_2 production on the Ag catalyst surface, as mentioned above, so the total net CO_2 destruction rate in the case of the Ag catalyst is clearly lower than in the plasma-only case (see Figure 17). Hence, our model predicts that an Ag catalyst is detrimental for the overall CO_2 conversion, compared to plasma without catalyst.

5.4.2 CH_4 destruction at steady state

Figure 18 presents the net steady state CH_4 destruction rates for the plasma-only case and the plasma combined with the three different catalysts. Similar to CO_2, CH_4 is net produced on the catalyst surfaces (as indicated by the hatched bars), through recombination of adsorbed CH_3* and H*. However, for Rh the rate of CH_4 formation on the catalyst is again extremely low due to surface poisoning, as is also the case for CO_2 formation on this metal. Among these three transition metals, the highest rate of CH_4 formation on the catalyst is now observed for Cu. In fact, the fast recombination of CH_3* and H* on the Cu surface results in a clear drop in the total net destruction rate of CH_4 compared to the other cases. Indeed, Cu was also identified as the best catalyst for radical recombination to CH_4 in the surface kinetics simulations with CatMAP, as displayed in Figure 15 a). Since the Cu catalyst gives the fastest recombination of H and CH_3 radicals to CH_4, it also causes the strongest drop of the CH_3 density in the plasma, as can be seen in Figure S1 b) in the SI. As a result, the net destruction of CH_4 in the plasma is faster for the case with Cu, compared to that with Rh or without catalyst (see Figure 18), exactly due to recombination between CH_3 and H happening now predominantly on the catalyst, causing a lower rate of the corresponding reaction in the gas phase.

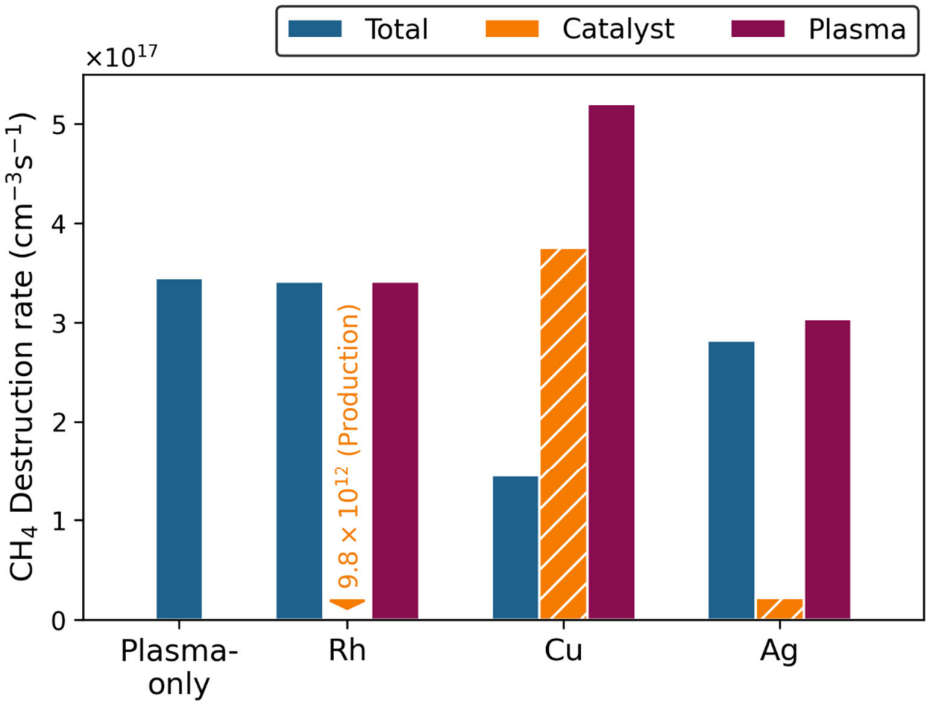

Figure 18. Net rates of CH_4 destruction at steady state ($t = 10^6$ s) for plasma without catalyst, or combined with a Rh, Cu or Ag catalyst. Distinction is made between the total rate, the rate on the catalyst surface and the rate in the plasma. Hatched bars indicate net production instead of destruction. The net (production) rate on the Rh surface is indicated by its numerical value, as it is many orders of magnitude lower compared to the other rates in the figure. Calculated for a 1:1 CH_4/CO_2 feed mixture using a total pressure of 1 bar and a temperature of 500 K.

For plasma combined with Ag, the total net rate of CH_4 destruction is also lowered compared to Rh and plasma-only. However, for this case the lower total CH_4 destruction results partly from recombination reactions that form CH_4 on the catalyst, and partly from lower CH_4 destruction in the plasma. The latter is caused by lower O and OH densities in the plasma when Ag is present as a catalyst, as illustrated in Figure S1 c) and d) in the SI, respectively. As shown in Figure 17, significant CO_2 formation occurs on the Ag surface, due to recombination of CO* and O* on this catalyst. Additionally, an even higher amount of O radicals is used on the Ag surface to form H_2O, as will be discussed in section 5.4.5 below. These processes in turn reduce the density of O radicals in the plasma, as illustrated in Figure S1 c). Since O radicals are partly responsible for CH_4 conversion in the plasma via $CH_4 + O \rightarrow CH_3 + OH$, the drop in O density also reduces the CH_4 destruction in the plasma. Additionally, the formed OH radicals can also convert CH_4 via $CH_4 + OH \rightarrow CH_3 + H_2O$. A drop in the O radical density also causes a drop in the OH density, which is formed from O, and both effects result in less CH_4 destruction in the plasma.

To summarize, while Cu results in a high net CH_4 destruction rate inside the plasma, it also causes the strongest drop in the total CH_4 destruction rate compared to plasma-only, due to quick recombination of CH_3* and H*, and thus CH_4 production, on the catalyst surface. Ag, on the other hand gives a less pronounced reduction of the CH_4 destruction rate compared to plasma without catalyst, but the effect of Ag is dual, i.e. due to both recombination of CH_3 and H on the catalyst, and less destruction of CH_4 via reactions with O and OH in the plasma (due to the lower densities of the latter species). In general, however, both Ag and especially Cu catalysts seem detrimental for the overall CH_4 conversion, compared to plasma-only, as predicted by our model.

5.4.3 CO production at steady state

The net rates of CO production are displayed in Figure 19. Note that hatched bars in the figure now indicate net destruction of CO on the catalyst surface, instead of formation. CO is mainly produced directly from CO_2 via electron impact dissociation in the plasma. However, by comparing the rates of CO production in Figure 19 and of CO_2 destruction in Figure 17, it becomes clear that CO production occurs faster and that a significant fraction of CO is not produced directly, i.e. not in a single step, from CO_2. Indeed, CO is also produced through decomposition of CH_3CO and dehydrogenation of CHO, which are formed by dehydrogenation of CH_3CHO and CH_2O, respectively. These aldehydes (CH_3CHO and CH_2O) in turn result from the oxidation of alkyl radicals (CH_3 and C_2H_5) by O, originating from CO_2.

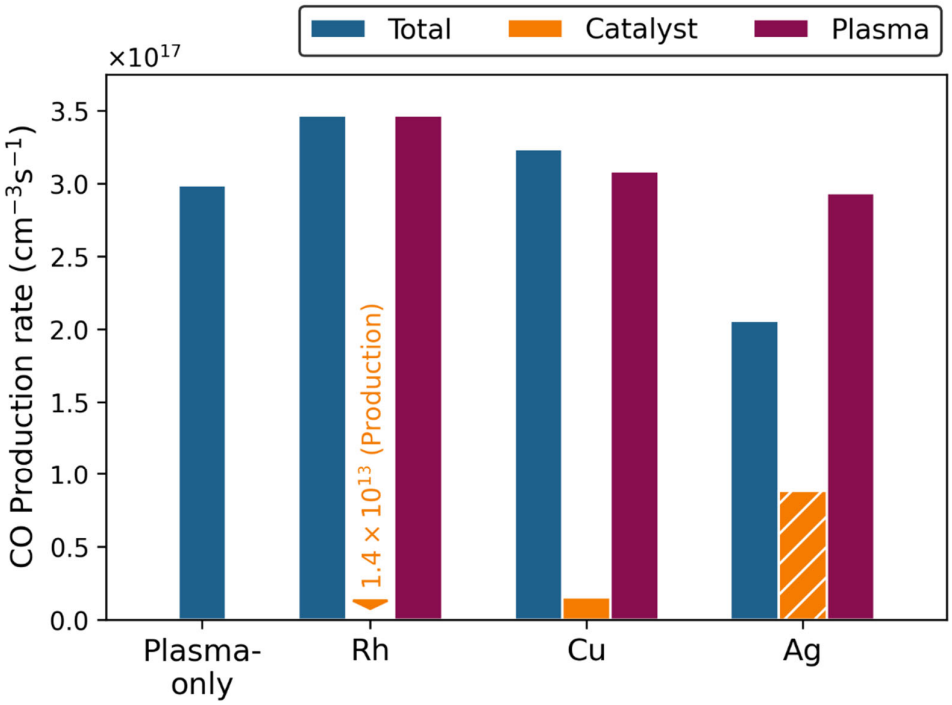

Figure 19. Net rates of CO production at steady state ($t = 10^6$ s) for plasma without catalyst, or combined with a Rh, Cu or Ag catalyst. Distinction is made between the total rate, the rate on the catalyst surface and the rate in the plasma. Hatched bars indicate net destruction instead of production. The net (production) rate on the Rh surface is indicated by its numerical value, as it is many orders of magnitude lower compared to the other rates in the figure. Calculated for a 1:1 CH_4/CO_2 feed mixture using a total pressure of 1 bar and a temperature of 500 K.

As is the case for CO_2 destruction in Figure 17, the CO production rate rises in the presence of Rh or Cu, compared to the plasma-only case. This can be partly attributed to the higher rate of $CO_2 + CH_2 \rightarrow CO + CH_2O$ in the plasma, as the lower H radical density (Figure S1 a) in the SI) causes a rise in the density of CH_2. Yet, the rise in CO production (Figure 19) is more significant compared to that of CO_2 destruction. Indeed, the drop in H density in the presence of the catalysts also suppresses hydrogenation and enhances dehydrogenation reactions. This increases the CO produced through dehydrogenation of CH_3CHO and CH_2O, as discussed above.

The rise in (total and plasma) CO production is less expressed for Cu compared to Rh. This is because Cu catalyzes recombination between CH_3* and H*, reducing the densities of CH_3 (Figure S1 b) in the SI), as well as C_2H_6 and thus C_2H_5, in the plasma. Indeed, C_2H_6 is formed by recombination of CH_3, and C_2H_5 is formed by dehydrogenation of C_2H_6. Since CH_3 and C_2H_5 play an important role in the formation of aldehydes (CH_3CHO and CH_2O) and also in dehydrogenating CHO, Cu produces less CO in the plasma, and also in total, compared to Rh. However, on the Cu surface, some dehydrogenation of

adsorbed CHO* takes place, forming CO* which can desorb to form CO or become oxidized to CO_2. As a result of this CO formation on the catalyst, the total CO production rate is slightly higher for Cu compared to the plasma-only case. The rate of CHO* decomposition on Rh is negligible due to surface poisoning.

For Ag the total CO production rate is lower relative to the plasma only-case, due to adsorption and subsequent oxidation of CO back to CO_2, as discussed in section 5.4.1. This is also clear from CO being net destroyed instead of produced on the catalyst, as displayed in Figure 19.

5.4.4 H_2 production at steady state

The net rates of H_2 production for the four different cases are displayed in Figure 20. The H_2 production rate appears especially high on the Rh surface, where recombination of adsorbed H* radicals to H_2 occurs the fastest. The fast destruction of H radicals on this catalyst, however, results in a lower H density in the plasma (see Figure S1 a) in the SI), which in turn reduces the rates of H_2 formation in the gas phase and causes a net destruction of H_2 in the plasma (hatched bar in Figure 20). However, H_2 production on the Rh catalyst is sufficiently fast to counter the net destruction of H_2 by plasma processes and leads to a total rate of H_2 production, which surpasses that of the plasma-only case. This is of course a positive effect, as H_2 is a value-added product. As discussed in section S2 in the SI, H adsorbs on a separate site type in our model, as it is assumed to have negligible interactions with the larger adsorbates on the surface. This allows H radicals to adsorb and recombine on the surface, even though the catalyst is poisoned by CO*. Note that H* can still react with other adsorbates on the surface, but H* recombination to H_2 is strongly favored over CO* hydrogenation.

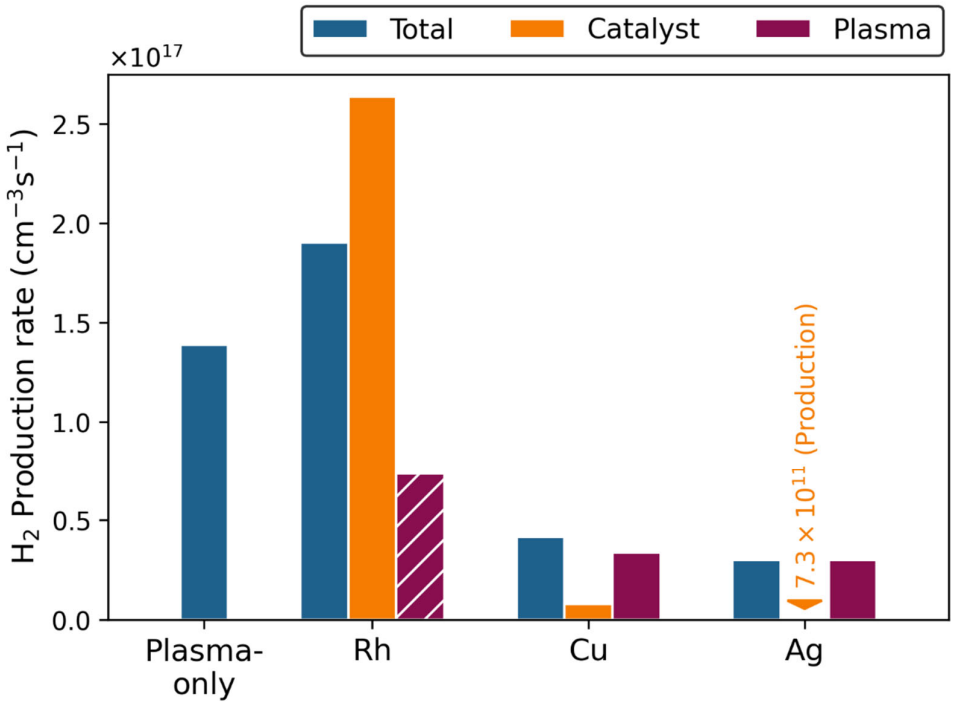

Figure 20. Net rates of H_2 production at steady state ($t = 10^6$ s) for plasma without catalyst, or combined with a Rh, Cu or Ag catalyst. Distinction is made between the total rate, the rate on the catalyst surface and the rate in the plasma. Hatched bars indicate net destruction instead of production. The net (production) rate on the Ag surface is indicated by its numerical value, as it is many orders of magnitude lower compared to the other rates in the figure. Calculated for a 1:1 CH_4/CO_2 feed mixture using a total pressure of 1 bar and a temperature of 500 K.

For the Cu and Ag catalysts, the H_2 production rate is positive in the plasma, yet clearly lower compared to the plasma-only case. This is due to the lower H densities in the plasma (see Figure S1 a) in the SI), due to H adsorption on these surfaces. However, on the Cu and Ag surfaces, the adsorbed H* is mainly used to form CH_4 and H_2O, rather than recombining to H_2. As such, the H_2 production rate is low on the Cu surface and negligible on the Ag surface. Because of the this, the total net H_2 production rates are significantly lower compared to the plasma without catalyst or with Rh catalyst.

5.4.5 H_2O production at steady state

In this section we discuss the formation of H_2O, which is an undesired side-product of plasma-catalytic DRM. Figure 21 shows the net rates of H_2O production for plasma-only and the different catalysts. H_2O is produced on all catalyst surfaces, although the net rate on Rh is negligible due to surface poisoning. Yet, on Cu and Ag surfaces, a non-negligible and even significant amount of H_2O is formed, respectively, via hydrogenation of adsorbed O*, or to a lesser extent, OH* radicals. For the Cu catalyst, the formation of H_2O on the surface results in an additional amount of H_2O formed on top of the large

production rate in the plasma. This increases the total rate of H_2O formation to a slightly higher value compared to the plasma-only case. For the Ag catalyst, on the other hand, formation on the catalyst surface appears by far the dominant mechanism of H_2O production. The high H_2O formation rate on the Ag surface is in agreement with the trend predicted by the surface kinetics simulation with CatMAP, as displayed in Figure 15 c). The quick adsorption of O and OH radicals from the plasma and their subsequent recombination with H on the catalyst significantly reduces the O and OH densities in the plasma, as shown in the SI, Figure S1 c) and d). This reduces the rates for H_2O formation in the gas phase and even causes net destruction of H_2O in the plasma.

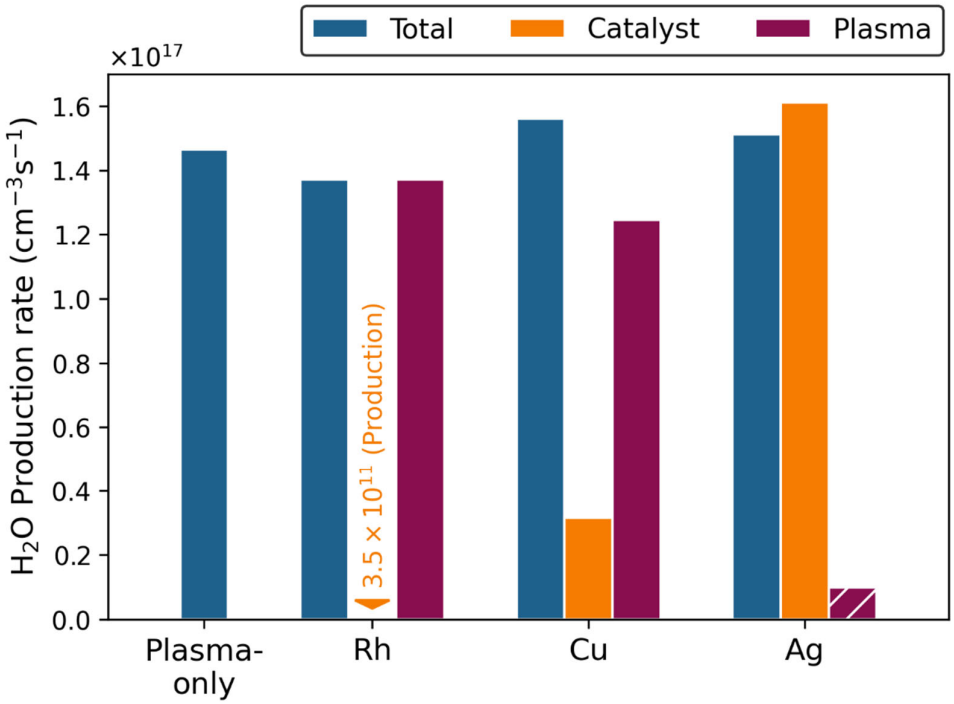

Figure 21. Net rates of H_2O production at steady state ($t = 10^6$ s) for plasma without catalyst, or combined with a Rh, Cu or Ag catalyst. Distinction is made between the total rate, the rate on the catalyst surface and the rate in the plasma. Hatched bars indicate net destruction instead of production. The net (production) rate on the Rh surface is indicated by its numerical value, as it is many orders of magnitude lower compared to the other rates in the figure. Calculated for a 1:1 CH_4/CO_2 feed mixture using a total pressure of 1 bar and a temperature of 500 K.

To summarize, despite the clearly different pathways for H_2O formation for the different catalysts (i.e., Rh and Cu, vs Ag), the total net rates of H_2O production do not vary much between the different cases, and are also very similar to the plasma-only case. Indeed, the H_2O formation is largely determined by the production of O radicals, which can either form H_2O in the plasma by abstracting H from H-containing species (e.g. CH_4) (in case of Rh and Cu), or adsorb and react with H on the catalyst surface

(in case of Ag). Whether or not the latter is favored depends on the supply of H to the surface and the activation barriers for hydrogenation to OH* and H_2O on the catalyst.

5.4.6 CH_3OH production at steady state

While typically not the main product, CH_3OH is a highly desired value-added chemical that could be formed in one step through plasma-catalytic DRM [10]. Therefore, it is especially interesting to investigate how CH_3OH formation is affected by the presence of the transition metal catalysts. Figure 22 displays the net production rates of CH_3OH for plasma without catalyst, as well as with Rh, Cu or Ag. Note that the vertical axis is now logarithmically scaled, to better visualize the trends. As can be seen, most of the CH_3OH is formed in the plasma, rather than on the catalyst surface. The highest CH_3OH formation rates on the surface are observed for Cu, followed by Ag. This is in agreement with the surface kinetics simulations performed with the CatMAP code, which predict Cu and Ag as the best catalysts for CH_3OH formation on the catalyst surface (cf. Figure 14 a)). However, while weakly binding catalysts, like Cu and Ag, produce more CH_3OH on the catalyst, this is not reflected in the total CH_3OH production. The latter is mainly determined by the CH_3OH production in the plasma (cf. the logarithmic scale to accommodate the large difference in magnitudes). As such, the highest total net CH_3OH formation is observed for the plasma without catalyst. Plasma combined with Rh, Cu or Ag, on the other hand, produces significantly less CH_3OH compared to the plasma-only case. The total net rate of CH_3OH production for the three catalysts is similar, although it is slightly reduced when going from Rh to Cu to Ag.

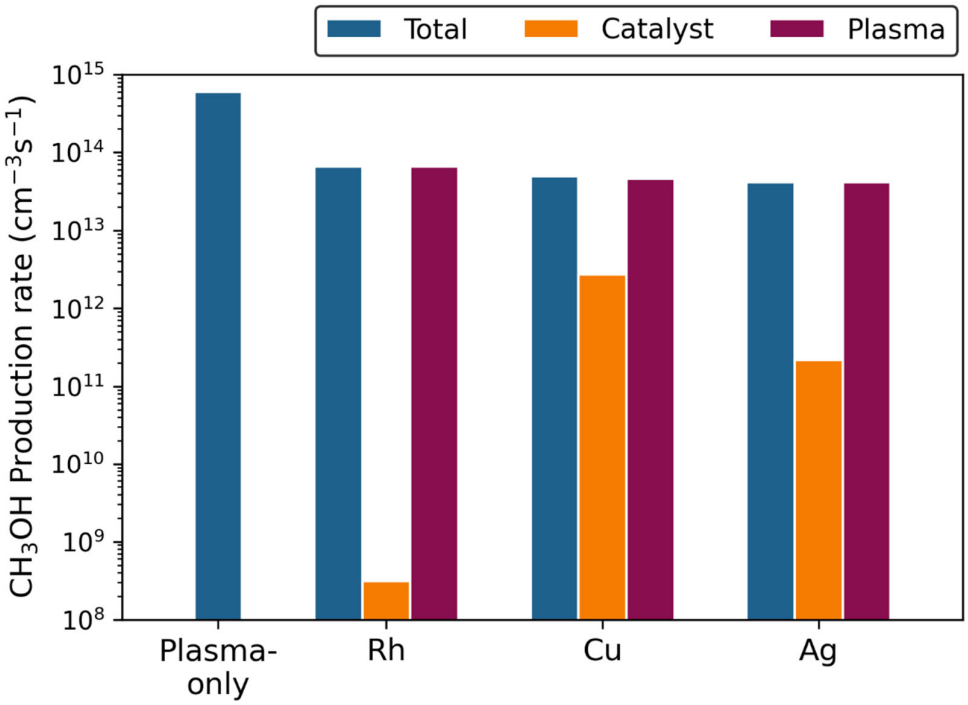

Figure 22. Net rates of CH_3OH production at steady state ($t = 10^6$ s) for plasma without catalyst, or combined with a Rh, Cu or Ag catalyst. Distinction is made between the total rate, the rate on the catalyst surface and the rate in the plasma. Note that the rates are logarithmically scaled. Calculated for a 1:1 CH_4/CO_2 feed mixture using a total pressure of 1 bar and a temperature of 500 K.

The formation of CH_3OH in the plasma-only case mainly occurs through pathways in which O radicals oxidize alkyl radicals (CH_3, C_2H_5) to form CH_2O, which subsequently reacts to form CH_2OH radicals. This species then recombines with H radicals into CH_3OH. Additionally, CH_3OH is also formed through recombination of CH_3 and OH, although to a lesser extent. When the plasma is in contact with a catalyst, however, radical adsorption and recombination on the surface causes a drop in the gas-phase densities of these species, as displayed in the SI in Figure S1 a), b) and d) for H, CH_3 and OH radicals, respectively. The reduction of these radical densities thus lowers the CH_3OH formation rate in the plasma. As discussed above, (very) small amounts of CH_3OH can be formed on the catalyst surfaces. For Rh and Cu, this occurs through adsorption of CH_2O, followed by hydrogenation to CH_3O* and subsequently, CH_3OH. On Ag, CHO is adsorbed from the gas phase and hydrogenated to CH_2O*, followed by the same reaction steps as on Rh and Cu. Hence, while adsorbed radicals can also react on the surface to form CH_3OH, this process is not favored and instead these species rather recombine to form either CH_4, CO_2, H_2O or H_2.

In summary, while CH_3OH formation does take place at the catalyst surfaces, the rate is much lower than the CH_3OH formation rate in the plasma, and the latter is significantly reduced compared to the

plasma-only case, due to adsorption of radicals at the catalyst surface, making them not available anymore for the plasma reactions producing CH_3OH.

Hence, our calculations suggest that transition metals would be detrimental for CH_3OH formation by plasma-catalytic DRM, at the conditions under study, because they mainly recombine radicals to undesired molecules (e.g., CH_4, CO_2 and H_2O). As such, these radicals are no longer available to form the desired end-compounds, like CH_3OH. Additionally, the plasma itself is already so reactive, due to the presence of the many radicals, so that the CH_3OH formation rate is largely dominated by plasma reactions. However, at the same time, the high plasma reactivity also hinders the selective production of the targeted compounds. Thus, careful analysis is needed on how the role of the catalyst can be promoted in plasma catalysis, but also on how the adsorbed radicals can be directed into desired, rather than unwanted products.

5.4.7 Summary of the insights provided by the model

Our coupled plasma-surface model allows us to study how the chemistry of the plasma and catalyst affect each other, as illustrated by comparing four different cases, namely plasma without catalyst or combined with Rh, Cu and Ag. Our model reveals that the presence of transition metal catalysts in plasma-catalytic DRM, for typical DBD conditions at which the radical chemistry dominates, has mainly negative, rather than positive effects. Indeed, we find that Ag has a detrimental effect on the net CO_2 destruction rate, as the catalyst efficiently recombines CO* and O* on the surface, and thus partly counteracts the dissociation of CO_2 in the plasma. The net destruction of CH_4, on the other hand, is especially reduced by Cu, due to facile recombination of CH_3* and H* on this catalyst. Additionally, the presence of Ag also slightly reduces the net CH_4 destruction rate. On one hand, this is caused by the formation of CH_4 on the surface. On the other hand, many O and OH radicals are adsorbed and subsequently converted to CO_2 and H_2O on the Ag surface, making these radicals unavailable for CH_4 destruction reactions in the gas-phase.

Our model also predicts that CO production mainly happens in the plasma, either directly from CO_2 or via various oxidation and dehydrogenation reactions. As such, the net production of CO is negatively affected by Ag, due to CO oxidation on the surface to form again CO_2. The production of H_2 is improved by Rh, due to adsorption of H radicals on hydrogen reservoir sites and facile subsequent recombination to H_2, while other catalytic sites are poisoned. However, on Cu and Ag, the adsorbed H* is primarily used for the production of CH_4 and H_2O, respectively, resulting in a significant drop of the net H_2 production. On the other hand, H_2O, as undesired side-product, is produced at similar net rates for all cases, yet the pathways through which the H_2O is formed depends on the catalyst. For Ag, most H_2O is formed on the catalyst, while for Cu and Rh, the H_2O production mainly happens in the plasma.

Most importantly, the CH_3OH production seems to be negatively affected by the presence of transition metal catalysts for the conditions under study. While some net CH_3OH formation occurs on the surfaces of all catalysts, the total CH_3OH production is mostly determined by plasma reactions. However, radicals that are lost from the plasma due to adsorption on the catalyst are primarily directed towards the formation of other products (i.e., CO_2, CH_4, CO, H_2 or H_2O) rather than CH_3OH. Consequently, the CH_3OH formation rate drops due to the loss of radicals from the plasma. This highlights the need to identify conditions and catalysts that can selectively produce CH_3OH from radicals and other plasma-produced species, to fully use the potential of plasma catalysis and avoid unwanted side-effects.

To conclude, our model illustrates that transition metal catalysts are detrimental to the radical chemistry for plasma-catalytic DRM, due to efficient back-reactions of the radicals on the catalyst. This indicates that plasma-catalyst synergy in DRM is unlikely to happen under conditions for which radicals are the dominant species for plasma catalysis, i.e., at typical (low temperature) DBD conditions. As such, plasma-catalytic DRM may benefit more from higher reaction temperatures, at which vibrational excitation can enhance the surface reactions (see section 4.3). This is in agreement with the work by Kim *et al.* [59] (discussed in section 4.1.1), who showed that vibrationally excited CH_4 could enhance plasma-catalytic DRM at temperatures in excess of 600 K, and also with the work of Sheng et al. [81,101], demonstrating the key role of vibrationally excited CO_2 and CH_4 molecules in promoting plasma-catalytic DRM. While high temperatures can also lead to increased V-T relaxation and thus less vibrationally excited species, this effect is only relevant for warm plasmas (typically with $T > 3000$ K), for which in-plasma catalysis is not possible [119]. Moreover, as we discussed in section 4.7, limiting the adsorption of CH_3 and O radicals, which can otherwise recombine with H* and CO*, back into CH_4 and CO_2, respectively, can also be beneficial for plasma-catalytic DRM. The formation of CH_3 and O may be limited if high conversion to CO and H_2 (which are typically the main products of plasma-catalytic DRM) can be achieved. This can subsequently also enable plasma-catalytic hydrogenation of CO and CO_2, in tandem with DRM, which would open up additional reaction pathways, like the HCOO* and RWGS pathways. Apart from the adsorption of H radicals, these pathways can also benefit from vibrational excitation of the CO_2 bending mode (for sufficiently high temperatures), as discussed in section 4.5.3. Of course, the presence of a transition metal catalyst in a DBD can also modify the discharge characteristics (section 3), which may (partly) counter the negative chemical interactions, but this would need further investigation.

Finally, it is important to note that while our model shows that the presence of a transition metal catalyst can negatively impact plasma-catalytic DRM at typical DBD conditions, this conclusion is not valid for all reactions. As such, a catalyst can still have a beneficial role in other plasma-catalytic reactions. It is also worth to mention that our model applies to transition metal catalysts, for which input data are most readily available in literature. The results might be different for non-metallic catalysts (e.g., oxides,

nitrides, etc.), although the problem of radicals being quenched by the catalyst and used for the back-reactions might still be present. This would however also require further investigation.

6 Conclusion

Plasma catalysis is a promising technology to convert two greenhouse gases, namely CO_2 and CH_4, into value-added chemicals like CH_3OH and other oxygenates, thus also providing an alternative for fossil resources to produce chemicals and fuels. Plasma-catalytic DRM has already been investigated in many experimental studies and with a broad range of catalysts. Yet the observations of these studies often differ, and as such there is no consensus on the mechanisms of plasma-catalytic DRM or even plasma catalysis in general. As we illustrate in this perspective paper, this can be attributed to the plethora of both physical and chemical interactions that occur between the plasma and the catalysts. This makes acquisition of fundamental insights very difficult, which is, in our opinion, a major bottleneck for the further development and optimization of plasma-catalytic applications for gas conversion, such as DRM. In this perspective paper, we therefore provide insight in the various physical and chemical effects that contribute to the high complexity of plasma catalysis. Indeed, not only interactions of reactive plasma species with the catalyst play a role, but the introduction of a catalyst or support packing also strongly affects the discharge behavior of the plasma. Various properties of the packing material and reactor setup determine the discharge type in the plasma, including the dielectric constant, the size of the packing beads and discharge gap, as well as the amount and type of metal nanoparticles loaded on the support. By altering the discharge type from localized microdischarges to surface discharges along the packing beads, the above parameters determine the contact between the plasma and the catalyst. Moreover, they also affect the electric field and electron temperature and consequently the electron impact reactions occurring in the plasma, which define the plasma chemistry. In addition, other material properties, like porosity, are also crucial in tuning the contact between plasma and catalyst. Even more, the comparison of different support packings in experimental studies is not straightforward, as different packings evolve to other partial chemical equilibria at different rates and thus perform differently depending on the gas residence time. Thus, the support packing can induce various physical effects, that strongly affect the plasma. This stresses the strong need for standardized experimental setups and elaborate documentation of packing properties, to disentangle the various effects and make progress in this important research field.

In addition to the already complex interplay of physical effects, plasma catalysis encompasses many chemical interactions as well. As we illustrate in this paper, there are many possible mechanisms by which reactive plasma species, like radicals and vibrationally excited molecules, can interact with the catalyst to alter the conversion and product selectivity. For example, by weakening or breaking bonds in the reactants, i.e., via vibration excitation and radicals, respectively, plasma can facilitate the dissociation of the reactant molecules on the catalyst. Additionally, other surface reaction steps can be enhanced by radical adsorption or E-R reactions, depending on which radicals can reach the surface. This can improve the reaction rates and consequently the product concentrations in the gas-phase, which

can even reach values beyond the thermal equilibrium. As such, plasma catalysis enables to circumvent the scaling relation for bond dissociation that are normally present in thermal catalysis.

However, plasma-catalyst synergy is not always observed. Indeed, while plasma catalysis can allow reactions to occur at lower temperatures compared to thermal catalysis, a certain light-off temperature is still necessary to activate surface reaction steps that are not directly affected by the plasma species. Additionally, plasma catalysis via vibrational excitation only becomes relevant at high temperatures, as a significant part of the activation barrier remains, while radical-based mechanisms can also occur at lower temperatures that are typical of a DBD. Moreover, depending on the mechanisms responsible for the plasma-catalyst synergy, i.e., vibrational excitation, adsorption of radicals or E-R reactions with radicals, the optimal catalyst also changes. Furthermore, the dominant mechanism for plasma-catalyst synergy and thus also the optimal catalyst is determined by the plasma species that reach the catalyst surface, and thus depends on the plasma chemistry, as well as the contact between plasma and catalyst. This again illustrates that plasma catalysis is a complex puzzle of many interactions that carefully need to be considered together.

Conversely, since the experimental results depend on many parameters, there are also many windows of opportunity to tune and optimize plasma-catalytic systems, which should be further exploited, but in a controlled way. Hence more research is needed to design optimal catalysts tailored to the plasma environment, as well as to design plasma reactors with optimal transport of plasma species towards the catalyst, and to tune the plasma conditions so that they work in optimal synergy with the catalyst.

We want the emphasize that a thorough understanding of the different physical and chemicals interactions is not only needed to optimally tailor the interplay between these effects, but also to avoid conditions under which they negatively affect the process. Indeed, combining a plasma with a catalyst can also adversely influence the conversions and product selectivities, as demonstrated in several experiments. However, this effect is, in our opinion, often still underestimated. Therefore, we provide insights from our own, newly developed model to demonstrate how the presence of a transition metal catalyst can have a detrimental effect on the CH_4 and CO_2 conversion and CH_3OH selectivity for DRM at typical DBD conditions at which the radical chemistry dominates. We illustrate that plasma-produced radicals, which are indeed the dominant species for plasma catalysis at typical DBD conditions, can easily recombine back to the reactants, CH_4 and CO_2, on the surfaces of weakly binding metals (Cu, Ag). This back-reaction reduces the reactant conversions and also directs radicals reaching the surface away from CH_3OH production, resulting in a drop of the CH_3OH formation compared to plasma without catalyst. Nevertheless, CH_3OH can still be created via plasma catalysis, through surface-hydrogenation of plasma-produced CO* or CH_xO* by adsorbed H* radicals. Yet, CH_3OH production from this pathway is negligible in DRM, as CO* and H* are scavenged from the surface by O* and CH_3* to produce CO_2 and CH_4, respectively.

Hence, we propose that, in order to avoid back-reaction to CH_4 and CO_2, as well as to improve the plasma-catalytic CH_3OH (or other oxygenate) selectivity, the flux of CH_3 and O radicals to the catalyst should remain limited without impairing the adsorption of CO and H radicals. We suggest that this might be achieved by diluting the CH_4/CO_2 gas mixture with syngas (CO/H_2) to avoid the formation of CH_3 and O radicals as much as possible, thus enabling plasma-catalytic CO_2/CO hydrogenation in tandem with DRM. Enriching the reactant mixture with CO and H_2 can also be achieved by performing plasma-catalytic DRM at high temperatures, for which CO and H_2 become thermodynamically favored over CH_4 and CO_2. We propose that strongly binding catalysts (like Ni) are used for syngas production, as these can break the strong C-H bonds in CH_4. Moreover, this combination of high temperature and a relative strongly binding catalyst would also enable plasma catalysis via vibrational excitation, which is more energy efficient than a radical-driven mechanism. Subsequently, the CO/H_2-enriched gas mixture can be used for CH_3OH formation in a DBD at low temperature, for which the radical chemistry is dominant. We suggest a weakly binding catalyst (e.g., Cu) to be used for this reaction, as these are typically more selective towards CH_3OH due to the higher barrier for C-O bond dissociation, and less likely to be hindered by surface poisoning. However, the plasma chemistry should be carefully tailored to avoid dissociation or weakening of the C-O bond, while H_2 dissociation should be enhanced.

Thus, our model illustrates that the presence of a transition metal catalyst has a negative effect on plasma-catalytic DRM if the plasma-catalyst interactions are dominated by radicals, which is typically the case in a DBD plasma at low temperature. However, the radical chemistry may still be beneficial if back-reactions to CH_4 and CO_2 can be omitted, by lowering the amount of CH_3 and O radicals that adsorb on the surface. We suggest that this can be achieved by attaining high conversion to syngas first, leading to a combination of plasma-catalytic DRM and CO_2/CO hydrogenation. Note that our model only applies to transition metal catalysts, and the results might be different for non-metallic catalysts, but this requires further investigation.

On the other hand, we expect that plasma-catalytic synergy can be achieved for DRM at higher temperatures in combination with vibrational excitation. It has indeed been demonstrated in literature that vibrationally excited CH_4 and CO_2 molecules are key in promoting plasma-catalyst synergy in DRM. Hence, plasma conditions should be exploited where vibrationally excited CH_4 and CO_2 molecules are more important than radicals, although this is not so evident in DBD plasmas.

We hope to have illustrated that detailed insight in the various mechanisms of plasma catalysis is necessary to identify reaction conditions, catalysts and packing properties that stimulate the occurrence of specific synergistic effects. Moreover, the plasma-catalyst interactions should be tailored to optimally work together, while special care should also be taken to avoid adverse effects. Thus, more experimental and modelling studies are needed to further elucidate the underlying mechanisms, but the complex interplay of both physical and chemical effects hampers a direct comparison between different studies.

Therefore, we want to again emphasize the strong need to develop a standardized design for experiments, to facilitate comparison of different catalysts and reaction conditions between experimental studies.

Acknowledgements

This research was supported by the FWO-SBO project PlasMaCatDESIGN (FWO grant ID S001619N), the FWO fellowship of R. Michiels (FWO grant ID 1114921N), and the European Research Council (ERC) under the European Union's Horizon 2020 research and innovation programme (grant agreement No 810182 – SCOPE ERC Synergy project). The computational resources and services used in this work were provided by the HPC core facility CalcUA of the Universiteit Antwerpen, and VSC (Flemish Supercomputer Center), funded by the Research Foundation - Flanders (FWO) and the Flemish Government.

References

[1] H.-O. Pörtner, D.C. Roberts, M. Tignor, E.S. Poloczanska, K. Mintenbeck, A. Alegría, M. Craig, S. Langsdorf, S. Löschke, V. Möller, A. Okem, B. Rama, eds., IPCC, 2022: Climate Change 2022: Impacts, Adaptation and Vulnerability. Contribution of Working Group II to the Sixth Assessment Report of the Intergovernmental Panel on Climate Change, Cambridge University Press, Cambridge, UK and New York, NY, USA, 2022. https://doi.org/10.1017/9781009325844.

[2] National Oceanic and Atmospheric Administration. Trends in Atmospheric Carbon Dioxide. https://gml.noaa.gov/ccgg/trends/global.html (accessed February 15, 2023).

[3] X. Lan, K.W. Thoning, E.J. Dlugokencky, Trends in globally-averaged CH4, N2O, and SF6 determined from NOAA Global Monitoring Laboratory measurements. Version 2023-02. https://doi.org/10.15138/P8XG-AA10 (accessed February 15, 2023).

[4] J.T. Houghton, Y. Ding, D.J. Griggs, M. Noguer, P.J. van der Linden, X. Dai, K. Maskell, C.A. Johnson, eds., IPCC, 2001: Climate Change 2001: The Scientific Basis. Contribution of Working Group I to the Third Assessment Report of the Intergovernmental Panel on Climate Change, Cambridge University Press, Cambridge, United Kingdom and New York, NY, USA, 2001.

[5] A. Goeppert, M. Czaun, J.-P. Jones, G.K.S. Prakash, G.A. Olah, Chem. Soc. Rev. 43 (2014) 7995–8048. https://doi.org/10.1039/C4CS00122B.

[6] D. Pakhare, J. Spivey, Chem. Soc. Rev. 43 (2014) 7813–7837. https://doi.org/10.1039/C3CS60395D.

[7] N.A.K. Aramouni, J.G. Touma, B.A. Tarboush, J. Zeaiter, M.N. Ahmad, Renewable Sustainable Energy Rev. 82 (2018) 2570–2585. https://doi.org/10.1016/j.rser.2017.09.076.

[8] R. Snoeckx, A. Bogaerts, Chem. Soc. Rev. 46 (2017) 5805–5863. https://doi.org/10.1039/C6CS00066E.

[9] A. Bogaerts, X. Tu, J.C. Whitehead, G. Centi, L. Lefferts, O. Guaitella, F. Azzolina-Jury, H.-H. Kim, A.B. Murphy, W.F. Schneider, T. Nozaki, J.C. Hicks, A. Rousseau, F. Thevenet, A. Khacef, M. Carreon, J. Phys. D: Appl. Phys. 53 (2020) 443001. https://doi.org/10.1088/1361-6463/ab9048.

[10] S. Liu, L.R. Winter, J.G. Chen, ACS Catal. 10 (2020) 2855–2871. https://doi.org/10.1021/acscatal.9b04811.

[11] J. Van Turnhout, D. Aceto, A. Travert, P. Bazin, F. Thibault-Starzyk, A. Bogaerts, F. Azzolina-Jury, Catal. Sci. Technol. 12 (2022) 6676–6686. https://doi.org/10.1039/D2CY00311B.

[12] A. Wang, J.H. Harrhy, S. Meng, P. He, L. Liu, H. Song, Energy Convers. Manag. 191 (2019) 93–101. https://doi.org/10.1016/j.enconman.2019.04.026.

[13] J.A. Andersen, J.M. Christensen, M. Østberg, A. Bogaerts, A.D. Jensen, Chem. Eng. J. 397 (2020) 125519. https://doi.org/10.1016/j.cej.2020.125519.

[14] J. Sentek, K. Krawczyk, M. Młotek, M. Kalczewska, T. Kroker, T. Kolb, A. Schenk, K.-H. Gericke, K. Schmidt-Szałowski, Appl. Catal. B Environ. 94 (2010) 19–26. https://doi.org/10.1016/j.apcatb.2009.10.016.

[15] L. Wang, Y. Yi, C. Wu, H. Guo, X. Tu, Angew. Chem., Int. Ed. 56 (2017) 13679–13683. https://doi.org/10.1002/anie.201707131.

[16] R. Vakili, R. Gholami, C.E. Stere, S. Chansai, H. Chen, S.M. Holmes, Y. Jiao, C. Hardacre, X. Fan, Appl. Catal. B Environ. 260 (2020) 118195. https://doi.org/10.1016/j.apcatb.2019.118195.

[17] D. Mei, M. Sun, S. Liu, P. Zhang, Z. Fang, X. Tu, J. CO2 Util. 67 (2023) 102307. https://doi.org/10.1016/j.jcou.2022.102307.

[18] Y. Wang, L. Fan, H. Xu, X. Du, H. Xiao, J. Qian, Y. Zhu, X. Tu, L. Wang, Appl. Catal. B Environ. 315 (2022) 121583. https://doi.org/10.1016/j.apcatb.2022.121583.

[19] Y. Zeng, X. Zhu, D. Mei, B. Ashford, X. Tu, Catal. Today. 256 (2015) 80–87. https://doi.org/10.1016/j.cattod.2015.02.007.

[20] D. Li, V. Rohani, F. Fabry, A. Parakkulam Ramaswamy, M. Sennour, L. Fulcheri, Appl. Catal. B Environ. 261 (2020) 118228. https://doi.org/10.1016/j.apcatb.2019.118228.

[21] L. Dou, Y. Liu, Y. Gao, J. Li, X. Hu, S. Zhang, K. (Ken) Ostrikov, T. Shao, Appl. Catal. B Environ. 318 (2022) 121830. https://doi.org/10.1016/j.apcatb.2022.121830.

[22] D. Ray, P.M.K. Reddy, C. Subrahmanyam, Catal. Today. 309 (2018) 212–218. https://doi.org/10.1016/j.cattod.2017.07.003.

[23] Y. Diao, X. Zhang, Y. Liu, B. Chen, G. Wu, C. Shi, Appl. Catal. B Environ. 301 (2022) 120779. https://doi.org/10.1016/j.apcatb.2021.120779.

[24] A.H. Khoja, M. Tahir, N.A. Saidina Amin, Int. J. Hydrogen Energy. 44 (2019) 11774–11787. https://doi.org/10.1016/j.ijhydene.2019.03.059.

[25] J. Li, L. Dou, Y. Gao, X. Hei, F. Yu, T. Shao, J. CO2 Util. 52 (2021) 101675. https://doi.org/10.1016/j.jcou.2021.101675.

[26] D. Ray, P. Chawdhury, C. Subrahmanyam, ACS Omega. 5 (2020) 14040–14050. https://doi.org/10.1021/acsomega.0c01442.

[27] Y.X. Zeng, L. Wang, C.F. Wu, J.Q. Wang, B.X. Shen, X. Tu, Appl. Catal. B Environ. 224 (2018) 469–478. https://doi.org/10.1016/j.apcatb.2017.10.017.

[28] A. Bogaerts, E.C. Neyts, O. Guaitella, A.B. Murphy, Plasma Sources Sci. Technol. 31 (2022) 053002. https://doi.org/10.1088/1361-6595/ac5f8e.

[29] E.C. Neyts, A. Bogaerts, J. Phys. D: Appl. Phys. 47 (2014) 224010. https://doi.org/10.1088/0022-3727/47/22/224010.

[30] E.C. Neyts, K.K. Ostrikov, M.K. Sunkara, A. Bogaerts, Chem. Rev. 115 (2015) 13408–13446. https://doi.org/10.1021/acs.chemrev.5b00362.

[31] H. Kim, Y. Teramoto, A. Ogata, J. Phys. D: Appl. Phys. 49 (2016) 415204. https://doi.org/10.1088/0022-3727/49/41/415204.

[32] W. Wang, H.-H. Kim, K. Van Laer, A. Bogaerts, Chem. Eng. J. 334 (2018) 2467–2479. https://doi.org/10.1016/j.cej.2017.11.139.

[33] IST-Lisbon database. www.lxcat.net (accessed January 4, 2023).

[34] D. Reiter, R.K. Janev, Contrib. to Plasma Phys. 50 (2010) 986–1013. https://doi.org/10.1002/ctpp.201000090.

[35] L.S. Polak, D.I. Slovetsky, Int. J. Radiat. Phys. Chem. 8 (1976) 257–282. https://doi.org/10.1016/0020-7055(76)90070-X.

[36] X. Tu, H.J. Gallon, M. V. Twigg, P.A. Gorry, J.C. Whitehead, J. Phys. D: Appl. Phys. 44 (2011). https://doi.org/10.1088/0022-3727/44/27/274007.

[37] H.-H. Kim, J.-H. Kim, A. Ogata, J. Phys. D: Appl. Phys. 42 (2009) 135210. https://doi.org/10.1088/0022-3727/42/13/135210.

[38] H.-H. Kim, A. Ogata, Eur. Phys. J. Appl. Phys. 55 (2011) 13806. https://doi.org/10.1051/epjap/2011100444.

[39] C. Ndayirinde, Y. Gorbanev, R.-G. Ciocarlan, R. De Meyer, A. Smets, E. Vlasov, S. Bals, P.

Cool, A. Bogaerts, Catal. Today. 419 (2023) 114156. https://doi.org/10.1016/j.cattod.2023.114156.

[40] K. Van Laer, A. Bogaerts, Plasma Sources Sci. Technol. 26 (2017) 085007. https://doi.org/10.1088/1361-6595/aa7c59.

[41] K. Van Laer, A. Bogaerts, Plasma Process. Polym. 14 (2017) 1600129. https://doi.org/10.1002/ppap.201600129.

[42] Y. Uytdenhouwen, S. Van Alphen, I. Michielsen, V. Meynen, P. Cool, A. Bogaerts, Chem. Eng. J. 348 (2018) 557–568. https://doi.org/10.1016/j.cej.2018.04.210.

[43] T. Butterworth, R. Elder, R. Allen, Chem. Eng. J. 293 (2016) 55–67. https://doi.org/10.1016/j.cej.2016.02.047.

[44] H.L. Chen, H.M. Lee, S.H. Chen, M.B. Chang, Ind. Eng. Chem. Res. 47 (2008) 2122–2130. https://doi.org/10.1021/ie071411s.

[45] S. Veerapandian, C. Leys, N. De Geyter, R. Morent, Catalysts. 7 (2017) 113. https://doi.org/10.3390/catal7040113.

[46] A. Ogata, H. Einaga, H. Kabashima, S. Futamura, S. Kushiyama, H.-H. Kim, Appl. Catal. B Environ. 46 (2003) 87–95. https://doi.org/10.1016/S0926-3373(03)00180-2.

[47] A. Ogata, N. Shintani, K. Mizuno, S. Kushiyama, T. Yamamoto, IEEE Trans. Ind. Appl. 35 (1999) 753–759. https://doi.org/10.1109/28.777181.

[48] I. Michielsen, Y. Uytdenhouwen, A. Bogaerts, V. Meynen, Catalysts. 9 (2019) 51. https://doi.org/10.3390/catal9010051.

[49] Q.Z. Zhang, A. Bogaerts, Plasma Sources Sci. Technol. 27 (2018) 35009. https://doi.org/10.1088/1361-6595/aab47a.

[50] R. Snoeckx, R. Aerts, X. Tu, A. Bogaerts, J. Phys. Chem. C. 117 (2013) 4957–4970. https://doi.org/10.1021/jp311912b.

[51] Y.-R. Zhang, K. Van Laer, E.C. Neyts, A. Bogaerts, Appl. Catal. B Environ. 185 (2016) 56–67. https://doi.org/10.1016/j.apcatb.2015.12.009.

[52] H.-H. Kim, Y. Teramoto, N. Negishi, A. Ogata, Catal. Today. 256 (2015) 13–22. https://doi.org/10.1016/j.cattod.2015.04.009.

[53] T. Nozaki, N. Muto, S. Kado, K. Okazaki, Catal. Today. 89 (2004) 57–65. https://doi.org/10.1016/j.cattod.2003.11.040.

[54] M. Mikhail, P. Da Costa, J. Amouroux, S. Cavadias, M. Tatoulian, M.E. Gálvez, S. Ognier, Appl. Catal. B Environ. 294 (2021) 120233. https://doi.org/10.1016/j.apcatb.2021.120233.

[55] R. Dębek, F. Azzolina-Jury, A. Travert, F. Maugé, Renewable Sustainable Energy Rev. 116 (2019) 109427. https://doi.org/10.1016/j.rser.2019.109427.

[56] X. Gao, Z. Wang, Q. Huang, M. Jiang, S. Askari, N. Dewangan, S. Kawi, Catal. Today. 402 (2022) 88–103. https://doi.org/10.1016/j.cattod.2022.03.017.

[57] W.C. Chung, M.B. Chang, Renewable Sustainable Energy Rev. 62 (2016) 13–31. https://doi.org/10.1016/j.rser.2016.04.007.

[58] Y. Uytdenhouwen, K.M. Bal, I. Michielsen, E.C. Neyts, V. Meynen, P. Cool, A. Bogaerts, Chem. Eng. J. 372 (2019) 1253–1264. https://doi.org/10.1016/j.cej.2019.05.008.

[59] J. Kim, M.S. Abbott, D.B. Go, J.C. Hicks, ACS Energy Lett. 1 (2016) 94–99. https://doi.org/10.1021/acsenergylett.6b00051.

[60] K.H.R. Rouwenhorst, H.G.B. Burbach, D.W. Vogel, J. Núñez Paulí, B. Geerdink, L. Lefferts, Catal. Sci. Technol. 11 (2021) 2834–2843. https://doi.org/10.1039/d0cy02189j.

[61] P. Mehta, P.M. Barboun, Y. Engelmann, D.B. Go, A. Bogaerts, W.F. Schneider, J.C. Hicks, ACS Catal. 10 (2020) 6726–6734. https://doi.org/10.1021/acscatal.0c00684.

[62] R.R. Smith, D.R. Killelea, D.F. DelSesto, A.L. Utz, Science (80-.). 304 (2004) 992–995. https://doi.org/10.1126/science.1096309.

[63] E. Dombrowski, E. Peterson, D. Del Sesto, A.L. Utz, Catal. Today. 244 (2015) 10–18. https://doi.org/10.1016/j.cattod.2014.10.025.

[64] P.M. Barboun, L.L. Daemen, C. Waitt, Z. Wu, W.F. Schneider, J.C. Hicks, ACS Energy Lett. 6 (2021) 2048–2053. https://doi.org/10.1021/acsenergylett.1c00643.

[65] P.M. Barboun, H.O. Otor, H. Ma, A. Goswami, W.F. Schneider, J.C. Hicks, ACS Sustain. Chem. Eng. 10 (2022) 15741–15748. https://doi.org/10.1021/acssuschemeng.2c04217.

[66] P. Mehta, P. Barboun, D.B. Go, J.C. Hicks, W.F. Schneider, ACS Energy Lett. 4 (2019) 1115–1133. https://doi.org/10.1021/acsenergylett.9b00263.

[67] Y. Yi, S. Li, Z. Cui, Y. Hao, Y. Zhang, L. Wang, P. Liu, X. Tu, X. Xu, H. Guo, A. Bogaerts, Appl. Catal. B Environ. 296 (2021) 120384. https://doi.org/10.1016/j.apcatb.2021.120384.

[68] B. Christian Enger, R. Lødeng, A. Holmen, Appl. Catal. A. 346 (2008) 1–27. https://doi.org/10.1016/j.apcata.2008.05.018.

[69] J.K. Nørskov, F. Studt, F. Abild-Pedersen, T. Bligaard, Fundamental Concepts in Heterogeneous Catalysis, John Wiley & Sons, Inc., Hoboken, New Jersey, 2014.

[70] P. Mehta, P. Barboun, F.A. Herrera, J. Kim, P. Rumbach, D.B. Go, J.C. Hicks, W.F. Schneider, Nat. Catal. 1 (2018) 269–275. https://doi.org/10.1038/s41929-018-0045-1.

[71] Y. Engelmann, K. Van'T Veer, Y. Gorbanev, E.C. Neyts, W.F. Schneider, A. Bogaerts, ACS Sustain. Chem. Eng. 9 (2021) 13151–13163. https://doi.org/10.1021/acssuschemeng.1c02713.

[72] H. Ma, W.F. Schneider, J. Phys. D: Appl. Phys. 54 (2021) 454004. https://doi.org/10.1088/1361-6463/ac1bd1.

[73] H. Ma, R.K. Sharma, S. Welzel, M.C.M. van de Sanden, M.N. Tsampas, W.F. Schneider, Nat. Commun. 13 (2022) 402. https://doi.org/10.1038/s41467-021-27912-2.

[74] Y. Engelmann, P. Mehta, E.C. Neyts, W.F. Schneider, A. Bogaerts, ACS Sustain. Chem. Eng. 8 (2020) 6043–6054. https://doi.org/10.1021/acssuschemeng.0c00906.

[75] R. Michiels, Y. Engelmann, A. Bogaerts, J. Phys. Chem. C. 124 (2020) 25859–25872. https://doi.org/10.1021/acs.jpcc.0c07632.

[76] B. Loenders, Y. Engelmann, A. Bogaerts, J. Phys. Chem. C. 125 (2021) 2966–2983. https://doi.org/10.1021/acs.jpcc.0c09849.

[77] E. Meloni, M. Martino, V. Palma, Catalysts. 10 (2020) 352. https://doi.org/10.3390/catal10030352.

[78] J.S. Hummelshøj, F. Abild-Pedersen, F. Studt, T. Bligaard, J.K. Nørskov, Angew. Chemie. 124 (2012) 278–280. https://doi.org/10.1002/ange.201107947.

[79] P.J. Linstrom, W.G. Mallard, eds., NIST Chemistry WebBook, NIST Standard Reference Database Number 69, National Institute of Standards and Technology, Gaithersburg MD, 20899, . https://doi.org/10.18434/T4D303.

[80] K.H.R. Rouwenhorst, H.H. Kim, L. Lefferts, ACS Sustain. Chem. Eng. 7 (2019) 17515–17522. https://doi.org/10.1021/acssuschemeng.9b04997.

[81] Z. Sheng, Y. Watanabe, H.-H. Kim, S. Yao, T. Nozaki, Chem. Eng. J. 399 (2020) 125751. https://doi.org/10.1016/j.cej.2020.125751.

[82] J. Kim, D.B. Go, J.C. Hicks, Phys. Chem. Chem. Phys. 19 (2017) 13010–13021. https://doi.org/10.1039/C7CP01322A.

[83] S. Xu, S. Chansai, Y. Shao, S. Xu, Y. chi Wang, S. Haigh, Y. Mu, Y. Jiao, C.E. Stere, H. Chen, X. Fan, C. Hardacre, Appl. Catal. B Environ. 268 (2020) 118752. https://doi.org/10.1016/j.apcatb.2020.118752.

[84] N. Jidenko, E. Bourgeois, J.-P. Borra, J. Phys. D: Appl. Phys. 43 (2010) 295203. https://doi.org/10.1088/0022-3727/43/29/295203.

[85] J. Jiang, P.J. Bruggeman, Plasma Chem. Plasma Process. 42 (2022) 689–707. https://doi.org/10.1007/s11090-022-10251-5.

[86] E.K. Gibson, C.E. Stere, B. Curran-McAteer, W. Jones, G. Cibin, D. Gianolio, A. Goguet, P.P. Wells, C.R.A. Catlow, P. Collier, P. Hinde, C. Hardacre, Angew. Chem., Int. Ed. 56 (2017) 9351–9355. https://doi.org/10.1002/anie.201703550.

[87] A. Parastaev, N. Kosinov, E.J.M. Hensen, J. Phys. D: Appl. Phys. 54 (2021) 264004. https://doi.org/10.1088/1361-6463/abeb96.

[88] B. Eliasson, U. Kogelschatz, B. Xue, L.-M. Zhou, Ind. Eng. Chem. Res. 37 (1998) 3350–3357. https://doi.org/10.1021/ie9709401.

[89] F. Ahmad, E.C. Lovell, H. Masood, P.J. Cullen, K.K. Ostrikov, J.A. Scott, R. Amal, ACS Sustain. Chem. Eng. 8 (2020) 1888–1898. https://doi.org/10.1021/acssuschemeng.9b06180.

[90] A.O. Elnabawy, J. Schumann, P. Bothra, A. Cao, J.K. Nørskov, Top. Catal. 63 (2020) 635–648. https://doi.org/10.1007/s11244-020-01283-2.

[91] J. Schumann, A.J. Medford, J.S. Yoo, Z.-J. Zhao, P. Bothra, A. Cao, F. Studt, F. Abild-Pedersen, J.K. Nørskov, ACS Catal. 8 (2018) 3447–3453. https://doi.org/10.1021/acscatal.8b00201.

[92] A.J. Medford, A.C. Lausche, F. Abild-Pedersen, B. Temel, N.C. Schjødt, J.K. Nørskov, F. Studt, Top. Catal. 57 (2014) 135–142. https://doi.org/10.1007/s11244-013-0169-0.

[93] A. Parastaev, W.F.L.M. Hoeben, B.E.J.M. van Heesch, N. Kosinov, E.J.M. Hensen, Appl. Catal. B Environ. 239 (2018) 168–177. https://doi.org/10.1016/j.apcatb.2018.08.011.

[94] J. Quan, F. Muttaqien, T. Kondo, T. Kozarashi, T. Mogi, T. Imabayashi, Y. Hamamoto, K.

Inagaki, I. Hamada, Y. Morikawa, J. Nakamura, Nat. Chem. 11 (2019) 722–729. https://doi.org/10.1038/s41557-019-0282-1.

[95] D.-Y. Kim, H. Ham, X. Chen, S. Liu, H. Xu, B. Lu, S. Furukawa, H.-H. Kim, S. Takakusagi, K. Sasaki, T. Nozaki, J. Am. Chem. Soc. 144 (2022) 14140–14149. https://doi.org/10.1021/jacs.2c03764.

[96] L. Wang, Y. Yi, H. Guo, X. Tu, ACS Catal. 8 (2018) 90–100. https://doi.org/10.1021/acscatal.7b02733.

[97] A.J. Medford, C. Shi, M.J. Hoffmann, A.C. Lausche, S.R. Fitzgibbon, T. Bligaard, J.K. Nørskov, Catal. Letters. 145 (2015) 794–807. https://doi.org/10.1007/s10562-015-1495-6.

[98] C. De Bie, J. van Dijk, A. Bogaerts, J. Phys. Chem. C. 119 (2015) 22331–22350. https://doi.org/10.1021/acs.jpcc.5b06515.

[99] H. Falsig, B. Hvolbæk, I.S. Kristensen, T. Jiang, T. Bligaard, C.H. Christensen, J.K. Nørskov, Angew. Chem., Int. Ed. 47 (2008) 4835–4839. https://doi.org/10.1002/anie.200801479.

[100] J.T. Kummer, J. Phys. Chem. 90 (1986) 4747–4752. https://doi.org/10.1021/j100411a008.

[101] Z. Sheng, H.-H. Kim, S. Yao, T. Nozaki, Phys. Chem. Chem. Phys. 22 (2020) 19349–19358. https://doi.org/10.1039/D0CP03127E.

[102] P.-A. Maitre, M.S. Bieniek, P.N. Kechagiopoulos, J. Phys. Chem. C. 126 (2022) 19987–20003. https://doi.org/10.1021/acs.jpcc.2c03503.

[103] Y. Gorbanev, Y. Engelmann, K. van't Veer, E. Vlasov, C. Ndayirinde, Y. Yi, S. Bals, A. Bogaerts, Catalysts. 11 (2021) 1230. https://doi.org/10.3390/catal11101230.

[104] J. Shah, F. Gorky, P. Psarras, B. Seong, D.A. Gómez-Gualdrón, M.L. Carreon, ChemCatChem. 12 (2020) 1200–1211. https://doi.org/10.1002/cctc.201901769.

[105] Y. Wang, M. Craven, X. Yu, J. Ding, P. Bryant, J. Huang, X. Tu, ACS Catal. 9 (2019) 10780–10793. https://doi.org/10.1021/acscatal.9b02538.

[106] J. Hong, S. Pancheshnyi, E. Tam, J.J. Lowke, S. Prawer, A.B. Murphy, J. Phys. D: Appl. Phys. 50 (2017) 154005. https://doi.org/10.1088/1361-6463/aa6229.

[107] K. van 't Veer, Y. Engelmann, F. Reniers, A. Bogaerts, J. Phys. Chem. C. 124 (2020) 22871–22883. https://doi.org/10.1021/acs.jpcc.0c05110.

[108] M. Xi, B.E. Bent, J. Phys. Chem. 97 (1993) 4167–4172. https://doi.org/10.1021/j100118a037.

[109] C.T. Rettner, D.J. Auerbach, J. Lee, J. Chem. Phys. 105 (1996) 10115–10122. https://doi.org/10.1063/1.472840.

[110] W.H. Weinberg, Acc. Chem. Res. 29 (1996) 479–487. https://doi.org/10.1021/ar9500980.

[111] Y. Yi, S. Li, Z. Cui, Y. Hao, Y. Zhang, L. Wang, P. Liu, X. Tu, X. Xu, H. Guo, A. Bogaerts, Appl. Catal. B Environ. 296 (2021) 120384. https://doi.org/10.1016/j.apcatb.2021.120384.

[112] J. Du, L. Zong, S. Zhang, Y. Gao, L. Dou, J. Pan, T. Shao, Plasma Process. Polym. 19 (2022) 2100111. https://doi.org/10.1002/ppap.202100111.

[113] K. van ‘t Veer, F. Reniers, A. Bogaerts, Plasma Sources Sci. Technol. 29 (2020) 045020. https://doi.org/10.1088/1361-6595/ab7a8a.

[114] H.A. Eshtehardi, K. Van ‘t Veer, M.-P. Delplancke, F. Reniers, A. Bogaerts, ACS Sustain. Chem. Eng. 11 (2023) 1720–1733. https://doi.org/10.1021/acssuschemeng.2c05665.

[115] N. Pourali, M. Vasilev, R. Abiev, E. V. Rebrov, J. Phys. D: Appl. Phys. 55 (2022) 395204. https://doi.org/10.1088/1361-6463/ac7fc6.

[116] N.E. Afonina, V.G. Gromov, V.L. Kovalev, Fluid Dyn. 37 (2002) 117–125.

[117] V. Guerra, IEEE Trans. Plasma Sci. 35 (2007) 1397–1412. https://doi.org/10.1109/TPS.2007.902028.

[118] Y.C. Kim, M. Boudart, Langmuir. 7 (1991) 2999–3005. https://doi.org/10.1021/la00060a016.

[119] A. Bogaerts, G. Centi, Front. Energy Res. 8 (2020) 1–23. https://doi.org/10.3389/fenrg.2020.00111.

Supporting Information

Is a catalyst always beneficial in plasma catalysis?

Insights from the many physical and chemical interactions

Table of contents

S1. Computational set-up of the DFT calculations

The microkinetic models, of which the results are presented in the main paper, require activation barriers and rate coefficients to calculate the rates of the corresponding reactions. For reactions occurring on the catalyst surface, the activation barriers are obtained from scaling relations (see section S2) and the corresponding rate coefficients are calculated from these barriers using transition state theory (see section S3). The scaling relations, which are used to calculate the activation barriers, are in turn derived from surface species energies calculated with density functional theory (DFT). Most of the surface species energies used to construct the scaling relations are taken from Schumann *et al*. [1] However, some additional species required in our DRM chemistry set, were not included in that paper, and are therefore calculated by ourselves with DFT, using settings that match those of Schumann *et al*. [1] as closely as possible, for consistency reasons. A list of these species with their corresponding energies and frequencies can be found in Table S1. Note that for gas-phase species (listed in

Table S2) the energies and frequencies are not calculated using DFT, but taken from the NIST chemistry webbook [2]. The computational details of our DFT calculations are discussed below.

Periodic plane-wave DFT calculations are carried out using the Vienna Ab-initio simulation Package (VASP version 6.2.1) [3–8]. We use the exchange-correlation functional BEEF-vdW (van der Waals corrected Bayesian error estimation functional) [9,10]. The core electrons are described by the projector augmented wave (PAW) method [11,12]. A plane-wave kinetic energy cutoff of 400 eV is used for the plane-wave basis set and the energy is converged within 10^{-7} eV. A Γ-centered 4×4×1 *k*-point mesh is used. Initial geometries of the adsorbed species are taken from the work of Schumann *et al.* [1] (i.e., a four-layer (3x3) fcc (111) slab with the top two layers allowed to move) as the DFT calculations are used to supplement their dataset. These geometries are relaxed with our computational setup to obtain total energies that can be used for the calculation of reaction and activation energies. Relaxing the geometries of the adsorbed species again (and not taking the optimized geometries from Schumann *et al.* [1]) is necessary because our computational setup is not completely identical to that work. Transition states are obtained using the dimer method, as implemented in the VASP Transition State Tools (VTST) [13–16] package, and are confirmed to be first order saddle points, as only one imaginary frequency is found in the normal mode analysis. The force on each atom is converged within 0.01 eV/Å.

S2. Surface kinetics simulations using the CatMAP code

The surface kinetics simulations (discussed in section 4.6 of the main paper) are performed with the mean-field microkinetic modelling software CatMAP, developed by Medford *et al* [17]. The software calculates reaction rates and fractional coverages at steady state for surfaces exposed to a fixed gas mixture. Specifically, the change in fractional surface coverage θ_s as a function of time, for species s on the catalyst surface is expressed as [17]:

$$\frac{\partial \theta_s}{\partial t} = \sum_{s,cat} \left[(c_{s,i}^R - c_{s,i}^L) r_{i,net} \right] = 0 \qquad \text{(S1)}$$

which equals zero at steady state. In eq. (S1), $c^R_{s,i}$ and $c^L_{s,i}$ are the stoichiometry coefficients of species s in reaction i for the right-hand (production) and left-hand side (destruction), respectively, and $r_{i,net}$ corresponds to the net rate of reaction i. The net rates are calculated from the fractional coverages, $\theta_{s,cat}$, for surface species, and from the partial pressure, $p_{s,cat}$, (which are kept constant) for gas species [17]:

$$r_{i,net} = k_i^f \prod_{s,cat} (\theta_s)^{c_{s,i}^L} \prod_{s,gas} (p_s)^{c_{s,i}^L} - k_i^r \prod_{s,cat} (\theta_s)^{c_{s,i}^R} \prod_{s,gas} (p_s)^{c_{s,i}^R} \qquad \text{(S2)}$$

in which k_i^f and k_i^r correspond to the forward and reverse rate constants, respectively. For more information on CatMAP, we refer to ref. [17].

While this model does not consider any changes in the gas composition due to e.g., gas or surface reactions, it allows to clearly illustrate trends in reactivity between different transition metals. These so-called activity plots display, for example, the production or destruction rates of a specific gas species as function of two descriptors. The descriptors are variables on which other parameters in the model, in this case the adsorbate and transition state energies, are dependent [17]. The use of these descriptors is made possible due to the existence of scaling relations, i.e., correlations between the adsorption energies of surface species and those of specific descriptor adsorbates [18,19]. In our simulations the O* and CH* binding energies are used as descriptors. The binding energies are defined as the formation energies of adsorbed O* and CH* relative to the empty slab and gaseous CO, H_2O and H_2. Note that, as long as the descriptors correlate well with the energies of the other surface species that bind to the catalyst via the O or C atom, the choice of the descriptors does not notably affect the results. The scaling relations used in our simulations are listed in Table S3, and are constructed using the adsorbate and transition state energies on transition metal (111) facets calculated by Schumann *et al* [1]. However, the energies of some surface species required in our simulations for CH_4/CO_2 were not included in that work and are thus calculated by ourselves, as described in section S1.

The simulations are executed at a temperature of 500 K and a total gas pressure of 1 bar, as these conditions are typical for DBD plasma. We employ the approximation that H* adsorbs on a separate reservoir site, as it is assumed to have negligible interactions with the other adsorbates because of its

small size [1,20]. As such H* can still co-adsorb even if the sites on which the larger species bind are fully covered. The Gibbs free energies of gas species are corrected using the Shomate equations. For gas species of which the Shomate parameters are not included in CatMAP by default, the parameters are taken from the NIST chemistry webbook [2]. The free energies of the surface species were corrected using the harmonic limit as implemented in the "Atomic Simulation Environment" (ASE) Python library [21]. The effect of radicals and stable plasma-produced species is investigated by setting small densities of these species in the gas mixture. If a radical is not included in the gas-phase, its adsorption and desorption reactions are removed from the chemistry set, to avoid net radical desorption from the surface due to the zero adsorption rate.

S3. Coupled plasma and surface kinetics simulations

Plasmas have a very rich gas-phase chemistry as a result of electron impact reactions, generating highly reactive species that subsequently react with each other or with stable gas molecules. As such, the plasma chemistry has a strong influence on the gas composition, and thus also on the surface chemistry of a catalyst in contact with this gas mixture. In turn, the destruction and formation of gas species on the catalyst affects the gas composition, and consequently the plasma. Hence, the plasma chemistry alters the surface chemistry and vice versa. Therefore, we developed a coupled plasma and surface kinetics model, which simultaneously calculates the number densities of gas species and fractional coverages of surface species as function of time.

S3.1 Balance equations of the surface and gas species

Our coupled model uses a continuously stirring tank reactor (CSTR) approach, meaning that perfect mixing is assumed in the reactor volume. As such, species densities in the plasma and surface coverages are considered uniform throughout the entire reactor. These densities and coverages change as function of time, as a result of chemical reactions, and due to reactants entering and products leaving the reactor.

The densities of the gas species are described by a balance equation:

$$\frac{\partial n_s}{\partial t} = R_{reaction,s} + \frac{n_{s,in} v_{in}}{V_{CSTR}} + \frac{n_{s,out} v_{out}}{V_{CSTR}} \tag{S3}$$

where n_s is the number density of species s, and t is the operating time. The first term on the right-hand side, $R_{reaction,s}$, denotes the change in number density due to reactions which is calculated according to eq. (S4), the second term corresponds to the feed gas entering the reactor and the third corresponds to the reaction mixture leaving the reactor. Here, $n_{s,in}$ is the species density in the feed, which is equal to 7.24×10^{18} cm^{-3} for CH_4 and CO_2, and zero for all other gas species, i.e., corresponding to a 1:1 CH_4/CO_2 gas mixture at 500 K and 1 bar. The volumetric flow rate entering the reactor, v_{in}, is chosen as 1.79 cm^3/s (corresponding to 107.4 mL/min for a typical DBD reactor), and the gas volume in the reactor, V_{CSTR}, is set equal to 8.85 cm^3. The gas mixture leaving the reactor, $n_{s,out}$, has the same composition as that in the reactor, $n_{s,out} = n_s$, and has a volumetric flow rate, v_{out}, which is calculated so that the total pressure in the reactor remains constant at 1 bar (10^5 Pa), as is shown below in eq. (S5).

The change in the number density of species s, as a result of reactions, is calculated by:

$$R_{reaction,s} = \sum_{i,gas} \left[(c_{s,i}^R - c_{s,i}^L) r_i\right] + n_{sites} f_{cat} \sum_{i,cat} \left[(c_{s,i}^R - c_{s,i}^L) r_i\right] + n_{sites}(1 - f_{cat}) \sum_{i,wall} \left[(c_{s,i}^R - c_{s,i}^L) r_i\right] \tag{S4}$$

Here, the first term on the right-hand side corresponds to the change due to reactions in the gas-phase, the second due to reactions on the catalyst surface, and the third due to interaction with a "non-catalytic"

wall. The latter can be, for example, the surface of the dielectric reactor wall or a dielectric packing. In eq. (S4), $c^R_{s,i}$ and $c^L_{s,i}$ correspond to the stoichiometry coefficients of species s in reaction i for production and destruction, respectively (which are at the right-hand side (R) and left-hand side (L) of the reaction equations, respectively). The reaction rates r_i are expressed in $cm^{-3}\ s^{-1}$ for gas reactions or s^{-1} for surface (catalyst or wall) reactions. The latter are therefore converted to the corresponding change in number density per unit of time (units of $cm^{-3}\ s^{-1}$) by multiplying with their volumetric site density. The number of catalytic sites per unit of gas volume is expressed as $n_{sites} \times f_{cat}$, where n_{sites} is the total volumetric site density of all (catalytic and wall) sites combined and f_{cat} is the fraction of these sites that are catalytic, i.e., transition metal sites. In our model, an estimated value of $1.5 \times 10^{18}\ cm^{-3}$ is used for n_{sites}, and the fraction of catalytic sites is set to 0.5 if a transition metal is present, or zero if this is not the case. As a reference, in ref. [22] de number of catalytic (metal) sites per mass of catalyst material was determined using CO pulse chemisorption for 5 wt.% transition metal catalysts on γ-Al_2O_3, and the measured values varied between 5-30 µmol/g (3-18 $\times 10^{18}$ sites/g). From our own observations we know that a DBD reactor with total (empty) volume of 17.7 cm^3 can hold about 12 g of γ-Al_2O_3-based catalyst pellets and that about half of the total volume of the packed reactor is occupied. As such, the gas volume, V_{CSTR}, in the reactor equals $0.5 \times 17.7\ cm^3 = 8.85\ cm^3$, as mentioned above. The parameters above correspond to volumetric site densities of 4-24 $\times 10^{18}\ cm^{-3}$. In our model, we use $n_{sites} = 1.5 \times 10^{18}\ cm^{-3}$, corresponding to a volumetric catalyst site density of $7.5 \times 10^{17}\ cm^{-3}$ for $f_{cat} = 0.5$. This is a factor 5.3 to 32 lower than aforementioned values, as we assume a smaller metal loading, i.e. 1 wt.% rather than 5 wt.%, and we use the lower end of the range to avoid overestimation of the effect of the catalyst. Indeed, we expect the effect of the catalyst to be slightly overestimated in our model, as we assume perfect mixing, while this is probably not true in reality, due to the short lifetime of the radicals, which might have reacted away before they are well mixed with the other gas species.

The volumetric flow rate of gas leaving the reactor, v_{out}, in eq. (S3) is calculated in such a way that the total pressure (and gas density) remains constant:

$$v_{out} = v_{in} + \frac{V_{CSTR} \sum_{s,gas} R_{reaction,s}}{\sum_{s,gas} n_s} = v_{in} + \frac{V_{CSTR} k_b T}{p_{tot}} \sum_{s,gas} R_{reaction,s} \qquad \text{(S5)}$$

As such, the volumetric flow rate that leaves the reactor, v_{out}, is equal to the sum of the volumetric flow rate entering the reactor, and the change in volume that results from the reactions under the chosen conditions of pressure and temperature. In eq. (S5), p_{tot} is the total pressure in the reactor, k_b is the Boltzmann constant and T is the temperature. Note that for simplicity the temperature of the gas, the catalyst surface and the wall are all assumed equal to 500 K, hence possible hotspots at the catalytic surface are neglected at this stage.

The fractional coverages and empty site fractions on the catalyst surface and wall are described by the following balance equations:

$$\frac{\partial \theta_{s,cat}}{\partial t} = \sum_{i,cat} \left[(c_{s,i}^{R} - c_{s,i}^{L}) r_i \right] \quad \text{(S6)}$$

$$\frac{\partial \theta_{s,wall}}{\partial t} = \sum_{i,wall} \left[(c_{s,i}^{R} - c_{s,i}^{L}) r_i \right] \quad \text{(S7)}$$

Like the simulations with CatMAP, we employ the approximation that H* binds on a separate site type, as explained in section S2. The catalytic sites are equally distributed between normal and H reservoir sites. Also on the non-catalytic wall, two types of sites are present, namely weakly binding physisorption and strongly binding chemisorption sites. Here, we choose a fraction of 2×10^{-3} for chemisorption and 0.998 for physisorption sites on the wall, based on refs. [23,24].

S3.2 Reaction rates

The reaction rates used in eq. (S4), (S6) and (S7) are calculated using the following equation:

$$r_i = k_i \prod_s (a_s)^{c_{s,i}^{L}} \quad \text{(S8)}$$

Here k_i is the reaction rate coefficient and a_s is the activity of species s, which is equal to the number density, n_s, for species in gas-phase reactions, and to the partial pressure, p_s, for gas species in surface reactions, or the fractional coverage, θ_s, for surface species. Number densities are converted to partial pressures and vice versa using the ideal gas law.

S3.3 Rate coefficients of gas-phase reactions

An overview of all gas and surface species in the model can be found in Table S4. Note that we do not include any vibrationally excited molecules, as their effect is negligible compared to that of radicals at the low temperatures that are typical for a DBD reactor (~ 500 K), as discussed in section 4.3 of the main paper. The rate coefficients, k_i, of the gas-phase reactions (with exception of electron impact reactions) are taken from literature and are listed in Table S5, together with the corresponding references. The rate coefficients of electron impact reactions are calculated as described in section S3.4.

S3.4 Rate coefficients of electron impact reactions

While electrons are not explicitly included as a gas-phase species, we obviously do include electron impact dissociation reactions as a way of generating radicals. The rate coefficients of these electron impact reactions are kept constant throughout the simulation. We note that this is a clear approximation for DBD plasmas, which typically consist of microdischarges and are hence non-uniform in both space and time. However, the goal of this study is to illustrate how the production of radicals and stable intermediates in the gas-phase can affect the surface chemistry and how the surface processes can alter the gas composition. A detailed treatment of the pulsed behavior of a DBD plasma combined with a catalyst is therefore outside the scope of this study, but will be investigated in future work.

The rate coefficients for electron impact processes are estimated as follows. First, we calculated the reduced electric field (E/n) at breakdown in pure CO_2 and CH_4 using the Paschen curves [25,26]:

$$\frac{E}{n_{tot}} = \frac{Bk_bT}{C + \ln(p_{tot}d)} \; with \; C = lnA - ln\left(ln\left(\frac{1}{\gamma} + 1\right)\right) \quad \text{(S9)}$$

Where A and B are experimentally determined parameters, taken from literature [25,26], and d is the size of the discharge gap, assumed here to be 4.5 mm. A value of 0.1 was assumed for the secondary electron emission coefficient γ. Typical values of γ in discharges are in the range of 0.1-0.01 [25,26]. Using γ = 0.01, however, results in a rise of only approximately 10% of the E/n calculated for these conditions. Using the Paschen curves, we find an E/n of 154 and 304 Td, for CH_4 and CO_2, respectively. We use the weighted average of these values, E/n = 229 Td, as a rough estimate of the electric field in the discharge for the 1:1 CH_4/CO_2 feed gas. Next, we calculate the rate coefficients of various electron impact reactions using BOLSIG+, a numerical solver for the Boltzmann equation for electrons [27]. We perform the calculation using a gas mixture containing 48.5% CO_2, 48% CH_4, 1.5% CO, 0.5% C_2H_6, 0.5% H_2O and 1.0% H_2. Small fractions of product species are included, as we also include their electron impact dissociation rate coefficients in the model. Note that the exact CH_4 and CO_2 conversions assumed for this gas mixture, and the corresponding fractions of product species, are not of great importance, as we found that the electron impact rate coefficients, calculated as described in this section, vary very little for different compositions. As such, the rate coefficients are considered constant throughout the simulations and do not change with rising conversion. A list of the electron impact processes included in the BOLSIG+ calculations can be found in Table S6. We assume an electron density of 10^{14} cm^{-3}, which is in the range of typical electron densities in the microdischarge filaments of a DBD [26]. We use this value as we will first calculate the electron impact rate coefficients in the microdischarges, which we will correct afterwards to account for microdischarges only taking up a small fraction of the gas volume, as described below. Apart from the rate coefficients of the electron impact processes, BOLSIG+ also provides the reduced electron mobility, $\mu_e \times n$, as function of E/n. The electron mobility, μ_e, can be related to the reduced electric field through:

$$\frac{E}{n_{tot}} = \frac{1}{n_{tot}}\sqrt{\frac{P}{n_e e \mu_e}} \quad \text{(S10)}$$

with P the power density, n_e the electron density and e the elementary charge. Reorganizing gives an expression for the power density:

$$P = E^2 n_e e \mu_e \quad \text{(S11)}$$

If we assume all power is deposited in the discharges, we can estimate the average combined volume of the microdischarges V_{plasma}, for a plasma power of 65 W. Since only a fraction of the gas molecules in the reactor will be exposed to this power density at a given point in time, we correct the electron impact

rate coefficients by multiplying with a geometrical factor V_{plasma}/V_{CSTR}. In Table S7, we list these corrected rate coefficients multiplied by the assumed electron density ($n_e = 10^{14}$ cm^{-3}).

We acknowledge that calculating the electric field by taking the weighted average of electric fields at breakdown for CH_4 and CO_2 gives only a very crude estimation of E/n. However, we find that if the rate coefficients are calculated according to the procedure described above, their values only vary by a factor 1 to 3 when comparing rate coefficients calculated with E/n = 154 Td (pure CH_4), E/n = 304 Td (pure CO_2) and E/n = 229 Td (weighted average). As such, the uncertainties on these rate coefficients are within the typical range of uncertainty factors for gas-phase reactions in literature [28].

S3.5 Rate coefficients of reactions on the catalyst surface

The catalyst surface reactions included in the model are listed in Table S8. The rate coefficients of these reactions are calculated using transition state theory:

$$k = \frac{k_b T}{h} \exp\left(-\frac{\Delta G^{\ddagger}}{RT}\right) = \frac{k_b T}{h} \exp\left(-\frac{\Delta \mathrm{H}^{\ddagger}}{RT}\right) \exp\left(\frac{\Delta \mathrm{S}^{\ddagger}}{R}\right) \quad \text{(S12)}$$

In which h is Planck's constant, R is the ideal gas constant and $\Delta G^{\ddagger}$, $\Delta H^{\ddagger}$ and $\Delta S^{\ddagger}$ are the differences in Gibbs free energy, enthalpy, and entropy, respectively, between the transition state and the initial state. The enthalpy differences are calculated from the species energies acquired from the scaling relations in Table S3. The thermodynamic corrections on the enthalpies and entropies are calculated using the Shomate equations for gas species and the harmonic approximation for surface species, as is also the case for the CatMAP code, discussed in section S2. Note that the rate coefficients calculated with eq. (S12) are expressed in s^{-1}. Specifically for these rate coefficients, the partial pressures used in the calculation of the reaction rates (eq. (S8)) need to be expressed relative to the standard state pressure of the gas (1 bar).

The rate coefficients for adsorption reactions are limited by the gas kinetics multiplied by a sticking coefficient that is function of the activation enthalpy:

$$k_{ads} = \frac{A_s}{\sqrt{2\pi m k_b T}} \exp\left(-\frac{\Delta \mathrm{H}^{\ddagger}}{RT}\right) \quad \text{(S13)}$$

Here A_s is the surface area of a single site, which is chosen as 10^{-15} cm^2 (corresponding to a typical site density of 10^{15} cm^{-2}) [29], and m is the molecular mass of the gas species. Note that if $\Delta H^{\ddagger}$ is zero, the sticking coefficient becomes one and the rate coefficient is determined entirely by the frequency of gas molecules hitting free sites on the surface. In the cases where the adsorption rate coefficient is determined by eq. (S13), the desorption rate coefficients are corrected using the equilibrium constant K_{eq}, to ensure thermodynamic consistency.

$$k_{des} = k_{ads}/K_{eq} \quad \text{(S14)}$$

The equilibrium constant, K_{eq}, is calculated as:

$$K_{eq} = \exp\left(-\frac{\Delta G_{ads}}{RT}\right) = \exp\left(-\frac{\Delta H_{ads}}{RT}\right)\exp\left(\frac{\Delta S_{ads}}{R}\right) \quad \text{(S15)}$$

with ΔG_{ads}, ΔH_{ads} and ΔS_{ads} the reaction Gibbs free energy, enthalpy, and entropy, respectively, for adsorption. For all catalyst surface reactions, the Gibbs free reaction energy, ΔG, is calculated as the difference between the Gibbs free energies, G_s, of the products and reactants:

$$\Delta G = \sum_{\substack{s,\\ Products}} G_s - \sum_{\substack{s,\\ Reactants}} G_s \quad \text{(S16)}$$

The Gibbs free activation barrier, $\Delta G^{\ddagger}$, is calculated as the difference between the Gibbs free energies of the transition state (TS) and the reactants, while also considering that the barrier cannot be negative or smaller than the reaction energy:

$$\Delta G^{\ddagger} = \max\left(\left(\sum_{\substack{s,\\ TS}} G_s - \sum_{\substack{s,\\ Reactants}} G_s\right), \Delta G, 0\right) \quad \text{(S17)}$$

in which 'max' denotes the maximum of the three values.

Apart from reactions on the catalyst surface, our model also includes radical loss processes on a non-catalytic surface, like the reactor wall. The rate coefficients for these reactions are calculated as described in section S3.6.

S3.6 Rate coefficients of reactions on the walls

Apart from reactions on the surface of a transition metal catalyst, our model also includes radical recombination on a non-catalytic surface or the reactor walls. This way, radical loss processes on a surface are also included when no catalyst is present in the reactor. Six different types of reactions are included in the surface mechanism [24]. Radicals from the gas-phase can either reversibly adsorb on physisorption sites or irreversibly on chemisorption sites. Physisorbed species can either desorb back to the gas-phase, diffuse to an empty chemisorption site, or diffuse to an occupied chemisorption site and react via a Langmuir-Hinshelwood (L-H) mechanism. Additionally, Eley-Rideal (E-R) reactions, in which a gas species reacts with a chemisorbed species, are also possible [24]. A full list of all wall reactions in the model can be found in Table S9.

The rate coefficients of adsorption for both chemisorption and physisorption are described by the gas kinetics:

$$k = \frac{A_s}{\sqrt{2\pi m k_b T}} \quad \text{(S18)}$$

The site area, A_s, is considered to be the same for both chemisorption and physisorption sites and is chosen equal to 10^{-15} cm^2. This corresponds to a surface site density of 10^{15} cm^{-2} if the surface is entirely covered with sites. Typical surface site densities are in the range of 10^{15}-10^{16} cm^{-2} [24]. The rate coefficient for desorption from physisorption sites is given by [24]:

$$k = \nu_d \exp\left(-\frac{E_d}{RT}\right) \tag{S19}$$

Here ν_d is the frequency factor for vibration of the physisorbed species in the direction perpendicular to the surface, and is set equal to 10^{15} s^{-1} based on ref. [24]. E_d is the activation energy for desorption. In ref. [23], a value of 51 kJ/mol is reported for E_d of O* and N* on silica, and 37 kJ/mol for that of H*. In our model we assume E_d = 50 kJ/mol for all species, except H* for which we use 40 kJ/mol.

Rate constants for E-R reactions between chemisorbed and gas species are calculated using the following equation [24]:

$$k = \frac{A_s}{\sqrt{2\pi m k_b T}} \exp\left(-\frac{E_r}{RT}\right) \tag{S20}$$

with E_r the activation barrier for recombination. Typical values of E_r for recombination of O or N are in the range of 14-24 kJ/mol [24]. While recombination reactions in our model occur between other species, we assume a similar value of 20 kJ/mol for E_r if recombination results in the formation of a stable gas molecule. We also consider some reactions, however, where species recombine on the wall to form a radical. In this case we assume the newly formed radical remains bound to the surface and set E_r to zero. The rate coefficient for diffusion is given by [24,30]:

$$k = \frac{\nu_D}{4} \exp\left(-\frac{E_D}{RT}\right) \tag{S21}$$

In this expression, ν_D is the frequency of vibration of the physisorbed species parallel to the surface, which is set equal to 10^{13} s^{-1} [23,24,30]. E_D is the energy barrier for diffusion to an adjacent site and is estimated as $E_D = E_d/2$, in accordance with [23,24]. Finally, the rate coefficient for L-H reactions is calculated using:

$$k = \frac{\nu_D}{4} \exp\left(-\frac{E_D + E_r}{RT}\right) = \frac{\nu_D}{4} \exp\left(-\frac{E_D}{RT}\right) \exp\left(-\frac{E_r}{RT}\right) \tag{S22}$$

The barrier for recombination, E_r, is taken the same as for the corresponding E-R process [24]. As such, we use E_r = 20 kJ/mol in case recombination results in a stable gas molecule, or zero if a radical is formed, which is assumed to remain bound to the surface.

S4. Evolution of radicals with operating time

Fig. S1 illustrates the evolution of the H, CH_3, O and OH radical densities in the plasma following the start of the reaction process. We call this "operating time", to make clear that this is not the residence time of the gas in the plasma. The latter is determined by the gas flow rate and length of the plasma in the reactor, while the operating time is the time as function of which the gas densities and surface coverages change, as discussed in section S3.1. This corresponds to the time that evolves following the start of an experiment, i.e. after turning on the plasma and gas flow. Our current model does not yet consider the filamentary character of a DBD, i.e., occurrence of microdischarge pulses that cause temporal and spatial nonuniformities. Nevertheless, the time evolution of the radicals can still provide useful insight in the interactions between the plasma species and the catalyst, both at short and long timescales. Note that both the horizontal and vertical axes in Fig. S1 are logarithmically scaled.

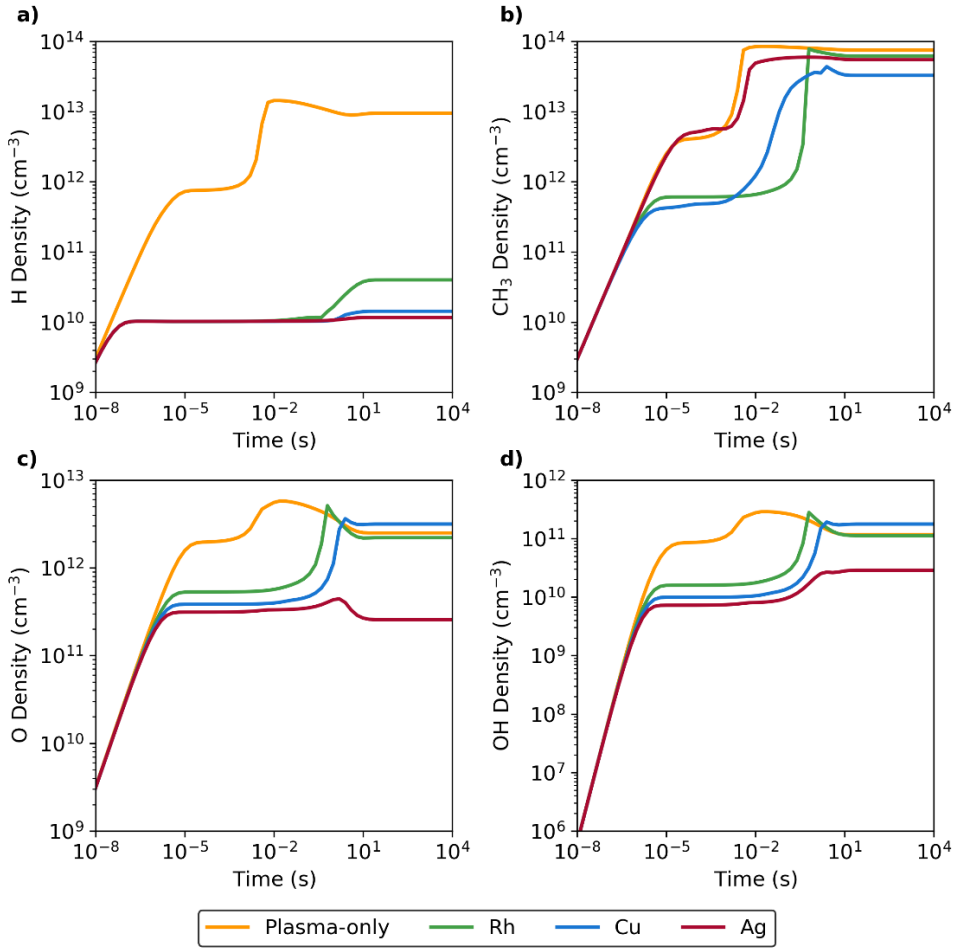

Fig. S1. *Evolution of the (a) H, (b) CH_3, (c) O and (d) OH radical densities with operating time for four different cases, i.e., plasma without catalyst, and plasma combined with a Rh, Cu or Ag catalyst. Calculated for a total pressure of 1 bar and a temperature of 500K.*

Initially, the radical densities clearly increase for all cases, due to electron impact dissociation of the reactant molecules (for the formation of H, CH_3 and O) and subsequent gas-phase reactions (in which also OH is formed). At this timescale, the radical densities are not yet affected by the presence of a transition metal surface and the density curves overlap. At longer timescales, the effect of radical adsorption on the catalyst surface becomes relevant. As a result, the radical densities for the cases without and with different catalysts start to deviate. This occurs between 10^{-8}-10^{-7} s for H radicals (Fig. S1 a)) and around 10^{-6} s for CH_3, O and OH radicals (Fig. S1 b), c) and d), respectively). For the cases with transition metals, most of the radical densities in Fig. S1 show a temporary region of stability. During this period, radical production is partly compensated for by adsorption of radicals on the transition metal surface. As a consequence, the densities of these radicals remain constant as a function of time, and are in general significantly lower when a catalyst is present than in the plasma-only case. However, exceptions also occur, as can be seen in Fig. S1 b) for the CH_3 radicals, when the plasma is combined with Ag. Due to the low adsorption enthalpy of CH_3 on Ag, the density curve for this radical is quite similar to that of the plasma without catalyst. Note that for the plasma-only case, radicals can still recombine on a "non-catalytic" surface, which represents the surface of the reactor wall or a silica packing. However, due to the low densities of chemisorption sites on such a surface and the facile desorption of species from physisorption sites, the rates of radical recombination are typically much lower on the wall compared to on a transition metal surface. Still, exceptions on this do occur when the catalyst is poisoned or for species that bind the transition metal very weakly (like CH_3 on Ag, as explained above).

At timescales of 0.1-1 s, the surfaces of the Cu and Rh catalysts start to become saturated. Due to the drop in the free surface site fractions on these catalysts, less radicals can adsorb on their surfaces and the radical densities in the plasma rise. This is especially visible for CH_3, O and OH in Fig. S1 b), c) and d), respectively, for the cases with Cu and Rh. The rise in CH_3 density starts earlier for the case with Cu, i.e., around 10^{-3}-10^{-2} s. At timescales of 1-10 s, there is again a period of stabilization, and the system typically reaches steady state between 10^{2}-10^{3} s. Depending on the rates of radical recombination on the catalyst surface, the steady-state radical densities can be lower than those in the plasma without catalyst. This is most clear for the H radical densities displayed in Fig. S1 a). The CH_3 densities in Fig. S1 b) show slightly reduced steady-state values for Rh and Ag, compared to plasma without catalyst, while the drop is more significant for Cu. The O and OH densities, on the other hand, are significantly lowered for the case with Ag, as displayed in Fig. S1 c) and d), respectively. For the cases with Rh and Cu, the O and OH densities at steady state are relatively close to those of plasma without catalyst. Note that in the case of Cu, the O and OH densities are slightly higher compared to the plasma-only case, even though these radicals also adsorb on Cu. The reason for this is unclear, but the effect appears to result from a drop in the densities of many other gas species that would otherwise react with O radicals in the

gas-phase. As OH is primarily formed from reaction between O and CH_4 or C_2H_6 in the plasma, the densities of O and OH are coupled.

For the plasma combined with Rh, the radical densities in Fig. S1 b), c) and d) are quite similar to those of the plasma-only case. This is caused by CO* poisoning of the Rh surface at steady state, resulting in partial deactivation of the catalyst. We found this also to be the case for Pt, Pd and Ir, which are not included in Fig. S1. Note that inclusion of lateral interactions between adsorbed CO* might result in partial re-activation of these catalysts. Such interactions are currently not included in our model, as the effect is outside the scope of this study. However, we do expect the global trends to remain valid, i.e., in which the more strongly binding metals are at least partly deactivated due to more difficult desorption. Also note that H radical adsorption and recombination is not affected by the CO* poisoning of the Rh surface, which is a consequence of the separate adsorption site for H* used in our model. In other words, it results from the assumed negligible interactions between the small H atoms and larger adsorbates. For more information, see section S2.

S5. Tables

S5.1 Surface and gas-phase species energies and frequencies

The surface species energies and vibrational frequencies calculated by DFT in our work are listed in Table S1; for the energies and frequencies of other surface species used in the models, we refer to ref. [1]. The adsorbate and transition state energies are given relative to the empty (111) slab and CO, H_2O and H_2 in the gas-phase. In accordance with ref. [1], we use 12 cm^{-1} as a lower limit for the vibrational frequencies and smaller frequencies are replaced with this value. The energies and vibrational frequencies of gas species are listed in Table S2. These energies are not calculated with DFT, but instead we use the experimental enthalpies of formation, which are taken from the NIST chemistry webbook [2]. The zero-point energy (ZPE) and thermodynamic contribution are subtracted from these enthalpies of formation to give the "uncorrected" enthalpies at 0 K. The thermodynamic contribution is estimated from the heat capacity as $c_p(300\ K) \times 300\ K$, with $c_p(300\ K)$ the heat capacity at 300 K [31]. The acquired energies are subsequently recalculated as the formation enthalpies relative to gaseous CO, H_2O and H_2. Note that the energies in Table S2 are only given without the ZPE and thermodynamic contributions, as the "uncorrected" energies are required as input for CatMAP. However, in both CatMAP and our coupled plasma-surface model, the ZPE and thermodynamic contributions are added again to these "uncorrected" energies during the simulations. The vibrational frequencies of the gas species are taken from ref. [32].

Table S1. Energies and vibrational frequencies of surface species on various transition metal (111) surfaces. The energies are calculated as the formation energy of the surface species relative to the empty (111) slab and CO, H_2O and H_2 in the gas-phase.

Species [a]	**Surface**	**Energy (eV)**	**Vibrational frequencies (cm^{-1})** [b]
O^{*s}	Rh	0.42	314.0, 314.0, 461.0
O^{*s}	Ag	1.98	-
O^{*s}	Cu	0.89	-
O^{*s}	Pd	1.01	-
O^{*s}	Pt	1.29	-
O^{*s}	Ir	0.73	-
CO_2^{*s}	Rh	-0.85	12.0, 12.0, 12.0, 37.0, 45.0, 610.0, 620.0, 1311.0, 2343.0
CO_2^{*s}	Ag	-0.82	-
CO_2^{*s}	Cu	-0.83	-
CO_2^{*s}	Pd	-0.84	-
CO_2^{*s}	Pt	-0.85	-
CO_2^{*s}	Ir	-0.85	-
$O\text{-}CO^{*s}$	Rh	0.14	55.0, 117.0, 257.0, 274.0, 383.0, 432.0, 564.0, 1889
$O\text{-}CO^{*s}$	Ag	2.12	-
$O\text{-}CO^{*s}$	Cu	1.02	-
$O\text{-}CO^{*s}$	Pd	0.92	-
$O\text{-}CO^{*s}$	Pt	1.06	-
$O\text{-}CO^{*s}$	Ir	0.13	-
$H\text{-}H^{*h}$	Rh	0.03	85.0, 204.0, 311.0, 1767.0, 1932.0
$H\text{-}H^{*h}$	Ag	1.83	-
$H\text{-}H^{*h}$	Cu	0.98	-
$H\text{-}H^{*h}$	Pd	0.14	-
$H\text{-}H^{*h}$	Pt	0.25	-
$H\text{-}H^{*h}$	Ir	0.11	-
$O\text{-}H^{*s}$	Rh	1.42	111.0, 270.0, 423.0, 459.0, 938.0
$O\text{-}H^{*s}$	Ag	3.22	-
$O\text{-}H^{*s}$	Cu	2.03	-
$O\text{-}H^{*s}$	Pd	1.87	-
$O\text{-}H^{*s}$	Pt	2.11	-
$O\text{-}H^{*s}$	Ir	1.85	-

a) Species containing a hyphen (-) denote transition states.

b) The vibrational frequencies of the species on Rh are used for all descriptor values.

Table S2. Gas-phase species energies and vibrational frequencies.

Species	**Energy (eV)**	**Vibrational frequencies (cm^{-1})**
H_2	0.00	4401.2
H_2O	0.00	3657.0, 1595.0, 3756.0
CH_4	-2.77	2917.0, 1534.0, 1534.0, 3019.0, 3019.0, 3019.0, 1306.0, 1306.0, 1306.0
CO	0.00	2169.8
CO_2	-0.33	1333.0, 2349.0, 667.0, 667.0
CH_2O	-0.28	2782.0, 1746.0, 1500.0, 1167.0, 2843.0, 1249.0
CH_3OH	-1.51	3681.0, 3000.0, 2844.0, 1477.0, 1455.0, 1345.0, 1060.0, 1033.0, 2960.0, 1477.0, 1165.0, 200.0
CH_3CHO	-2.74	3014.0, 2923.0, 2716.0, 1743.0, 1433.0, 1395.0, 1352.0, 1114.0, 867.0, 509.0, 2964.0, 1431.0, 1102.0, 764.0, 150.0
CH_3CH_2OH	-3.71	3652.9, 2984.1, 2939.2, 2899.6, 1490.2, 1463.5, 1411.7, 1371.4, 1256.3, 1090.7, 1027.7, 887.6, 416.5, 2991.4, 2909.6, 1445.8, 1274.8, 1161.0, 811.8, 251.0, 200.0
O	5.32	-
H	2.38	-
CH_3	-0.29	3004.4, 606.5, 3160.8, 3160.8, 1396.0, 1396.0
CH_2	2.39	2805.9, 963.1, 3190.0
OH	3.07	3737.8
CHO	1.56	2434.5, 1868.2, 1080.8

S5.2 Scaling relations

Table S3. Scaling relations that describe the surface species binding energies as function of the binding energies of CH and O* (E_{CH*} and E_{O*}, respectively). All energies are expressed in eV. The binding energies are defined as the formation energies of the adsorbed species relative to the empty (111) slab and CO, H_2O and H_2 in the gas-phase.*

Surface species	**Scaling relation for surface species energy (eV)**
H^{*h}	$0.2157 \times E_{CH*} + 0.0208$
CH_2CO^{*s}	$0.3840 \times E_{CH*} - 2.0507$
CH_2OH^{*s}	$0.4036 \times E_{CH*} - 0.7973$
CH_2O^{*s}	$0.0299 \times E_{CH*} + 0.1287 \times E_{O*} - 0.8431$
CH_2^{*s}	$0.5987 \times E_{CH*} - 0.6190$
$CH_3CH_2OH^{*s}$	$0.0953 \times E_{O*} - 4.247$
CH_3CHOH^{*s}	$0.3899 \times E_{CH*} - 3.0096$
CH_3CHO^{*s}	$0.1068 \times E_{O*} - 3.2775$
CH_3CO^{*s}	$0.4514 \times E_{CH*} - 2.7583$
CH_3O^{*s}	$0.3151 \times E_{O*} - 1.5419$
CH_3^{*s}	$0.2981 \times E_{CH*} - 1.7338$
$CHCO^{*s}$	$0.4047 \times E_{CH*} - 1.6985$
$CHOH^{*s}$	$0.62583 \times E_{CH*} - 0.0469$
CHO^{*s}	$0.4721 \times E_{CH*} - 0.1194$
CH^{*s}	E_{CH*}
CO_2^{*s}	$0.0086 \times E_{CH*} - 0.8335$
CO^{*s}	$0.5075 \times E_{CH*} - 0.8177$
OH^{*s}	$0.3089 \times E_{O*} + 0.2447$
O^{*s}	E_{O*}
$H\text{-}H^{*h}$	$0.4627 \times E_{CH*} + 0.9053$
$CH\text{-}CO^{*s}$	$1.0504 \times E_{CH*} - 0.0304$

CH-H*^{s}	$1.1198 \times E_{CH^*} + 0.5586$
CH-OH*^{s}	$0.8717 \times E_{CH^*} + 0.2692 \times E_{O^*} + 0.9914$
CH_2-H*^{s}	$0.7830 \times E_{CH^*} - 0.1068$
CH_3-CO*^{s}	$0.4927 \times E_{CH^*} - 1.3135$
CH_3-H*^{s}	$0.4721 \times E_{CH^*} - 1.1043$
CH_3-OH*^{s}	$0.1327 \times E_{CH^*} + 0.1939 \times E_{O^*} + 0.0450$
CH_3CHO-H*^{s}	$0.3742 \times E_{CH^*} + 0.0096 \times E_{O^*} - 2.2066$
CH_3CHOH-H *^{s}	$0.4713 \times E_{CH^*} + 0.0211 \times E_{O^*} - 2.5172$
CH_3O-H*^{s}	$0.1085 \times E_{CH^*} + 0.1585 \times E_{O^*} - 0.5971$
H-CH_2CO*^{s}	$0.4969 \times E_{CH^*} - 1.2740$
H-CH_2OH*^{s}	$0.4492 \times E_{CH^*} - 0.1866$
H-CH_2O*^{s}	$0.1947 \times E_{CH^*} + 0.1673 \times E_{O^*} - 0.3649$
H-CH_3CO*^{s}	$0.4777 \times E_{CH^*} + 0.0303 \times E_{O^*} - 2.1454$
H-CHCO*^{s}	$0.6542 \times E_{CH^*} - 0.8822$
H-CHOH*^{s}	$0.6167 \times E_{CH^*} + 0.6003$
H-CHO*^{s}	$0.4828 \times E_{CH^*} + 0.0401 \times E_{O^*} + 0.2964$
H-CO*^{s}	$0.5341 \times E_{CH^*} + 0.1823$
H-OH*^{s}	$0.1497 \times E_{CH^*} + 0.2144 \times E_{O^*} + 0.9553$
HCO-H*^{s}	$0.6838 \times E_{CH^*} + 0.5385$
O-CO*^{s}	$0.2986 \times E_{CH^*} + 0.5883 \times E_{O^*} + 0.5036$
O-H*^{s}	$0.1603 \times E_{CH^*} + 0.7434 \times E_{O^*} + 1.4210$

S5.3 Species included in the model

Table S4. List of the gas-phase species, wall and catalyst surface species included in the model.

Gas-phase species	H_2, H, H_2O, OH, O, CO_2, CO, CH_4, CH_3, CH_2, C_2H_6, C_2H_5, CHO, CH_2O, CH_3O, CH_3OH, CH_2OH, CH_3CH_2OH, CH_3CHO, CH_3CO
Wall species (physisorbed)[a]	H^{*p}, O^{*p}, CH_3^{*p}, CH_2^{*p}, CHO^{*p}, OH^{*p}, ^{*p}
Wall species (chemisorbed)[a]	H^{*c}, O^{*c}, CH_3^{*c}, CH_2^{*c}, CHO^{*c}, OH^{*c}, ^{*c}
Catalyst surface species [a]	H^{*h}, ^{*h}, O^{*s}, OH^{*s}, CO_2^{*s}, CO^{*s}, CHO^{*s}, $CHOH^{*s}$, CH_2OH^{*s}, CH_2O^{*s}, CH_3O^{*s}, CH^{*s}, CH_2^{*s}, CH_3^{*s}, $CHCO^{*s}$, CH_2CO^{*s}, CH_3CO^{*s}, CH_3CHO^{*s}, CH_3CHOH^{*s}, $CH_3CH_2OH^{*s}$, ^{*s}

a) Superscripts p, c, h and s refer the physisorption, chemisorption, hydrogen reservoir and catalytic surface sites, respectively.

S5.4 Rate coefficients of gas-phase reactions

Table S5 lists the gas-phase reactions and corresponding rate coefficients used in the coupled plasma-surface model, with exception of the electron impact dissociation reactions, which are listed in Table S7 below. Some of the rate coefficients for the dissociation and recombination reactions in Table S5 are given as fall-off expressions of the form [33]:

$$k = \frac{k_0 M k_\infty}{k_0 M + k_\infty} F \tag{S23}$$

$$\log(F) = \frac{\log(F_c)}{1 + \left[\frac{\log(k_0 M / k_\infty)}{N}\right]^2} \tag{S24}$$

$$N = 0.75 - 1.27\log(F_c) \tag{S25}$$

In which k_0 and k_∞ are the low- and high-pressure limit rate coefficients, respectively, F_c is the centered broadening factor and M is the density of neutral gas species, equal to 1.449×10^{19} cm^{-3} at 500 K. Expressions for k_0, k_∞ and F_c are listed in Table S5.

Table S5. List of gas-phase reactions included in the coupled plasma-surface model with the corresponding rate coefficient expressions and references.

Reaction	**Rate coefficient** [a, b]	**Ref.**
$H + OH \rightarrow H_2 + O$	$4.1\times10^{-12}\left(\frac{T}{300}\right)\exp\left(\frac{-3.50\times10^3}{T}\right)$	[34]
$H + OH \rightarrow H_2O$	$6.7\times10^{-31}\left(\frac{T}{300}\right)^{-2.0}\times M$	[34]
$OH + OH \rightarrow H_2O + O$	$1.02\times10^{-12}\left(\frac{T}{300}\right)^{1.4}\exp\left(\frac{2.0\times10^2}{T}\right)$	[28]
$OH \rightarrow O + H$	$4.7\times10^{-8}\left(\frac{T}{300}\right)^{-1.0}\exp\left(\frac{-5.0830\times10^4}{T}\right)\times M$	[34]
$H_2 + OH \rightarrow H + H_2O$	$3.6\times10^{-16}T^{1.52}\exp\left(\frac{-1.74\times10^3}{T}\right)$	[33]
$H_2O + O \rightarrow OH + OH$	$7.6\times10^{-15}T^{1.3}\exp\left(\frac{-8.6\times10^3}{T}\right)$	[28]
$H + H_2O \rightarrow H_2 + OH$	$7.5\times10^{-16}T^{1.6}\exp\left(\frac{-9.03\times10^3}{T}\right)$	[33]
$O + H \rightarrow OH$	$4.33\times10^{-32}\left(\frac{T}{300}\right)^{-1}\times M$	[28]

$H_2 + O \rightarrow H + OH$	$9\times10^{-12}\left(\frac{T}{300}\right)\exp\left(\frac{-4.480\times10^{3}}{T}\right)$	[34]
$H + H \rightarrow H_2$	$1.8\times10^{-30}T^{-1}\times M$	[34]
$CO + O \rightarrow CO_2$	$2.79\times10^{-29}T^{-1.5}\exp\left(\frac{-2.52\times10^{3}}{T}\right)\times M$	[35]
$CH_4 + H \rightarrow CH_3 + H_2$	$6.4\times10^{-18}T^{2.11}\exp\left(\frac{-3.9\times10^{3}}{T}\right)$	[36]
$CH_3 + H_2 \rightarrow CH_4 + H$	$6.62\times10^{-20}T^{2.24}\exp\left(\frac{-3.22\times10^{3}}{T}\right)$	[36]
$CH_3 + H \rightarrow CH_2 + H_2$	$2.1\times10^{-8}T^{-0.56}\exp\left(\frac{-8.0\times10^{3}}{T}\right)$	[33]
$CH_3 + H \rightarrow CH_4$	$k_0 = 1.7\times10^{-24}T^{-1.8}$ $k_\infty = 3.5\times10^{-10}$ $F_c = 6.3\times10^{-1}\exp\left(\frac{-T}{3.3150\times10^{3}}\right)$ $+3.7\times10^{-1}\exp\left(\frac{-T}{6.10\times10^{1}}\right)$	[33] [c]
$CH_2 + H_2 \rightarrow CH_3 + H$	$7.32\times10^{-19}T^{2.3}\exp\left(\frac{-3.6990\times10^{3}}{T}\right)$	[37]
$CH_3 + CH_4 \rightarrow C_2H_6 + H$	$\frac{8\times10^{13}}{N_A}\exp\left(\frac{-1.6736\times10^{5}}{RT}\right)$	[38]
$CH_3 + CH_4 \rightarrow C_2H_5 + H_2$	$\frac{1\times10^{13}}{N_A}\exp\left(\frac{-9.6232\times10^{4}}{RT}\right)$	[38]
$CH_2 + CH_4 \rightarrow CH_3 + CH_3$	$7.14\times10^{-12}\exp\left(\frac{-4.199\times10^{4}}{RT}\right)$	[39]
$CH_3 + CH_3 \rightarrow C_2H_6$	$k_0 = 3.5\times10^{-7}T^{-7}\exp\left(\frac{-1.39\times10^{3}}{T}\right)$ $k_\infty = 6\times10^{-11}$ $F_c = 3.8\times10^{-1}\exp\left(\frac{-T}{7.3\times10^{1}}\right)$ $+6.2\times10^{-1}\exp\left(\frac{-T}{1.18\times10^{3}}\right)$	[33] [c]
$CH_3 + CH_3 \rightarrow C_2H_5 + H$	$9\times10^{-11}\exp\left(\frac{-8.08\times10^{3}}{T}\right)$	[33]
$CH_3 + CH_3 \rightarrow CH_2 + CH_4$	$5.6\times10^{-17}T^{1.34}\exp\left(\frac{-6.791\times10^{4}}{RT}\right)$	[40]

$CH_3 \rightarrow CH_2 + H$	$1.7\times10^{-8}\exp\left(\frac{-4.560\times10^{4}}{T}\right)\times M$	[33]
$C_2H_6 + H \rightarrow C_2H_5 + H_2$	$1.63\times10^{-10}\exp\left(\frac{-4.640\times10^{3}}{T}\right)$	[33]
$C_2H_5 + H_2 \rightarrow C_2H_6 + H$	$5.1\times10^{-24}T^{3.6}\exp\left(\frac{-4.253\times10^{3}}{T}\right)$	[33]
$C_2H_5 + H \rightarrow CH_3 + CH_3$	7×10^{-11}	[33]
$C_2H_5 + H \rightarrow C_2H_6$	$\frac{6\times10^{-11}}{1+10^{-1.915+2.69\times10^{-3}T-2.35\times10^{-7}T^2}}$	[28]
$C_2H_6 + CH_3 \rightarrow C_2H_5 + CH_4$	$9.3\times10^{-14}\exp\left(\frac{-4.740\times10^{3}}{T}\right)$ $+1.4\times10^{-9}\exp\left(\frac{-1.120\times10^{4}}{T}\right)$	[33]
$C_2H_6 + CH_2 \rightarrow C_2H_5 + CH_3$	$\frac{6.5\times10^{12}}{N_A}\exp\left(\frac{-3.31\times10^{4}}{RT}\right)$	[39]
$C_2H_5 + CH_4 \rightarrow C_2H_6 + CH_3$	$1.43\times10^{-25}T^{4.14}\exp\left(\frac{-6.322\times10^{3}}{T}\right)$	[28]
$C_2H_5 + CH_3 \rightarrow C_2H_6 + CH_2$	$3\times10^{-44}T^{9.0956}$	[41]
$CO_2 + H \rightarrow CO + OH$	$4.7\times10^{-10}\exp\left(\frac{-1.3915\times10^{4}}{T}\right)$	[33]
$CO + H \rightarrow CHO$	$2\times10^{-35}T^{0.2}\times M$	[33]
$CO + OH \rightarrow CO_2 + H$	$\frac{3.3\times10^{6}}{N_A}T^{1.55}\exp\left(\frac{4.02\times10^{2}}{T}\right)$	[42]
$CH_4 + O \rightarrow CH_3 + OH$	$7.3\times10^{-19}T^{2.5}\exp\left(\frac{-3.310\times10^{3}}{T}\right)$	[33]
$CH_3 + O \rightarrow H + CH_2O$	$0.8\times1.4\times10^{-10}$	[33]
$CH_3 + O \rightarrow CO + H_2 + H$	$0.2\times1.4\times10^{-10}$	[33]
$CH_2 + O \rightarrow CO + H + H$	$0.6\times3.4\times10^{-10}\exp\left(\frac{-2.7\times10^{2}}{T}\right)$	[33]
$CH_2 + O \rightarrow CO + H_2$	$0.4\times3.4\times10^{-10}\exp\left(\frac{-2.7\times10^{2}}{T}\right)$	[33]
$CH_3 + CO \rightarrow CH_3CO$	$k_0 = 1.6\times10^{-37}T^{1.05}\exp\left(\frac{-1.3\times10^{3}}{T}\right)$ $k_\infty = 3.1\times10^{-16}T^{1.05}\exp\left(\frac{-2.85\times10^{3}}{T}\right)$ $F_c = 5\times10^{-1}$	[33] [c]

$CH_2 + CO_2 \rightarrow CO + CH_2O$	3.9×10^{-14}	[28]
$CH_4 + OH \rightarrow CH_3 + H_2O$	$1.66\times10^{-18}T^{2.182}\exp\left(\frac{-1.231\times10^{3}}{T}\right)$	[43]
$CH_3 + OH \rightarrow CH_3OH$	$k_0 = 1.06\times10^{-10}T^{-6.21}\exp\left(\frac{-6.71\times10^{2}}{T}\right)$ $k_\infty = 7.2\times10^{-9}T^{-0.79}$ $F_c = 7.5\times10^{-1}\exp\left(\frac{-T}{2.1\times10^{2}}\right)$ $+2.5\times10^{-1}\exp\left(\frac{-T}{1.434\times10^{3}}\right)$	[33] [c]
$CH_3 + OH \rightarrow CH_2 + H_2O$	$\frac{k}{M}$ $k_0 = 1.8\times10^{-8}T^{-0.91}\exp\left(\frac{-2.75\times10^{2}}{T}\right)$ $k_\infty = 6.4\times10^{-8}T^{5.8}\exp\left(\frac{4.85\times10^{2}}{T}\right)$ $F_c = 6.64\times10^{-1}\exp\left(\frac{-T}{3.569\times10^{3}}\right)$ $+3.36\times10^{-1}\exp\left(\frac{-T}{1.08\times10^{2}}\right)$ $+\exp\left(\frac{-3.24\times10^{3}}{T}\right)$	[33] [c]
$CH_3 + OH \rightarrow CH_2OH + H$	$1.2\times10^{-12}\exp\left(\frac{-2.76\times10^{3}}{T}\right)$	[33]
$CH_3 + OH \rightarrow CH_3O + H$	$2\times10^{-14}\exp\left(\frac{-6.99\times10^{3}}{T}\right)$	[33]
$CH_3 + OH \rightarrow H_2 + CH_2O$	$5.3\times10^{-15}\exp\left(\frac{-2.53\times10^{3}}{T}\right)$	[33]
$CH_3 + OH \rightarrow CH_4 + O$	$1.16\times10^{-19}T^{2.2}\exp\left(\frac{-2.24\times10^{3}}{T}\right)$	[44]
$CH_3 + H_2O \rightarrow CH_4 + OH$	$8\times10^{-22}T^{2.9}\exp\left(\frac{-7.48\times10^{3}}{T}\right)$	[45]
$CH_2 + OH \rightarrow H + CH_2O$	5×10^{-11}	[28]
$CH_2 + H_2O \rightarrow CH_3 + OH$	1×10^{-16}	[28]
$CH_3O + CO \rightarrow CH_3 + CO_2$	$2.6\times10^{-11}\exp\left(\frac{-5.94\times10^{3}}{T}\right)$	[28]
$H + CHO \rightarrow CO + H_2$	1.5×10^{-10}	[33]

$H + CHO \rightarrow CH_2 + O$	$\frac{3.981\times10^{13}}{N_A}\exp\left(\frac{-4.29\times10^{5}}{RT}\right)$	[46]
$H_2 + CHO \rightarrow H + CH_2O$	$3\times10^{-18}T^{2}\exp\left(\frac{-8.972\times10^{3}}{T}\right)$	[28]
$H + CH_2O \rightarrow H_2 + CHO$	$3.34\times10^{-23}T^{-3.81}\exp\left(\frac{-2.02\times10^{2}}{T}\right)$	[33]
$H + CH_2O \rightarrow CH_3O$	$\frac{2.4\times10^{13}}{N_A}\exp\left(\frac{-1.72\times10^{4}}{T}\right)$	[47]
$CH_3O + H \rightarrow H_2 + CH_2O$	3.3×10^{-11}	[28]
$CH_3O + H \rightarrow CH_3OH$	$3.4\times10^{-10}\left(\frac{T}{300}\right)^{0.33}$	[48]
$CH_3O + H_2 \rightarrow CH_3OH + H$	$1.7\times10^{-15}\left(\frac{T}{300}\right)^{4}\exp\left(\frac{-2.47\times10^{3}}{T}\right)$	[49]
$CH_2OH + H \rightarrow H_2 + CH_2O$	1×10^{-11}	[50]
$CH_2OH + H \rightarrow CH_3 + OH$	1.6×10^{-10}	[50]
$CH_2OH + H_2 \rightarrow CH_3OH + H$	$1.12\times10^{-18}T^{2}\exp\left(\frac{-6.722\times10^{3}}{T}\right)$	[50]
$CH_3OH + H \rightarrow CH_2OH + H_2$	$5.7\times10^{-15}T^{1.24}\exp\left(\frac{-2.26\times10^{3}}{T}\right)$	[33]
$CH_3OH + H \rightarrow CH_3 + H_2O$	1.9×10^{-28}	[51]
$CHO + OH \rightarrow CO + H_2O$	1.8×10^{-10}	[33]
$H_2O + CHO \rightarrow CH_2O + OH$	$3.9\times10^{-16}T^{1.35}\exp\left(\frac{-1.3146\times10^{4}}{T}\right)$	[28]
$CH_2O + OH \rightarrow H_2O + CHO$	$2.31\times10^{-11}\exp\left(\frac{-3.04\times10^{2}}{T}\right)$	[33]
$CH_3O + OH \rightarrow H_2O + CH_2O$	3×10^{-11}	[28]
$CH_2OH + OH \rightarrow H_2O + CH_2O$	4×10^{-11}	[50]
$CH_2OH + H_2O \rightarrow CH_3OH + OH$	$4.2\times10^{-14}\left(\frac{T}{300}\right)^{3.0}\exp\left(\frac{-10440}{T}\right)$	[49]
$CH_3OH + OH \rightarrow H + H_2O + CH_2O$	$2.96\times10^{-16}T^{1.4434}\exp\left(\frac{-5.7\times10^{1}}{T}\right)$	[52]
$CHO + O \rightarrow CO + OH$	5×10^{-11}	[28]
$CHO + O \rightarrow CO_2 + H$	5×10^{-11}	[28]
$CH_2O + O \rightarrow CHO + OH$	$6.9\times10^{-13}T^{0.57}\exp\left(\frac{-1.39\times10^{3}}{T}\right)$	[33]

$CH_3O + O \rightarrow CH_2O + OH$	$0.25\times2.5\times10^{-11}$	[33]
$CH_3OH + O \rightarrow CH_2OH + OH$	$4.1\times10^{-11}\exp\left(\frac{-2.67\times10^{3}}{T}\right)$	[33]
$CH_4 + CHO \rightarrow CH_3 + CH_2O$	$1.21\times10^{-20}T^{2.85}\exp\left(\frac{-1.133\times10^{4}}{T}\right)$	[28]
$CH_3 + CHO \rightarrow CH_4 + CO$	2×10^{-10}	[28]
$CH_3 + CHO \rightarrow CH_3CHO$	3×10^{-11}	[28]
$CH_2 + CHO \rightarrow CH_3 + CO$	3×10^{-11}	[28]
$CH_3 + CH_2O \rightarrow CH_4 + CHO$	$5.3\times10^{-23}T^{3.36}\exp\left(\frac{-2.17\times10^{3}}{T}\right)$	[33]
$CH_2 + CH_2O \rightarrow CH_3 + CHO$	1×10^{-14}	[28]
$CH_3O + CH_4 \rightarrow CH_3 + CH_3OH$	$2.6\times10^{-13}\exp\left(\frac{-4.45\times10^{3}}{T}\right)$	[28]
$CH_3 + CH_3O \rightarrow CH_4 + CH_2O$	4×10^{-11}	[28]
$CH_2 + CH_3O \rightarrow CH_3 + CH_2O$	3×10^{-11}	[28]
$CH_2OH + CH_4 \rightarrow CH_3 + CH_3OH$	$3.6\times10^{-23}T^{3.1}\exp\left(\frac{-8.166\times10^{3}}{T}\right)$	[50]
$CH_2OH + CH_3 \rightarrow CH_3CH_2OH$	2×10^{-11}	[50]
$CH_2OH + CH_3 \rightarrow CH_4 + CH_2O$	4×10^{-12}	[50]
$CH_2 + CH_2OH \rightarrow CH_3 + CH_2O$	2×10^{-12}	[50]
$CH_3 + CH_3OH \rightarrow CH_2OH + CH_4$	$0.33\times5\times10^{-23}T^{3.45}\exp\left(\frac{-4.02\times10^{3}}{T}\right)$	[33]
$CH_3 + CH_3OH \rightarrow CH_3O + CH_4$	$0.67\times5\times10^{-23}T^{3.45}\exp\left(\frac{-4.02\times10^{3}}{T}\right)$	[33]
$CH_2 + CH_3OH \rightarrow CH_2OH + CH_3$	$5.3\times10^{-23}T^{3.2}\exp\left(\frac{-3.609\times10^{3}}{T}\right)$	[50]
$CH_2 + CH_3OH \rightarrow CH_3 + CH_3O$	$2.4\times10^{-23}T^{3.1}\exp\left(\frac{-3.49\times10^{3}}{T}\right)$	[50]
$CHO + CHO \rightarrow CO + CH_2O$	$0.853\times5\times10^{-11}$	[33]
$CHO + CHO \rightarrow CO + CO + H_2$	$0.147\times5\times10^{-11}$	[33]
$CH_3O + CHO \rightarrow CH_3OH + CO$	1.5×10^{-10}	[28]
$CH_2OH + CHO \rightarrow CH_3OH + CO$	2×10^{-10}	[50]
$CH_2OH + CHO \rightarrow CH_2O + CH_2O$	3×10^{-10}	[50]

$CH_3OH + CHO \rightarrow CH_2OH + CH_2O$	$1.6\times10^{-20}T^{2.9}\exp\left(\frac{-6.596\times10^{3}}{T}\right)$	[50]
$CH_3OH + CHO \rightarrow CH_3O + CH_2O$	$1.6\times10^{-22}T^{2.9}\exp\left(\frac{-6.596\times10^{3}}{T}\right)$	[50]
$CH_3O + CH_2O \rightarrow CH_3OH + CHO$	$1.7\times10^{-13}\exp\left(\frac{-1.5\times10^{3}}{T}\right)$	[28]
$CH_2OH + CH_2O \rightarrow CH_3OH + CHO$	$9.1\times10^{-21}T^{2.8}\exp\left(\frac{-2.95\times10^{3}}{T}\right)$	[50]
$CH_3O + CH_3O \rightarrow CH_3OH + CH_2O$	1×10^{-10}	[28]
$CH_2OH + CH_3O \rightarrow CH_3OH + CH_2O$	4×10^{-11}	[50]
$CH_3O + CH_3OH \rightarrow CH_2OH + CH_3OH$	$5\times10^{-13}\exp\left(\frac{-2.05\times10^{3}}{T}\right)$	[50]
$CH_2OH + CH_2OH \rightarrow CH_3OH + CH_2O$	8×10^{-12}	[50]
$CH_2OH + CH_3OH \rightarrow CH_3O + CH_3OH$	$1.3\times10^{-14}\exp\left(\frac{-6.07\times10^{3}}{T}\right)$	[50]
$C_2H_6 + OH \rightarrow C_2H_5 + H_2O$	$1.52\times10^{-17}T^{2}\exp\left(\frac{-5\times10^{2}}{T}\right)$	[33]
$C_2H_5 + OH \rightarrow C_2H_6 + O$	$1.7\times10^{-40}T^{8.8}\exp\left(\frac{-2.5\times10^{2}}{T}\right)$	[44]
$C_2H_5 + H_2O \rightarrow C_2H_6 + OH$	$5.6\times10^{-18}T^{1.44}\exp\left(\frac{-1.015\times10^{4}}{T}\right)$	[28]
$C_2H_6 + O \rightarrow C_2H_5 + OH$	$3\times10^{-19}T^{2.8}\exp\left(\frac{-2.92\times10^{3}}{T}\right)$	[33]
$C_2H_5 + O \rightarrow CH_3CHO + H$	$0.4\times2.2\times10^{-10}$	[33]
$C_2H_5 + O \rightarrow CH_3 + CH_2O$	$0.3\times2.2\times10^{-10}$	[33]
$C_2H_6 + CHO \rightarrow C_2H_5 + CH_2O$	$7.8\times10^{-20}T^{2.72}\exp\left(\frac{-9.176\times10^{3}}{T}\right)$	[28]
$C_2H_6 + CH_3O \rightarrow C_2H_5 + CH_3OH$	$4\times10^{-13}\exp\left(\frac{-3.57\times10^{3}}{T}\right)$	[28]
$C_2H_6 + CH_2OH \rightarrow C_2H_5 + CH_3OH$	$3.3\times10^{-22}T^{2.95}\exp\left(\frac{-7.033\times10^{3}}{T}\right)$	[50]
$C_2H_5 + CHO \rightarrow C_2H_6 + CO$	2×10^{-10}	[28]
$C_2H_5 + CH_2O \rightarrow C_2H_6 + CHO$	$9.2\times10^{-21}T^{2.81}\exp\left(\frac{-2.95\times10^{3}}{T}\right)$	[28]
$C_2H_5 + CH_3O \rightarrow C_2H_6 + CH_2O$	4×10^{-11}	[28]
$C_2H_5 + CH_2OH \rightarrow C_2H_6 + CH_2O$	4×10^{-12}	[50]

$C_2H_5 + CH_3OH \rightarrow C_2H_6 + CH_2OH$	$5.3\times10^{-23}T^{3.2}\exp\left(\frac{-4.61\times10^{3}}{T}\right)$	[50]
$C_2H_5 + CH_3OH \rightarrow C_2H_6 + CH_3O$	$2.4\times10^{-23}T^{3.1}\exp\left(\frac{-4.5\times10^{3}}{T}\right)$	[50]
$CH_3CO + H \rightarrow CH_3 + CHO$	$0.65\times\frac{2\times10^{13}}{N_A}$	[53,54]
$CH_3CO + H \rightarrow CH_3CHO$	$6.02\times10^{-11}T^{0.16}$	[55]
$CH_3CO + H_2 \rightarrow CH_3CHO + H$	$6.8\times10^{-18}T^{1.82}\exp\left(\frac{-8.862\times10^{3}}{T}\right)$	[28]
$CH_3CHO + H \rightarrow CH_3CO + H_2$	$2.18\times10^{-19}T^{2.58}\exp\left(\frac{-6.14\times10^{2}}{T}\right)$	[56]
$CH_3CH_2OH + H \rightarrow C_2H_5 + H_2O$	$\frac{5.9\times10^{11}}{N_A}\exp\left(\frac{-1.44\times10^{4}}{RT}\right)$	[57]
$CH_3CHO + OH \rightarrow CH_3CO + H_2O$	$0.93\times4.8\times10^{-16}T^{1.35}\exp\left(\frac{7.92\times10^{2}}{T}\right)$	[33]
$CH_3CO + O \rightarrow CH_3 + CO_2$	$0.75\times3.5\times10^{-10}$	[33]
$CH_3CHO + O \rightarrow CH_3CO + OH$	$\frac{5\times10^{12}}{N_A}\exp\left(\frac{-7.5\times10^{3}}{RT}\right)$	[53]
$CH_3CO + CH_4 \rightarrow CH_3 + CH_3CHO$	$3.6\times10^{-21}T^{2.88}\exp\left(\frac{-1.08\times10^{4}}{T}\right)$	[28]
$CH_3 + CH_3CHO \rightarrow CH_3CO + CH_4$	$0.993\times5.8\times10^{-32}T^{6.21}\exp\left(\frac{-8.2\times10^{2}}{T}\right)$	[33]
$CH_3 + CH_3CHO \rightarrow CH_3 + CH_4 + CO$	$\frac{6.31\times10^{12}}{N_A}T^{0.5}\exp\left(\frac{-4.48\times10^{4}}{RT}\right)$	[58]
$C_2H_6 + CH_3CO \rightarrow C_2H_5 + CH_3CHO$	$3\times10^{-20}T^{2.75}\exp\left(\frac{-8.82\times10^{3}}{T}\right)$	[28]
$C_2H_5 + CH_3CHO \rightarrow C_2H_6 + CH_3CO$	$\frac{1.26\times10^{12}}{N_A}\exp\left(\frac{-3.56\times10^{4}}{RT}\right)$	[59]
$CH_3CO + CHO \rightarrow CH_3CHO + CO$	1.5×10^{-11}	[28]
$CH_3CO + CH_2O \rightarrow CH_3CHO + CHO$	$3\times10^{-13}\exp\left(\frac{-6.5\times10^{3}}{T}\right)$	[28]
$CH_3CO + CH_3O \rightarrow CH_3CHO + CH_2O$	1×10^{-11}	[28]
$CH_3CO + CH_3OH \rightarrow CH_3CHO + CH_2OH$	$8.06\times10^{-21}T^{2.99}\exp\left(\frac{-6.21\times10^{3}}{T}\right)$	[50]
$CH_3CHO + CH_3O \rightarrow CH_3CO + CH_3OH$	$\frac{1.69\times10^{5}}{N_A}T^{2.04}\exp\left(\frac{-9.84\times10^{3}}{RT}\right)$	[60]

	$+\frac{9.62\times10^{3}}{N_A}T^{2.5}\exp\left(\frac{-6.65\times10^{2}}{RT}\right)$	
CHO → CO + H	$6.6\times10^{-11}\exp\left(\frac{-7.82\times10^{3}}{T}\right)\times M$	[33]
CH_2O → H + CHO	$8.09\times10^{-9}\exp\left(\frac{-3.805\times10^{4}}{T}\right)\times M$	[33]
CH_2O → CO + H_2	$4.7\times10^{-9}\exp\left(\frac{-3.211\times10^{4}}{T}\right)\times M$	[33]
CH_3O → H + CH_2O	$6.8\times10^{13}\exp\left(\frac{-1.317\times10^{4}}{T}\right)$	[33]
CH_2OH → H + CH_2O	$k_0=\frac{6.01\times10^{33}}{N_A}T^{-5.39}\exp\left(\frac{-1.51\times10^{5}}{RT}\right)$ $k_\infty=2.8\times10^{14}T^{-0.73}\exp\left(\frac{-1.37\times10^{5}}{RT}\right)$ $F_c=4\times10^{-2}\exp\left(\frac{-T}{6.76\times10^{1}}\right)$ $+9.6\times10^{-1}\exp\left(\frac{-T}{1.855\times10^{3}}\right)$ $+\exp\left(\frac{-7.543\times10^{3}}{T}\right)$	[61] [c]
CH_3OH → CH_3 + OH	$0.8\times k$ $k_0=1.1\times10^{-7}\exp\left(\frac{-3.308\times10^{4}}{T}\right)$ $k_\infty=2.5\times10^{19}T^{-0.94}\exp\left(\frac{-4.703\times10^{4}}{T}\right)$ $F_c=1.8\times10^{-1}\exp\left(\frac{-T}{2\times10^{2}}\right)$ $+8.2\times10^{-1}\exp\left(\frac{-T}{1.438\times10^{3}}\right)$	[33,62] [c]
CH_3OH → CH_2 + H_2O	$0.15\times k$ $k_0=1.1\times10^{-7}\exp\left(\frac{-3.308\times10^{4}}{T}\right)$ $k_\infty=2.5\times10^{19}T^{-0.94}\exp\left(\frac{-4.703\times10^{4}}{T}\right)$ $F_c=1.8\times10^{-1}\exp\left(\frac{-T}{2\times10^{2}}\right)$ $+8.2\times10^{-1}\exp\left(\frac{-T}{1.438\times10^{3}}\right)$	[33,62] [c]

$CH_3OH \rightarrow CH_2OH + H$	$1.64\times10^{7}T^{2.55}\exp\left(\frac{-3.85\times10^{5}}{RT}\right)$	[63]
$CH_3CO \rightarrow CH_3 + CO$	$k_0 = 1\times10^{-8}\exp\left(\frac{-7.08\times10^{3}}{T}\right)$ $k_\infty = 2\times10^{13}\exp\left(\frac{-8.63\times10^{3}}{T}\right)$ $F_c = 5\times10^{-1}$	[33] [c]
$CH_3CHO \rightarrow CH_3CO + H$	$5\times10^{14}\exp\left(\frac{-3.68\times10^{5}}{RT}\right)$	[64]
$CH_3CHO \rightarrow CH_4 + CO$	$1\times10^{15}\exp\left(\frac{-3.56\times10^{5}}{RT}\right)$	[64]
$CH_3CHO \rightarrow CH_3 + CHO$	$2.1\times10^{16}\exp\left(\frac{-4.1135\times10^{4}}{T}\right)$	[33]
$CH_3CH_2OH \rightarrow CH_2OH + CH_3$	$k_0 = \frac{2.88\times10^{85}}{N_A}T^{-18.9}\exp\left(\frac{-5.532\times10^{4}}{T}\right)$ $k_\infty = 5.94\times10^{23}T^{-1.68}\exp\left(\frac{-4.588\times10^{4}}{T}\right)$ $F_c = 5\times10^{-1}\exp\left(\frac{-T}{2\times10^{2}}\right)$ $+5\times10^{-1}\exp\left(\frac{-T}{8.9\times10^{2}}\right)$ $+\exp\left(\frac{-4.6\times10^{3}}{T}\right)$	[65] [c]
$C_2H_6 + H \rightarrow CH_3 + CH_4$	$K_{eq} \times k_{rev}$	[d]
$C_2H_5 + H_2 \rightarrow CH_3 + CH_4$	$K_{eq} \times k_{rev}$	[d]
$CH_2 + H \rightarrow CH_3$	$K_{eq} \times k_{rev}$	[d]
$H + CH_2O \rightarrow CH_3 + O$	$K_{eq} \times k_{rev}$	[d]
$CO + H_2 \rightarrow CH_2 + O$	$K_{eq} \times k_{rev}$	[d]
$CO + CH_2O \rightarrow CH_2 + CO_2$	$K_{eq} \times k_{rev}$	[d]
$CH_3O + H \rightarrow CH_3 + OH$	$K_{eq} \times k_{rev}$	[d]
$H_2 + CH_2O \rightarrow CH_3 + OH$	$K_{eq} \times k_{rev}$	[d]
$H + CH_2O \rightarrow CH_2 + OH$	$K_{eq} \times k_{rev}$	[d]
$CH_3 + CO_2 \rightarrow CH_3O + CO$	$K_{eq} \times k_{rev}$	[d]
$CO + H_2 \rightarrow H + CHO$	$K_{eq} \times k_{rev}$	[d]
$CH_2 + O \rightarrow H + CHO$	$K_{eq} \times k_{rev}$	[d]
$H_2 + CH_2O \rightarrow CH_3O + H$	$K_{eq} \times k_{rev}$	[d]
$CH_3OH \rightarrow CH_3O + H$	$K_{eq} \times k_{rev}$	[d]

$CH_3OH + H \rightarrow CH_3O + H_2$	$K_{eq} \times k_{rev}$	[d]
$H_2 + CH_2O \rightarrow CH_2OH + H$	$K_{eq} \times k_{rev}$	[d]
$CH_3 + H_2O \rightarrow CH_3OH + H$	$K_{eq} \times k_{rev}$	[d]
$CO + H_2O \rightarrow CHO + OH$	$K_{eq} \times k_{rev}$	[d]
$H_2O + CH_2O \rightarrow CH_3O + OH$	$K_{eq} \times k_{rev}$	[d]
$H_2O + CH_2O \rightarrow CH_2OH + OH$	$K_{eq} \times k_{rev}$	[d]
$CH_3OH + OH \rightarrow CH_2OH + H_2O$	$K_{eq} \times k_{rev}$	[d]
$CO + OH \rightarrow CHO + O$	$K_{eq} \times k_{rev}$	[d]
$CO_2 + H \rightarrow CHO + O$	$K_{eq} \times k_{rev}$	[d]
$CHO + OH \rightarrow CH_2O + O$	$K_{eq} \times k_{rev}$	[d]
$CH_2O + OH \rightarrow CH_3O + O$	$K_{eq} \times k_{rev}$	[d]
$CH_2OH + OH \rightarrow CH_3OH + O$	$K_{eq} \times k_{rev}$	[d]
$CH_4 + CO \rightarrow CH_3 + CHO$	$K_{eq} \times k_{rev}$	[d]
$CH_3 + CO \rightarrow CH_2 + CHO$	$K_{eq} \times k_{rev}$	[d]
$CH_3 + CHO \rightarrow CH_2 + CH_2O$	$K_{eq} \times k_{rev}$	[d]
$CH_4 + CH_2O \rightarrow CH_3 + CH_3O$	$K_{eq} \times k_{rev}$	[d]
$CH_3 + CH_2O \rightarrow CH_2 + CH_3O$	$K_{eq} \times k_{rev}$	[d]
$CH_4 + CH_2O \rightarrow CH_2OH + CH_3$	$K_{eq} \times k_{rev}$	[d]
$CH_3 + CH_2O \rightarrow CH_2 + CH_2OH$	$K_{eq} \times k_{rev}$	[d]
$CH_2OH + CH_3 \rightarrow CH_2 + CH_3OH$	$K_{eq} \times k_{rev}$	[d]
$CH_3 + CH_3O \rightarrow CH_2 + CH_3OH$	$K_{eq} \times k_{rev}$	[d]
$CO + CH_2O \rightarrow CHO + CHO$	$K_{eq} \times k_{rev}$	[d]
$CH_3OH + CO \rightarrow CH_3O + CHO$	$K_{eq} \times k_{rev}$	[d]
$CH_3OH + CO \rightarrow CH_2OH + CHO$	$K_{eq} \times k_{rev}$	[d]
$CH_2O + CH_2O \rightarrow CH_2OH + CHO$	$K_{eq} \times k_{rev}$	[d]
$CH_3OH + CH_2O \rightarrow CH_3O + CH_3O$	$K_{eq} \times k_{rev}$	[d]
$CH_3OH + CH_2O \rightarrow CH_2OH + CH_3O$	$K_{eq} \times k_{rev}$	[d]
$CH_3OH + CH_2O \rightarrow CH_2OH + CH_2OH$	$K_{eq} \times k_{rev}$	[d]
$CH_3CHO + H \rightarrow C_2H_5 + O$	$K_{eq} \times k_{rev}$	[d]
$CH_3 + CH_2O \rightarrow C_2H_5 + O$	$K_{eq} \times k_{rev}$	[d]
$C_2H_6 + CO \rightarrow C_2H_5 + CHO$	$K_{eq} \times k_{rev}$	[d]
$C_2H_6 + CH_2O \rightarrow C_2H_5 + CH_3O$	$K_{eq} \times k_{rev}$	[d]
$C_2H_6 + CH_2O \rightarrow C_2H_5 + CH_2OH$	$K_{eq} \times k_{rev}$	[d]
$CH_3 + CHO \rightarrow CH_3CO + H$	$K_{eq} \times k_{rev}$	[d]
$C_2H_5 + H_2O \rightarrow CH_3CH_2OH + H$	$K_{eq} \times k_{rev}$	[d]

$CH_3CO + H_2O \rightarrow CH_3CHO + OH$	$K_{eq} \times k_{rev}$	[d]
$CH_3 + CO_2 \rightarrow CH_3CO + O$	$K_{eq} \times k_{rev}$	[d]
$CH_3CO + OH \rightarrow CH_3CHO + O$	$K_{eq} \times k_{rev}$	[d]
$CH_3CHO + CO \rightarrow CH_3CO + CHO$	$K_{eq} \times k_{rev}$	[d]
$CH_3CHO + CHO \rightarrow CH_3CO + CH_2O$	$K_{eq} \times k_{rev}$	[d]
$CH_3CHO + CH_2O \rightarrow CH_3CO + CH_3O$	$K_{eq} \times k_{rev}$	[d]
$CH_2OH + CH_3CHO \rightarrow CH_3CO + CH_3OH$	$K_{eq} \times k_{rev}$	[d]
$CH_3CO + CH_3OH \rightarrow CH_3CHO + CH_3O$	$K_{eq} \times k_{rev}$	[d]
$H + CHO \rightarrow CH_2O$	$K_{eq} \times k_{rev}$	[d]
$CO + H_2 \rightarrow CH_2O$	$K_{eq} \times k_{rev}$	[d]
$H + CH_2O \rightarrow CH_2OH$	$K_{eq} \times k_{rev}$	[d]
$CH_2 + H_2O \rightarrow CH_3OH$	$K_{eq} \times k_{rev}$	[d]
$CH_2OH + H \rightarrow CH_3OH$	$K_{eq} \times k_{rev}$	[d]
$CH_4 + CO \rightarrow CH_3CHO$	$K_{eq} \times k_{rev}$	[d]

a) Units are s^{-1}, $cm^3\ s^{-1}$ or $cm^6\ s^{-1}$ for unimolecular, bimolecular or trimolecular reactions, respectively.

b) $N_A = 6.02214076 \times 10^{23}\ mol^{-1}$, $R = 8.314462618\ J\ mol^{-1}\ K^{-1}$, $M = 1.449 \times 10^{19}\ cm^{-3}$.

c) Fall-off expressions, see eqs. (S23), (S24) and (S25).

d) Rate coefficient calculated from the equilibrium constants and the rate coefficient of the reverse reaction. Equilibrium constants are calculated from the data in ref. [66].

S5.5 Electron impact processes included in the Bolsig+ calculations

Table S6. List of electron impact processes used in the calculation of the electron impact dissociation rate coefficients and electron mobilities with BOLSIG+.

Electron impact process	Reference
$CH_4 + e^- \rightarrow CH_4^+ + 2e^-$	[67]
$CH_4 + e^- \rightarrow CH_3^+ + H + 2e^-$	[67]
$CH_4 + e^- \rightarrow CH_2^+ + H_2 + 2e^-$	[67]
$CH_4 + e^- \rightarrow CH_2^+ + 2H + 2e^-$	[67]
$CH_4 + e^- \rightarrow CH^+ + H_2 + H + 2e^-$	[67]
$CH_4 + e^- \rightarrow CH_3 + H + e^-$	[67]
$CH_4 + e^- \rightarrow CH_2 + H_2 + e^-$	[67]
$CH_4 + e^- \rightarrow CH_2 + 2H + e^-$	[67]
$CH_4 + e^- \rightarrow CH + H_2 + H + e^-$	[67]
$CH_4 + e^- \rightarrow C + H_2 + 2H + e^-$	[67]
$CH_4 + e^- \rightarrow C + 2H_2 + e^-$	[67]
$CH_4 + e^- \rightarrow CH_4 + e^-$ (elastic)	[68]
$CH_4 + e^- \rightarrow CH_4(\nu_{1,3}) + e^-$	[68]
$CH_4 + e^- \rightarrow CH_4(\nu_{2,4}) + e^-$	[68]
$CH_4 + e^- \rightarrow CH_2^- + H_2$	[68]
$CH_4 + e^- \rightarrow CH_3 + H^-$	[68]
$CO_2 + e^- \rightarrow CO_2^+ + 2e^-$	[68]
$CO_2 + e^- \rightarrow CO + O(1D) + e^-$	[69]
$CO_2 + e^- \rightarrow CO(a3P) + O + e^-$	[69]
$CO_2 + e^- \rightarrow CO_2 + e^-$ (effective)	[68]
$CO_2 + e^- \rightarrow CO_2(\nu_{010}) + e^-$	[68]
$CO_2 + e^- \rightarrow CO_2(\nu_{020}) + e^-$	[68]
$CO_2 + e^- \rightarrow CO_2(\nu_{100}) + e^-$	[68]
$CO_2 + e^- \rightarrow CO_2(\nu_{030+110}) + e^-$	[68]
$CO_2 + e^- \rightarrow CO_2(\nu_{001}) + e^-$	[68]
$CO_2 + e^- \rightarrow CO_2(\nu_{040+120+011}) + e^-$	[68]
$CO_2 + e^- \rightarrow CO_2(X, \nu_{020}) + e^-$	[68]
$CO_2 + e^- \rightarrow CO_2(X, \nu_{050+210+130+021+101}) + e^-$	[68]
$CO_2 + e^- \rightarrow CO_2(X, \nu_{300}) + e^-$	[68]
$CO_2 + e^- \rightarrow CO_2(X, \nu_{060+220+140}) + e^-$	[68]

$CO_2 + e^- \rightarrow CO_2(X, \nu_{0n0+n00}) + e^-$	[68]
$CO_2 + e^- \rightarrow CO_2(E1) + e^-$	[68]
$CO_2 + e^- \rightarrow CO_2(E2) + e^-$	[68]
$CO_2 + e^- \rightarrow CO + O^-$	[70]
$CO + e^- \rightarrow CO^+ + 2e^-$	[68]
$CO + e^- \rightarrow C + O + e^-$	[68]
$CO + e^- \rightarrow CO + e^-$ (elastic)	[68]
$CO + e^- \rightarrow CO(\nu_x) + e^-$ (with x = 1-10)	[68]
$CO + e^- \rightarrow CO(a3P) + e^-$	[68]
$CO + e^- \rightarrow CO(a'3Su+) + e^-$	[68]
$CO + e^- \rightarrow CO(A1P) + e^-$	[68]
$CO + e^- \rightarrow CO(b3Su+) + e^-$	[68]
$CO + e^- \rightarrow CO(B1Su+) + e^-$	[68]
$CO + e^- \rightarrow CO(C1Su+) + e^-$	[68]
$CO + e^- \rightarrow CO(E1P) + e^-$	[68]
$CO + e^- \rightarrow C + O^-$	[68]
$C_2H_6 + e^- \rightarrow C_2H_6^+ + 2e^-$	[67]
$C_2H_6 + e^- \rightarrow C_2H_5^+ + H + 2e^-$	[67]
$C_2H_6 + e^- \rightarrow C_2H_4^+ + H_2 + 2e^-$	[67]
$C_2H_6 + e^- \rightarrow C_2H_3^+ + H_2 + H + 2e^-$	[67]
$C_2H_6 + e^- \rightarrow C_2H_2^+ + 2H_2 + 2e^-$	[67]
$C_2H_6 + e^- \rightarrow C_2H_2^+ + H_2 + 2H + 2e^-$	[67]
$C_2H_6 + e^- \rightarrow C_2H_4 + H_2^+ + 2e^-$	[67]
$C_2H_6 + e^- \rightarrow CH_3^+ + CH_3 + 2e^-$	[67]
$C_2H_6 + e^- \rightarrow C_2H_5 + H + e^-$	[67,71]
$C_2H_6 + e^- \rightarrow C_2H_4 + H_2 + e^-$	[67,71]
$C_2H_6 + e^- \rightarrow C_2H_3 + H_2 + H + e^-$	[67,71]
$C_2H_6 + e^- \rightarrow C_2H_2 + 2H_2 + e^-$	[67,71]
$C_2H_6 + e^- \rightarrow CH_4 + CH_2 + e^-$	[67,71]
$C_2H_6 + e^- \rightarrow 2CH_3 + e^-$	[67,71]
$C_2H_6 + e^- \rightarrow C_2H_6 + e^-$ (elastic)	[72]
$C_2H_6 + e^- \rightarrow C_2H_6(\nu_{1,3}) + e^-$	[72]
$C_2H_6 + e^- \rightarrow C_2H_6(\nu_{2,4}) + e^-$	[72]
$C_2H_6 + e^- \rightarrow C_2H_6(E1) + e^-$	[72]
$C_2H_6 + e^- \rightarrow C_2H_6(E2) + e^-$	[72]

$H_2 + e^- \rightarrow H_2^+ + 2e^-$	[68]
$H_2 + e^- \rightarrow H + H^+ + 2e^-$	[73]
$H_2 + e^- \rightarrow 2H + e^-$	[73]
$H_2 + e^- \rightarrow H_2 + e^-$ (elastic)	[68]
$H_2 + e^- \rightarrow H_2(\nu_x) + e^-$ (with x = 1-3)	[68]
$H_2 + e^- \rightarrow H_2(b3Su) + e^-$	[68]
$H_2 + e^- \rightarrow H_2(B1Su) + e^-$	[68]
$H_2 + e^- \rightarrow H_2(c3Pu) + e^-$	[68]
$H_2 + e^- \rightarrow H_2(a3Sg) + e^-$	[68]
$H_2 + e^- \rightarrow H_2(C1Pu) + e^-$	[68]
$H_2 + e^- \rightarrow H_2(E1Sg, F1Sg) + e^-$	[68]
$H_2 + e^- \rightarrow H_2(e3Su) + e^-$	[68]
$H_2 + e^- \rightarrow H_2(B'1Su) + e^-$	[68]
$H_2 + e^- \rightarrow H_2(D1Pu) + e^-$	[68]
$H_2 + e^- \rightarrow H_2(B''1Su) + e^-$	[68]
$H_2 + e^- \rightarrow H_2(D'1Pu) + e^-$	[68]
$H_2 + e^- \rightarrow H + H^-$	[73]
$H_2O + e^- \rightarrow H_2O^+ + 2e^-$	[74,75]
$H_2O + e^- \rightarrow H + OH^+ + 2e^-$	[74,75]
$H_2O + e^- \rightarrow H_2 + O^+ + 2e^-$	[74,75]
$H_2O + e^- \rightarrow H_2^+ + O + 2e^-$	[74,75]
$H_2O + e^- \rightarrow H^+ + OH + 2e^-$	[74,75]
$H_2O + e^- \rightarrow H + OH + e^-$	[76]
$H_2O + e^- \rightarrow H_2O + e^-$ (elastic)	[72]
$H_2O + e^- \rightarrow H_2O(rot) + e^-$	[74]
$H_2O + e^- \rightarrow H_2O(\nu_{010}) + e^-$	[74]
$H_2O + e^- \rightarrow H_2O(\nu_{100+001}) + e^-$	[74]
$H_2O + e^- \rightarrow H + OH^-$	[74,75]
$H_2O + e^- \rightarrow H_2 + O^-$	[74,76]
$H_2O + e^- \rightarrow H^- + OH$	[74,76]

S5.6 Electron impact dissociation rate coefficients

Table S7. Electron impact dissociation reactions included in the coupled plasma-surface model and the corresponding calculated rate coefficients multiplied with the electron density ($n_e = 10^{14}$ cm^{-3}).

Reaction	**$k \times n_e$ (s^{-1})**
$CH_4 + e^- \rightarrow CH_3 + H + e^-$	4.1×10^{-2}
$CH_4 + e^- \rightarrow CH_2 + H_2 + e^-$	9.2×10^{-3}
$CH_4 + e^- \rightarrow CH_2 + 2H + e^-$	6.9×10^{-4}
$CO_2 + e^- \rightarrow CO + O + e^-$	4.4×10^{-2}
$H_2O + e^- \rightarrow H + OH + e^-$	8.2×10^{-2}
$H_2 + e^- \rightarrow 2H + e^-$	9.3×10^{-2}
$C_2H_6 + e^- \rightarrow C_2H_5 + H + e^-$	1.1×10^{-2}
$C_2H_6 + e^- \rightarrow CH_2 + CH_4 + e^-$	4.1×10^{-3}
$C_2H_6 + e^- \rightarrow 2CH_3 + e$	5.9×10^{-3}

S5.7 Catalyst surface reactions

Table S8. List of catalyst surface reactions included in the CatMAP and coupled plasma-surface models.

Reaction[a, b]	**Transition state**
$CH_4 + *^s + *^h \rightleftharpoons CH_3*^s + H*^h$	$CH_3\text{-}H*^s + *^h$
$CH_3*^s + *^h \rightleftharpoons CH_2*^s + H*^h$	$CH_2\text{-}H*^s + *^h$
$CH_2*^s + *^h \rightleftharpoons CH*^s + H*^h$	$CH\text{-}H*^s + *^h$
$CO_2 + *^s \rightleftharpoons CO_2*^s$	-[c]
$CO_2*^s + *^s \rightleftharpoons CO*^s + O*^s$	$O\text{-}CO*^s + *^s$
$CO + *^s \rightleftharpoons CO*^s$	-[c]
$H_2 + *^h + *^h \rightleftharpoons H*^h + H*^h$	$H\text{-}H*^h + *^h$
$O*^s + H*^h \rightleftharpoons OH*^s + *^h$	$O\text{-}H*^s + *^h$
$OH*^s + H*^h \rightleftharpoons H_2O + *^s + *^h$	$H\text{-}OH*^s + *^h$
$H + *^h \rightleftharpoons H*^h$	-[c]
$O + *^s \rightleftharpoons O*^s$	-[c]
$CH_3 + *^s \rightleftharpoons CH_3*^s$	-[c]
$CH_2 + *^s \rightleftharpoons CH_2*^s$	-[c, d]
$OH + *^s \rightleftharpoons OH*^s$	-[c, d]
$CHO + *^s \rightleftharpoons CHO*^s$	-[c, d]
$CO*^s + H*^h \rightleftharpoons CHO*^s + *^h$	$H\text{-}CO*^s + *^h$
$CHO*^s + H*^h \rightleftharpoons CHOH*^s + *^h$	$HCO\text{-}H*^s + *^h$
$CHOH*^s + *^s \rightleftharpoons CH*^s + OH*^s$	$CH\text{-}OH*^s + *^s$
$CH*^s + CO*^s \rightleftharpoons CHCO*^s + *^s$	$CH\text{-}CO*^s + *^s$
$CHCO*^s + H*^h \rightleftharpoons CH_2CO*^s + *^h$	$H\text{-}CHCO*^s + *^h$
$CH_2CO*^s + H*^h \rightleftharpoons CH_3CO*^s + *^h$	$H\text{-}CH_2CO*^s + *^h$
$CH_3CO*^s + H*^h \rightleftharpoons CH_3CHO*^s + *^h$	$H\text{-}CH_3CO*^s + *^h$
$CH_3CHO*^s \rightleftharpoons CH_3CHO + *^s$	-[c]
$CH_3CHO*^s + H*^h \rightleftharpoons CH_3CHOH*^s + *^h$	$CH_3CHO\text{-}H*^s + *^h$
$CH_3CHOH*^s + H*^h \rightleftharpoons CH_3CH_2OH*^s + *^h$	$CH_3CHOH\text{-}H*^s + *^h$
$CH_3CH_2OH*^s \rightleftharpoons CH_3CH_2OH + *^s$	-[c]
$CHO*^s + H*^h \rightleftharpoons CH_2O*^s + *^h$	$H\text{-}CHO*^s + *^h$
$CH_2O*^s \rightleftharpoons CH_2O + *^s$	-[c, d]
$CH_2O*^s + H*^h \rightleftharpoons CH_3O*^s + *^h$	$H\text{-}CH_2O*^s + *^h$
$CH_3O*^s + H*^h \rightleftharpoons CH_3OH + *^s + *^h$	$CH_3O\text{-}H*^s + *^h$

$CHOH^{*s} + H^{*h} \rightleftharpoons CH_2OH^{*s} + *^{h}$	$H\text{-}CHOH^{*s} + *^{h}$
$CH_2OH^{*s} + H^{*h} \rightleftharpoons CH_3OH + *^{s} + *^{h}$	$H\text{-}CH_2OH^{*s} + *^{h}$
$CH_3O^{*s} + *^{s} + H^{*h} \rightleftharpoons CH_3^{*s} + OH^{*s} + *^{h}$	$CH_3\text{-}OH^{*s} + *^{s} + *^{h}$
$CH_3^{*s} + CO^{*s} \rightleftharpoons CH_3CO^{*s} + *^{s}$	$CH_3\text{-}CO^{*s} + *^{s}$

a) All reactions on the transition metal surfaces are included in both the forward and reverse direction.

b) Superscripts h and s denote hydrogen reservoir and catalytic surface sites, respectively.

c) Molecular and radical adsorption/desorption reactions are considered to occur without additional energy barrier. For these cases the enthalpy and Gibbs free energy barriers are determined by the reaction enthalpy and Gibbs free energy, respectively.

d) These adsorption/desorption reactions are only included in the coupled plasma-surface simulations and not in the simulations with the CatMAP model.

S5.8 Reactions on the non-catalytic wall

Table S9. List of reactions that occur on the non-catalytic wall included in the coupled plasma-surface model.

Physisorption [a]	**Desorption** [a]
$H + *^{p} \rightarrow H*^{p}$	$H*^{p} \rightarrow H + *^{p}$
$O + *^{p} \rightarrow O*^{p}$	$O*^{p} \rightarrow O + *^{p}$
$CH_3 + *^{p} \rightarrow CH_3*^{p}$	$CH_3*^{p} \rightarrow CH_3 + *^{p}$
$CH_2 + *^{p} \rightarrow CH_2*^{p}$	$CH_2*^{p} \rightarrow CH_2 + *^{p}$
$CHO + *^{p} \rightarrow CHO*^{p}$	$CHO*^{p} \rightarrow CHO + *^{p}$
$OH + *^{p} \rightarrow OH*^{p}$	$OH*^{p} \rightarrow OH + *^{p}$
Chemisorption [a]	**Surface diffusion** [a]
$H + *^{c} \rightarrow H*^{c}$	$H*^{p} + *^{c} \rightarrow H*^{c} + *^{p}$
$O + *^{c} \rightarrow O*^{c}$	$O*^{p} + *^{c} \rightarrow O*^{c} + *^{p}$
$CH_3 + *^{c} \rightarrow CH_3*^{c}$	$CH_3*^{p} + *^{c} \rightarrow CH_3*^{c} + *^{p}$
$CH_2 + *^{c} \rightarrow CH_2*^{c}$	$CH_2*^{p} + *^{c} \rightarrow CH_2*^{c} + *^{p}$
$CHO + *^{c} \rightarrow CHO*^{c}$	$CHO*^{p} + *^{c} \rightarrow CHO*^{c} + *^{p}$
$OH + *^{c} \rightarrow OH*^{c}$	$OH*^{p} + *^{c} \rightarrow OH*^{c} + *^{p}$
Eley-Rideal [a]	**Langmuir-Hinshelwood** [a]
$H + H*^{c} \rightarrow H_2 + *^{c}$	$H*^{p} + H*^{c} \rightarrow H_2 + *^{p} + *^{c}$
$H + CH_3*^{c} \rightarrow CH_4 + *^{c}$	$H*^{p} + CH_3*^{c} \rightarrow CH_4 + *^{p} + *^{c}$
$H + CHO*^{c} \rightarrow CH_2O + *^{c}$	$H*^{p} + CHO*^{c} \rightarrow CH_2O + *^{p} + *^{c}$
$H + OH*^{c} \rightarrow H_2O + *^{c}$	$H*^{p} + OH*^{c} \rightarrow H_2O + *^{p} + *^{c}$
$H + O*^{c} \rightarrow OH*^{c}$	$H*^{p} + O*^{c} \rightarrow OH*^{c} + *^{p}$
$H + CH_2*^{c} \rightarrow CH_3*^{c}$	$H*^{p} + CH_2*^{c} \rightarrow CH_3*^{c} + *^{p}$
$CH_3 + H*^{c} \rightarrow CH_4 + *^{c}$	$CH_3*^{p} + H*^{c} \rightarrow CH_4 + *^{p} + *^{c}$
$CHO + H*^{c} \rightarrow CH_2O + *^{c}$	$CHO*^{p} + H*^{c} \rightarrow CH_2O + *^{p} + *^{c}$
$OH + H*^{c} \rightarrow H_2O + *^{c}$	$OH*^{p} + H*^{c} \rightarrow H_2O + *^{p} + *^{c}$
$O + H*^{c} \rightarrow OH*^{c}$	$O*^{p} + H*^{c} \rightarrow OH*^{c} + *^{p}$
$CH_2 + H*^{c} \rightarrow CH_3*^{c}$	$CH_2*^{p} + H*^{c} \rightarrow CH_3*^{c} + *^{p}$
$CO + O*^{c} \rightarrow CO_2 + *^{c}$	

a) Superscripts c and p denote chemisorption and physisorption sites, respectively.

S6. References

[1] J. Schumann, A.J. Medford, J.S. Yoo, Z.-J. Zhao, P. Bothra, A. Cao, F. Studt, F. Abild-Pedersen, J.K. Nørskov, ACS Catal. 8 (2018) 3447–3453. https://doi.org/10.1021/acscatal.8b00201.

[2] P.J. Linstrom, W.G. Mallard, eds., NIST Chemistry WebBook, NIST Standard Reference Database Number 69, National Institute of Standards and Technology, Gaithersburg MD, 20899, . https://doi.org/10.18434/T4D303.

[3] J. Klimeš, D.R. Bowler, A. Michaelides, Phys. Rev. B. 83 (2011) 195131. https://doi.org/10.1103/PhysRevB.83.195131.

[4] G. Kresse, J. Hafner, Phys. Rev. B. 49 (1994) 14251–14269. https://doi.org/10.1103/PhysRevB.49.14251.

[5] G. Kresse, J. Hafner, Phys. Rev. B. 47 (1993) 558–561. https://doi.org/10.1103/PhysRevB.47.558.

[6] G. Kresse, J. Furthmüller, Comput. Mater. Sci. 6 (1996) 15–50. https://doi.org/10.1016/0927-0256(96)00008-0.

[7] G. Kresse, J. Furthmüller, Phys. Rev. B. 54 (1996) 11169–11186. https://doi.org/10.1103/PhysRevB.54.11169.

[8] G. Román-Pérez, J.M. Soler, Phys. Rev. Lett. 103 (2009) 096102. https://doi.org/10.1103/PhysRevLett.103.096102.

[9] K. Lee, É.D. Murray, L. Kong, B.I. Lundqvist, D.C. Langreth, Phys. Rev. B. 82 (2010) 081101. https://doi.org/10.1103/PhysRevB.82.081101.

[10] J. Wellendorff, K.T. Lundgaard, A. Møgelhøj, V. Petzold, D.D. Landis, J.K. Nørskov, T. Bligaard, K.W. Jacobsen, Phys. Rev. B. 85 (2012) 235149. https://doi.org/10.1103/PhysRevB.85.235149.

[11] G. Kresse, J. Hafner, J. Phys. Condens. Matter. 6 (1994) 8245–8257. https://doi.org/10.1088/0953-8984/6/40/015.

[12] G. Kresse, D. Joubert, Phys. Rev. B. 59 (1999) 1758–1775. https://doi.org/10.1103/PhysRevB.59.1758.

[13] G. Henkelman, H. Jónsson, J. Chem. Phys. 111 (1999) 7010–7022. https://doi.org/10.1063/1.480097.

[14] A. Heyden, A.T. Bell, F.J. Keil, J. Chem. Phys. 123 (2005) 224101. https://doi.org/10.1063/1.2104507.

[15] J. Kästner, P. Sherwood, J. Chem. Phys. 128 (2008) 014106. https://doi.org/10.1063/1.2815812.

[16] P. Xiao, D. Sheppard, J. Rogal, G. Henkelman, J. Chem. Phys. 140 (2014) 174104. https://doi.org/10.1063/1.4873437.

[17] A.J. Medford, C. Shi, M.J. Hoffmann, A.C. Lausche, S.R. Fitzgibbon, T. Bligaard, J.K. Nørskov, Catal. Letters. 145 (2015) 794–807. https://doi.org/10.1007/s10562-015-1495-6.

[18] F. Abild-Pedersen, J. Greeley, F. Studt, J. Rossmeisl, T.R. Munter, P.G. Moses, E. Skúlason, T. Bligaard, J.K. Nørskov, Phys. Rev. Lett. 99 (2007) 016105. https://doi.org/10.1103/PhysRevLett.99.016105.

[19] S. Wang, B. Temel, J. Shen, G. Jones, L.C. Grabow, F. Studt, T. Bligaard, F. Abild-Pedersen, C.H. Christensen, J.K. Nørskov, Catal. Letters. 141 (2011) 370–373. https://doi.org/10.1007/s10562-010-0477-y.

[20] A.C. Lausche, A.J. Medford, T.S. Khan, Y. Xu, T. Bligaard, F. Abild-Pedersen, J.K. Nørskov, F. Studt, J. Catal. 307 (2013) 275–282. https://doi.org/10.1016/j.jcat.2013.08.002.

[21] A.H. Larsen, J.J. Mortensen, J. Blomqvist, I.E. Castelli, R. Christensen, M. Dułak, J. Friis, M.N. Groves, B. Hammer, C. Hargus, E.D. Hermes, P.C. Jennings, P.B. Jensen, J. Kermode, J.R. Kitchin, E.L. Kolsbjerg, J. Kubal, K. Kaasbjerg, S. Lysgaard, J. Bergmann Maronsson, T. Maxson, T. Olsen, L. Pastewka, A. Peterson, C. Rostgaard, J. Schiøtz, O. Schütt, M. Strange, K.S. Thygesen, T. Vegge, L. Vilhelmsen, M. Walter, Z. Zeng, K.W. Jacobsen, J. Phys. Condens. Matter. 29 (2017) 273002. https://doi.org/10.1088/1361-648X/aa680e.

[22] P. Mehta, P. Barboun, F.A. Herrera, J. Kim, P. Rumbach, D.B. Go, J.C. Hicks, W.F. Schneider, Nat. Catal. 1 (2018) 269–275. https://doi.org/10.1038/s41929-018-0045-1.

[23] Y.C. Kim, M. Boudart, Langmuir. 7 (1991) 2999–3005. https://doi.org/10.1021/la00060a016.

[24] V. Guerra, IEEE Trans. Plasma Sci. 35 (2007) 1397–1412. https://doi.org/10.1109/TPS.2007.902028.

[25] A.E.D. Heylen, Int. J. Electron. 39 (1975) 653–660. https://doi.org/10.1080/00207217508920532.

[26] A. Fridman, Plasma Chemistry, Cambridge University Press, New York, 2008. www.cambridge.org/9780521847353.

[27] G.J.M. Hagelaar, L.C. Pitchford, Plasma Sources Sci. Technol. 14 (2005) 722–733. https://doi.org/10.1088/0963-0252/14/4/011.

[28] W. Tsang, R.F. Hampson, J. Phys. Chem. Ref. Data. 15 (1986) 1087–1279.

https://doi.org/10.1063/1.555759.

[29] C.T. Campbell, L.H. Sprowl, L. Árnadóttir, J. Phys. Chem. C. 120 (2016) 10283–10297. https://doi.org/10.1021/acs.jpcc.6b00975.

[30] N.E. Afonina, V.G. Gromov, V.L. Kovalev, Fluid Dyn. 37 (2002) 117–125.

[31] A.J. Medford, A.C. Lausche, F. Abild-Pedersen, B. Temel, N.C. Schjødt, J.K. Nørskov, F. Studt, Top. Catal. 57 (2014) 135–142. https://doi.org/10.1007/s11244-013-0169-0.

[32] R.D. Johnson, ed., NIST Computational Chemistry Comparison and Benchmark Database NIST Standard Reference Database Number 101 Release 22, 2022. https://doi.org/10.18434/T47C7Z.

[33] D.L. Baulch, C.T. Bowman, C.J. Cobos, R.A. Cox, T. Just, J.A. Kerr, M.J. Pilling, D. Stocker, J. Troe, W. Tsang, R.W. Walker, J. Warnatz, J. Phys. Chem. Ref. Data. 34 (2005) 757–1397. https://doi.org/10.1063/1.1748524.

[34] M. Capitelli, C.M. Ferreira, B.F. Gordiets, A.I. Osipov, Plasma Kinetics in Atmospheric Gases, Springer Berlin Heidelberg, Berlin, Heidelberg, 2000. https://doi.org/10.1007/978-3-662-04158-1.

[35] H.G. Wagner, F. Zabel, Berichte Der Bunsengesellschaft Für Phys. Chemie. 78 (1974) 705–712. https://doi.org/10.1002/bbpc.19740780717.

[36] M.J. Rabinowitz, J.W. Sutherland, P.M. Patterson, R.B. Klemm, J. Phys. Chem. 95 (1991) 674–681. https://doi.org/10.1021/j100155a033.

[37] K.-W. Lu, H. Matsui, C.-L. Huang, P. Raghunath, N.-S. Wang, M.C. Lin, J. Phys. Chem. A. 114 (2010) 5493–5502. https://doi.org/10.1021/jp100535r.

[38] K. Tabayashi, S.H. Bauer, Combust. Flame. 34 (1979) 63–83. https://doi.org/10.1016/0010-2180(79)90079-8.

[39] T. Böhland, S. Dõbẽ, F. Temps, H.G. Wagner, Berichte Der Bunsengesellschaft Für Phys. Chemie. 89 (1985) 1110–1116. https://doi.org/10.1002/bbpc.19850891018.

[40] P. Han, K. Su, Y. Liu, Y. Wang, X. Wang, Q. Zeng, L. Cheng, L. Zhang, J. Comput. Chem. 32 (2011) 2745–2755. https://doi.org/10.1002/jcc.21854.

[41] Y. Ge, M.S. Gordon, F. Battaglia, R.O. Fox, J. Phys. Chem. A. 114 (2010) 2384–2392. https://doi.org/10.1021/jp911673h.

[42] V. Lissianski, H. Yang, Z. Qin, M.R. Mueller, K.S. Shin, W.C. Gardiner, Chem. Phys. Lett. 240 (1995) 57–62. https://doi.org/10.1016/0009-2614(95)00496-Q.

[43] N.K. Srinivasan, M.-C. Su, J.W. Sutherland, J. V. Michael, J. Phys. Chem. A. 109 (2005) 1857–1863. https://doi.org/10.1021/jp040679j.

[44] N. Cohen, K.R. Westberg, J. Phys. Chem. Ref. Data. 20 (1991) 1211–1311. https://doi.org/10.1063/1.555901.

[45] N. Cohen, K.R. Westberg, J. Phys. Chem. Ref. Data. 12 (1983) 531–590. https://doi.org/10.1063/1.555692.

[46] T. Tsuboi, K. Hashimoto, Combust. Flame. 42 (1981) 61–76. https://doi.org/10.1016/0010-2180(81)90142-5.

[47] H.J. Curran, Int. J. Chem. Kinet. 38 (2006) 250–275. https://doi.org/10.1002/kin.20153.

[48] K. Brudnik, A.A. Gola, J.T. Jodkowski, J. Mol. Model. 15 (2009) 1061–1066. https://doi.org/10.1007/s00894-009-0461-x.

[49] J.T. Jodkowski, M.-T. Rayez, J.-C. Rayez, T. Bérces, S. Dóbé, J. Phys. Chem. A. 103 (1999) 3750–3765. https://doi.org/10.1021/jp984367q.

[50] W. Tsang, J. Phys. Chem. Ref. Data. 16 (1987) 471–508. https://doi.org/10.1063/1.555802.

[51] G. Lendvay, T. Bérces, F. Márta, J. Phys. Chem. A. 101 (1997) 1588–1594. https://doi.org/10.1021/jp963188a.

[52] N.K. Srinivasan, M.-C. Su, J. V. Michael, J. Phys. Chem. A. 111 (2007) 3951–3958. https://doi.org/10.1021/jp0673516.

[53] J. Warnatz, Rate Coefficients in the C/H/O System, in: Combust. Chem., Springer New York, New York, NY, 1984: pp. 197–360. https://doi.org/10.1007/978-1-4684-0186-8_5.

[54] K. Ohmori, A. Miyoshi, H. Matsui, N. Washida, J. Phys. Chem. 94 (1990) 3253–3255. https://doi.org/10.1021/j100371a006.

[55] V.D. Knyazev, Chem. Phys. Lett. 685 (2017) 165–170. https://doi.org/10.1016/j.cplett.2017.07.040.

[56] R. Sivaramakrishnan, J. V. Michael, S.J. Klippenstein, J. Phys. Chem. A. 114 (2010) 755–764. https://doi.org/10.1021/jp906918z.

[57] W.K. Aders, H.G. Wagner, Berichte Der Bunsen-Gesellschaft. 77 (1973) 332–335. https://doi.org/10.1002/bbpc.19730770509.

[58] R.E. Dodd, Trans. Faraday Soc. 47 (1951) 56–62. https://doi.org/10.1039/tf9514700056.

[59] G. Höhlein, G.R. Freeman, J. Am. Chem. Soc. 92 (1970) 6118–6125.

https://doi.org/10.1021/ja00724a004.

[60] X. Zhang, L. Ye, Y. Li, Y. Zhang, C. Cao, J. Yang, Z. Zhou, Z. Huang, F. Qi, Combust. Flame. 191 (2018) 431–441. https://doi.org/10.1016/j.combustflame.2018.01.027.

[61] T.J. Held, F.L. Dryer, Int. J. Chem. Kinet. 30 (1998) 805–830. https://doi.org/10.1002/(SICI)1097-4601(1998)30:11<805::AID-KIN4>3.0.CO;2-Z.

[62] C. Dombrowsky, A. Hoffmann, M. Klatt, H. Gg. Wagner, Berichte Der Bunsengesellschaft Für Phys. Chemie. 95 (1991) 1685–1687. https://doi.org/10.1002/bbpc.19910951217.

[63] W.-C. Ing, C.Y. Sheng, J.W. Bozzelli, Fuel Process. Technol. 83 (2003) 111–145. https://doi.org/10.1016/S0378-3820(03)00062-6.

[64] K. Yasunaga, S. Kubo, H. Hoshikawa, T. Kamesawa, Y. Hidaka, Int. J. Chem. Kinet. 40 (2007) 73–102. https://doi.org/10.1002/kin.20294.

[65] N.M. Marinov, Int. J. Chem. Kinet. 31 (1999) 183–220. https://doi.org/10.1002/(SICI)1097-4601(1999)31:3<183::AID-KIN3>3.0.CO;2-X.

[66] B.J. McBride, M.J. Zehe, S. Gordon, NASA Glenn coefficients for calculating thermodynamic properties of individual species, 2002. https://ntrs.nasa.gov/search.jsp?R=20020085330 2020-05-03T03:42:36+00:00Z.

[67] D. Reiter, R.K. Janev, Contrib. to Plasma Phys. 50 (2010) 986–1013. https://doi.org/10.1002/ctpp.201000090.

[68] IST-Lisbon database. www.lxcat.net (accessed January 4, 2023).

[69] L.S. Polak, D.I. Slovetsky, Int. J. Radiat. Phys. Chem. 8 (1976) 257–282. https://doi.org/10.1016/0020-7055(76)90070-X.

[70] Biagi database. www.lxcat.net (accessed January 4, 2023).

[71] R.K. Janev, D. Reiter, Phys. Plasmas. 11 (2004) 780–829. https://doi.org/10.1063/1.1630794.

[72] Hayashi database. www.lxcat.net (accessed January 3, 2023).

[73] Itikawa database. www.lxcat.net (accessed January 4, 2023).

[74] C. Verheyen, T. Silva, V. Guerra, A. Bogaerts, Plasma Sources Sci. Technol. 29 (2020) 095009. https://doi.org/10.1088/1361-6595/aba1c8.

[75] Y. Itikawa, N. Mason, J. Phys. Chem. Ref. Data. 34 (2005) 1–22. https://doi.org/10.1063/1.1799251.

[76] TRINITI database. www.lxcat.net (accessed January 4, 2023).